Title
Expansion of the Surrogate Method to Measure (n,xn) Cross Sections and Fission Neutron Multiplicity Distributions

Author
Akindele, Oluwatomi

Publication Date
2018

Peer reviewed|Thesis/dissertation

Expansion of the Surrogate Method to Measure (n,xn) Cross Sections and Fission Neutron Multiplicity Distributions

by

Oluwatomi A. Akindele

A dissertation submitted in partial satisfaction of the
requirements for the degree of
Doctor of Philosophy

in

Engineering, Nuclear Engineering

in the

Graduate Division

of the

University of California, Berkeley

Committee in charge:

Professor Eric B. Norman, Chair
Professor Yury G. Kolomensky
Doctor Jason T. Burke

Spring 2018

Expansion of the Surrogate Method to Measure (n,xn) Cross Sections and Fission Neutron Multiplicity Distributions

Abstract

Expansion of the Surrogate Method to Measure (n,xn) Cross Sections and Fission Neutron Multiplicity Distributions

by

Oluwatomi A. Akindele

Doctor of Philosophy in Engineering, Nuclear Engineering

University of California, Berkeley

Professor Eric B. Norman, Chair

In addition to ^{235,238}U and ^{239}Pu, ^{241}Pu is considered a major actinide in regards to nuclear fuel and systems. Despite contributing up to ∼10% of energy generated in nuclear reactors towards the end of a cycle, nuclear data for this isotope is limited. Due to its 14 year half-life, target manufacturing for this isotope is difficult, and as a result the (n,xn) cross section and fission neutron multiplicity as a function of incident neutron energy for ^{241}Pu does not exist in the published literature. Using the surrogate ratio method, experimental difficulties associated with target manufacturing can be circumvented in measuring n + ^{241}Pu reactions by using inelastic scattering of α particles incident on ^{242}Pu to create the same compound nucleus. The NeutronSTARS detection array in Cave 4 of the Texas A&M Cyclotron was commissioned specifically for experiments of this nature. The target chamber consists of three large area silicon detectors: two serve as a silicon telescope to determine the energy of the scattered alpha particle, and one fission detector to gate on fission events by detecting fission fragments. A segmented cylindrical array consisting of 2.2 tons of gadolinium doped liquid scintillator is used to detect emitted neutrons. By relating the detected recoiled alpha energy to an equivalent neutron energy, detecting fission fragments to separate neutron evaporation events from fission, and detecting emitted neutrons in close time coincidence; an attempt to measure the (n,xn) cross section and prompt fission multiplicity for ^{241}Pu was made. The prompt fission neutron multiplicity was fit to a skewed Gaussian distribution, while the average neutron multiplicity was recorded. Due to the large contribution of oxygen and carbon in the target, relatively low neutron detection efficiency, and inadequate background rejection for non-fission events; the (n,xn) cross section measurement was difficult to extract.

To my family

Contents

List of Figures

List of Tables

Acknowledgments

I would first like to thank Professor Eric Norman for being my primary advisor throughout my time in graduate school. I have appreciated your mentorship and support throughout the entire process. In addition your guidance on coursework and research, I have enjoyed your enthusiasm on allowing me to pursue supplemental activities to my thesis project such as traveling and attending workshops and conferences.

The majority of the analysis effort for my dissertation was performed at Lawrence Livermore National Laboratory. I am grateful for the support of the Nuclear and Particle Physics group specifically Jason Burke, Robert Casperson, Richard Hughes, and Barbara Alan. I would like to thank Jason for first conceptualizing the experimental campaign for this project and securing the necessary funds for the detector development, experimental setup, and beam runs. Additionally, I have appreciated your guidance in hands on laboratory activities ranging from how to correctly use an allen key to most of the NeutronBall refurbishment efforts. I would also like to thank Robert for his endless assistance during the analysis portion of the experiment, and sharing your vast knowledge of computer science and data structures with me. I know I will use the analysis tools and approaches you have taught me for the rest of my career, and I am extremely grateful for your mentorship. I would also like to thank Richard for helping me to assemble the NeutronSTARs chamber, sharing a lot of institutional knowledge on the STARS arrays, and always being willing to travel to Texas and taking countless shifts throughout the entire campaign. I would like to thank Barbara for ensuring the targets were made by the time of the experiment, and helping me overcome the ROOT learning curve.

I would also like to thank the entire Texas A&M Cyclotron Institute's staff and operators for allowing us to perform work in their facilities. I specifically want to thank the Cyclotron operators for taking time out of Easter for setting up the beam before our run. I would like to thank Antti Saastamoinen for always being on call to help with equipment in Texas while we were in California. I would also like to thank everyone who took shifts during all the experiments to either characterize the array or perform the experiment: John Koglin, Kay Kolos, Shuya Ota, Perry Chodash, and Andrew Ratkiewicz. I would also like to thank the chemists at LLNL, Roger Henderson and Sherry Faye for making the targets used in the experiment. I would aslo like to thank Yury Kolomensky for serving on my dissertation and qualifying exam committee.

This work was performed under the auspices of the U.S. Department of Energy National Nuclear Security Administration through the Nuclear Science and Security Consortium under Award Number DE-NA-0003180.

Disclaimer: This work was prepared as an account of work sponsored by an agency of the United States Government. Neither the United States Government nor any agency thereof, nor any of their employees, makes any warranty, express or implied, or assumes any legal liability or responsibility for the accuracy, completeness, or usefulness of any information, apparatus, product, or process disclosed, or represents that its use would not infringe privately owned rights. Reference herein to any specific commercial product, process, or service

Chapter 1

Introduction

Nuclear systems are defined by their time dependant neutron economy. To properly simulate new nuclear reactor designs, perform nondestructive assays on material of interest, or accurately perform diagnostics on the aging nuclear stockpile; reliable data on neutron production and loss mechanisms are needed. Neutrons are produced primarily through prompt fission; while a smaller fraction are created from beta-delayed neutron emission of fission fragments, and particle induced neutron emission on both fissile and structural materials such as (n,xn). Furthermore, neutron absorption into non-fissile material and boundary leakage are predominately responsible for *net* losses. Consequently, quantifying these reaction rates and properties: (n,γ), (n,xn), and (n,f); are imperative when defining the power, fissile inventory, and criticality of a given nuclear system.

Of the four major actinides, nuclear data exists for (n,xn) and (n,fxn) reactions for ^{235,238}U and ^{239}Pu. However, for ^{241}Pu the data is sparse in the case of (n,fxn); or nonexistent in the case of (n,xn). Due to its short half-life, 14 years, ^{241}Pu is not naturally occurring. Instead, ^{241}Pu can be created in a nuclear reactor. Initially, nuclear fuel usually contains $3-5\%$ ^{235}U and $95-97\%$ ^{238}U. In this high neutron-fluence environment multiple neutron captures on ^{238}U and subsequent beta decay of its daughters lead to the production of ^{241}Pu:

$$n + {}^{238}\mathrm{U} \rightarrow {}^{239}\mathrm{U} \xrightarrow[23.5min]{\beta-} {}^{239}\mathrm{Np} \xrightarrow[2.36d]{\beta-} {}^{239}\mathrm{Pu} \underset{(n,2n)}{\overset{(n,\gamma)}{\rightleftharpoons}} {}^{240}\mathrm{Pu} \underset{(n,2n)}{\overset{(n,\gamma)}{\rightleftharpoons}} {}^{241}\mathrm{Pu} \tag{1.1}$$

Within this series ^{239}Pu is bred, which can be chemically separated for other uses. Depending on the irradiation time for ^{238}U, any ^{239}Pu extracted will have some concentration of ^{241}Pu. Additionally, the (n,xn) reactions directly affect the fissile inventory of plutonium isotopes. An absence of data propagates into large uncertainties when modeling composite nuclear reactions for both reactors and applications for special nuclear material that contains any plutonium.

1.1 Motivation

Comprehensive nuclear data is imperative the ensuring the safe and secure operation of nuclear power systems. Understanding the (n,xn) and (n,fxn) reactions is needed to inform models and simulations pertaining to nuclear reactor design. In recent years there has been a focus to revolutionize nuclear reactor designs with the incorporation of Generation IV reactors. These reactors use different moderators, fuel composition, and neutron energies than their predecessors, requiring the understanding of material structure, thermal properties, and nuclear data that was not necessary in the past. Additionally, the secure operation of nuclear power requires the timely detection of maleficent activities. Nuclear reactors produce large quantities of plutonium, and verification methods need to be in place to ensure they are not diverted for weapons programs. Algorithms to determine the mass of plutonium in samples and spent fuel are reliant on minute differences in the neutron emission from different isotopes. Providing energy specific data not heavily influenced on generalized assumptions, allow for faster detection times and increased reliability in verification procedures. Lastly, to ensure that nuclear facilities are held accountable for securing and safeguarding their material, international agencies should be able to provide attribution to interdicted nuclear material. Nuclear data gives insight to how a given facilities operational conditions yield distinct signatures in nuclear material.

Advanced Nuclear Reactor Designs

Nuclear reactor disasters mark the turning point in reactor design and safety emphasis. Following the Three Mile Island accident, Generation III reactors were implemented incorporating redundant systems and variable approaches to loss of cooling scenarios[10]. During the Fukishima Daiichi reactor accident, loss of coolant led to reactor fuel meltdowns in Units 1,2 & 3; and caused boiling in the spent fuel pools in Unit 4 [19]. Given the extensive damage to the reactor site and environment due to excessive decay heat in both active and spent fuel, modern reactor designs focus on reducing the quantity of transuranic wastes and using fuels that are impervious to meltdowns. In addition to improved safety features, advanced reactors are more effective at producing power by incorporating new fuel composition and operating past thermal energies.

Generation III reactors mainly focused on utilizing the thermal neutron spectra for fission and subsequent thermal power production. Fissile isotopes have the highest probability to fission at thermal energiess. However, as shown in Equation 1.1; thermal neutron capture on fertile material and subsequent beta decay can lead to the growth of transuranics. Although, isotopes such as ^{239,241}Pu are fissile, when the reaction network is expanded, other transuranics are fissionable and will contribute to decay heat when the reactor is not active due to their high propensity to alpha decay. To ensure the transmutation of transuranics and to increase the fuel utilization in reactors, some new designs, so called "Burner Reactors", operate at fast neutron energies [10]. Using the neutrons at the energies at which they are born from

fission, typically characterized by either a Watt or Maxwell-Boltzman distribution, requires different energy dependent cross sections that extend up to higher energies [10].

In addition to burning spent fuel, "Breed and Burn Reactors" are designed to breed their own fissile material from fertile isotopes such as ^{232}Th and ^{238}U, and burn subsequent minor actinides in a similar manner to Burner rectors. This reduces the need of enrichment towards the front of the nuclear fuel cycle. Neutrons in these reactors now have two purposes, to induce fission and convert fertile fuel. Although traditional light water reactors converted ^{238}U to plutonium, these reactors are intended to breed most of their fissile material. As a result, the neutron multiplicity moments from induced fission are needed for these results. Currently, this is only characterized for ^{241}Pu at thermal energies, but to accurately determine these reactors' isotopic inventory, thermal power output, and critically; the (n,xn) and (n,fxn) cross sections and distributions on all actinides of interest , including ^{241}Pu, will need to be characterized at higher energies.

Nondestructive Assay

Article IV of the Nonproliferation Treaty (NPT) grants each country the "unalienable right" to develop technology for nuclear energy. However, these technologies can be diverted from their intended use leading to the proliferation of nuclear weapons. To verify that nuclear facilities are compliant with the NPT, the International Atomic Energy Agency (IAEA) performs routine inspections throughout all phases of the nuclear fuel cycle. For IAEA inspections to be successful, the methods implemented should ideally be non-intrusive and not compromise the daily operations of the host facility. Nondestructive assay of nuclear material is a preferable technique when verifying the fissile isotopic concentration of nuclear material [37]. As its name suggests, this method allows for material to be assayed without compromising its original structure or composition, and keeps the sample intact. The Next Generation Safeguards Initiative identified determining the mass of plutonium in spent fuel as a high priority for technology development [21]. Although the task referred to the physical detectors deployed to make measurements on spent fuel, the evolution of this technology is limited by the available nuclear data. The initiative focused on spent fuel accountability due to the vast plutonium content (up to 330 kg in a 1100 MWe reactor); however, NDA techniques can also be used to verify the isotopic concentration of smaller scale materials present at an inspection facility.

Neutron instruments for passive NDA measurements vary in size and efficiency, but incorporate similar detection concepts regardless of if the intended use is spent fuel monitoring, plutonium waste measurements, or verifying the composition of mixed-oxide pellets (MOX). These detector use active detection volumes such as ^{3}He or fission chambers surrounded by moderation material such as polyethylene or CH_2 to measure neutrons as a function of time. A detailed description of the passive NDA detectors currently in use by the IAEA can be found in Section 2.2.3.1 of Reference [23]. These systems rely on a spontaneous fission source, ^{244}Cm in spent fuel or ^{240}Pu in plutonium samples, to begin a fission chain. Additionally heavy isotopes in the sample may alpha decay causing induced reactions on low Z structural

Moment	$\nu_1 = \bar{\nu}$	$\nu_2 = \overline{\nu(\nu-1)}$	$\nu_3 = \overline{\nu(\nu-1)(\nu-2)}$
^{235}U	2.406	4.626	6.862
^{239}Pu	2.879	6.773	12.630
^{241}Pu	2.929	N/A	N/A

Table 1.1: Neutron Multiplicity Moments for Fissile Isotopes ^{235}U, ^{239}Pu and ^{241}Pu.

or bonded material such as (α,n) on oxygen and fluorine. These source neutrons have the possibility of inducing reactions, (n,fxn) and (n,xn), that begin a fission neutron chain.

By knowing the spontaneous fission rate of fissile material, the (α,n) cross section of other isotopes the actinides are bonded to (i.e. oxygen, fluorine), and the average fission neutron multiplicity, $\bar{\nu}$; the isotopic composition of the sample can be inferred and related to the declared enrichment [27]. In the case of spent fuel monitoring, the burn-up of the reactor must be modeled using a Monte-Carlo approach and declaration of reactor conditions from the host site. The largest limitation in this approach is the multiplicity for fissile material in the sample is assumed from the moments of thermally induced fission. Due to the similarities in the $\bar{\nu}$ for thermal induced fission for ^{239}Pu and ^{241}Pu large counting times are needed to determine the isotopic composition of a given sample [37]. Accounting for the multiplicity moment at all possible induced neutron energies, not just thermal, would increase the efficacy of these techniques.

Attribution of Interdicted Nuclear Material

Each nuclear facility is responsible for the security and safeguards of the nuclear material under its control. In the case that nuclear material is interdicted through the black market, from an unattended location, a nefarious actor etc., attribution of the material is important to identify any vulnerabilities in nuclear safeguards or security practices. Moreover, robust nuclear forensics techniques serve as a deterrent to facilities or countries from violating the Treaty on the Non-Proliferation of Nuclear Weapons and providing nuclear material to groups or organizations not entitled to poses them. The IAEA identifies three main objective for nuclear forensics [22]:

1. Determine what the materials are.
2. Determine the origin of the material such as the location, time, and process used to fabricate the material.
3. Determine the intended end use of the material.

Although these objectives are rather broad, nuclear material exists in many forms, compositions, and isotopic concentrations. As a result, nuclear forensics requires a diverse set of

tools and analysis methods to determine attribution. In the case that samples originating from a reactor were interdicted, the isotopic composition would give insight to the reactor from which it originated if the appropriate nuclear data were available. As mentioned in the previous subsection, (n,xn) and (n,fxn) reactions are needed for nondestructive assay of nuclear materials, which has overlaps in nuclear forensics. Additionally, the reaction network shown in Equation 1.1 demonstrates how the (n,xn) reactions directly feed into the production of specific isotopes within a reactor. The rates for these reactions are dependant on the incident neutron's energy relative to the neutron separation energy. The transmutation of nuclear fuel occurs when actinides capture neutrons, and either undergo beta decay or (n,xn) reactions. If the material composition can be identified through other means, the additional knowledge of the behavior of (n,2n) reactions gives insight to the neutron fluence and energy spectra of the reactor which can help to pin point a specific location of origin.

1.2 Previous Experiments

To date only three measurements have sought to identify the prompt fission neutron multiplicity for ^{241}Pu, while none have attempted to find the (n,xn) cross section. The (n,xn) and (n,xnf) quantities for other actinides have been measured through a variety of methods. Currently induced neutron reaction measurements fall into three categories: radio-chemistry methods, direct counting of neutrons, and partial gamma-ray detection. Of the three mentioned, prompt fission neutron multiplicities are only measured using direct counting of neutrons.

Radio-chemistry

The (n,2n) cross-sections for ^{239}Pu and ^{241}Am were previously measured by R. W. Lougheed et. al. using a 14-MeV neutron source from the Insulated Core Transformer (ICT) [28]. These neutrons were created through a ^{3}H(d,n)^{4}He reaction from a deuteron beam incident on tritium-impregnated titanium. Two reference foils, gold and iron, were used to monitor the neutron flux and energy respectively. Gold was a suitable reference reaction because ^{197}Au(n,2n)^{196}Au cross section is constant over the energies of interest and is well characterized. The ^{54}Fe(n,p)^{54}Mn reaction has a high sensitivity to the incident neutron temperature and was used to confirm the neutron energy. To determine how much ^{240}Am was created through (n,2n) a Ge(Li) detector was used to measure the 988, 662, and 722 keV gamma-rays. However, following irradiation, the plutonium target was dissolved and electroplated onto platinum disks to reduce the self shielding from emitted alpha particles. After one year of counting enough statistics from the ^{238}Pu characteristic 5.50 MeV alpha particle were detected to deduce a cross section. The detected counts can be used to infer a cross section.

$$R_{\alpha} = R_{c} * \frac{\lambda_{238}\Delta t_{rt}}{1 - e^{-\lambda_{238}\Delta t_{rt}}} \tag{1.2}$$

Here, R_α refers to the alpha rate at the beginning of counting, R_c is the counted alpha rate over the real time of the measurement Δt_{rt}, and λ_{238} is the decay rate for ^{238}Pu. The alpha rate at the end of irradiation, $R_{\alpha,0}$ is then determined using the time since irradiation,Δt:

$$R_{\alpha,0} = R_\alpha e^{+\lambda_{238}\Delta t} \tag{1.3}$$

The rate of alpha emission to the number density of ^{238}Pu at the end of irradiation, N_{Pu238}, are then related by correcting for the efficiency of the detector and the the branching ratio,BR of the alpha detector,ϵ_α.

$$N_{Pu238} = \frac{R_{\alpha,0}}{\epsilon_\alpha \lambda_{238} BR} \tag{1.4}$$

Finally, the (n,2n) cross section for ^{239}Pu can be inferred using the following ratio:

$$\sigma_{Pu239(n2n)} = \frac{N_{238/239}}{N_{196/197}} \sigma_{Au196(n2n)} \tag{1.5}$$

Here $N_{238/239}$ and $N_{196/197}$ refer to the ratios of ^{238}Pu/^{239}Pu and ^{196}Au/^{197}Au in the samples, and σ refers to the cross section for the reactions of interest.

These methods are appropriate for measuring cross sections at a specific energy. Due to neutron energies available through ^{3}H(d,n)^{4}He and ^{2}H(d,n)^{3}He reactions, the incident neutron energy is limited. Additionally, at higher energies other light particles reactions such as (n,d) become feasible producing the intended daughter product of interest for (n,2n):

$$n + {}^{239}Pu \xrightarrow{d} {}^{238}Np \xrightarrow[2.117d]{\beta-} {}^{238}Pu \qquad (Q_{val} = 3.947MeV) \tag{1.6}$$

For isotopes without easily observable gamma-ray lines, alpha counting would be too time consuming. To determine the (n,2n) cross section in 500 keV bins from 0-20 MeV would take roughly 40 years of effort. Lastly, using this method for ^{241}Pu would require a pure target, which is difficult to produce.

Direct Neutron Counting

The onset of in-beam energy dependant (n,xn) cross sections and neutron multiplicity measurements occurred shortly after the development of doped liquid scintillators by Cowan and Reines to detect antineutrinos [38]. Of the subsequent experimental campaigns, the most notable was Frehaut et. al. using the 14 MeV Tandum Van de Graff accelerator [16]. A pulsed neutron beam was created using a gaseous target through ^{3}H(d,n)^{4}He reactions. A fission chamber was used to identify fission events. Following a neutron pulse, neutrons were detected as either fission neutron or (n,xn) candidates using a large gadolinium doped scintillator. The detected neutron spectrum in the detector was assumed to follow a binomial distribution with a 90% efficiency. Fission neutrons were correlated to events in the fission chamber. To differentiate (n,xn) neutrons from fission neutrons, the known distribution of

fission neutrons, N_f, with the probability to emit x neutron, $P(x)$, must be subtracted from the experimental number of fission neutrons:

$$N_x = N(x) - N_f P(x) \tag{1.7}$$

Once the fission neutron multiplicity was subtracted, the resulting (n,xn) reactions were determined as a ratio to the detected fission counts and the known neutron induced cross-section for fission:

$$\sigma_{n,xn} = \frac{N_{xn}}{N_f}\sigma_f \tag{1.8}$$

Systematic and statistical errors influenced both the fission neutron multiplicity and the (n,2n) cross section. In the plutonium measurements thick samples of plutonium metal led to high random backgrounds from the activity of the sample and the spontaneous fission rate of ^{240}Pu. Moreover, neutrons could be down scattered in the target inducing multiple reactions such as (n,2n) and (n,f). Additionally,the aluminum cladding in the experiment led to high rates of correlated single neutron detection. At the time of the measurements the ^{252}Cf $\bar{\nu}$=3.733 $\pm$ 0.022 , while the current consensus value is $\bar{\nu}$=3.7692 $\pm$ 0.0047. Because ^{252}Cf is used to calibrate the array's neutron efficiency, this discrepancy propagates in each detected neutron multiplicity and in the ratio to fission neutrons of multiplicity three and four used as a ratio. The experimental concerns that only effected the (n,2n) cross section included the neutron detection efficiency for (n,2n) should be modified to incorporate the emitted neutron spectrum [29].

Partial Gamma-Ray Detection

The partial gamma-ray detection method was meant to be an improvement on the direct neutron counting. Becker et. al. measured the (n,2n) cross section for ^{239}Pu as a function of E_n using a "white" neutron source produced by LANCE (Los Alamos Neutron Science Center)[3]. The variable incident neutron energy for the reaction was determined using neutron time-of-flight between the beam pulse and interaction time. The (n,2n) events were determined by measuring the characteristic gamma-rays from the excited states of ^{238}Pu with the GEANIE (GErmanium Array for Neutron Induced Excitations) detector, which consisted of 26 high-resolution Gemanium detectors [4]. In addition to ^{239}Pu target, iron foils were used and the ^{56}Fe(n,n'γ_{847}) cross-section was used as a reference reaction at 14 MeV. By detecting the characteristic gamma-rays from ^{238}Pu, the uncertainties due to the neutron background from beam induced reactions, beam captures in the detector, and competing reactions producing neutrons are removed.

The cross-section was determined by including the partial gamma-ray cross sections: (157.4 keV, $6^+ \rightarrow 4^+$), (936.6 keV, $4^- \rightarrow 4^+$), (918.7 keV, $1^- \rightarrow 2^+$), (924.0 keV, $2^- \rightarrow 2^+$), and (617.3 keV, $5^- \rightarrow 6^+/3^- \rightarrow 4^+$). The partial cross sections were corrected using the

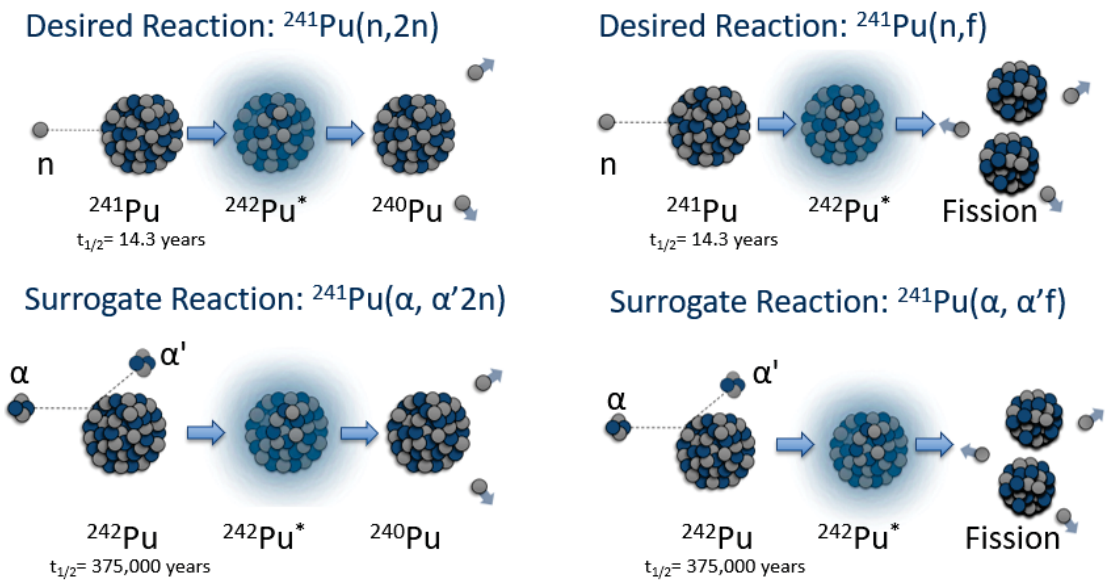

Figure 1.1: Surrogate reactions for neutrons induced neutron emission through (n,xn) and (n,fxn) on ^{241}Pu. The neutron beam is substituted with an α beam and the target is ^{242}Pu.

enhanced Hauser-Feshbach model:

$$\sigma(n,2n) = \sum_{\gamma i} \sigma^{exp}(n,2n\gamma_i) \times \frac{\sigma^{model}(n,2n)}{\sum_{\gamma i} \sigma^{model}(n,2n\gamma i)} \tag{1.9}$$

In this experiment the lowest gamma ray transition used was the (157.4 keV, $6^+ \rightarrow 4^+$). The (44.1 keV, $2^+ \rightarrow 0^+$) transition, which carries 90% of the (n,2n) cross section decayed primarily through internal conversion. Additionally, the (101.9 keV, $4^+ \rightarrow 2^+$) transition was contaminated by fission gamma-rays. Using the partial gamma ray method requires a strong reliance on theoretical models because most of the intense branches were undetectable including reactions that leave ^{238}Pu in its ground state. Again, this method requires pure targets, and would not be suitable for short-lived isotopes.

1.3 Surrogate Reactions

The common systematic and statistical uncertainties associated with (n,xn) and (n,fxn) measurements on actinides are both beam and target related. To circumvent the use of a ^{241}Pu target and large background subtractions from using a neutron beam and neutron detection, a surrogate is introduced [13]. Figure 1.1 illustrates the use of surrogate reactions in this experiment. The desired reaction is a neutron incident on ^{241}Pu to create the compound nucleus ^{242}Pu with the desired exit channels of multiple neutron emission from fission or

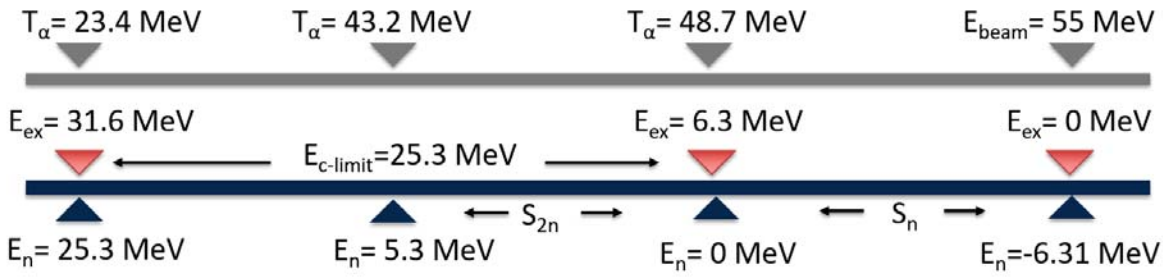

Figure 1.2: Energy diagram relating the detected α particle energies to the excitation energy and equivalent neuton energy for ^{242}Pu(α,α') reactions for a 55 MeV beam

evaporation. By using an alpha particle incident on ^{242}Pu ($t_{1/2} = 375,000$ years), the nucleus can be in-elastically promoted to the same excited state. The resulting nucleus is then expected to decay in the same manner as if it had been produced by neutron capture. By detecting the energy of the scattered alpha particle, T_α, the excitation energy of the compound nucleus, can be deduced and related to the energy of the equivalent neutron energy, E_n:

$$E_n = E_{beam} + Q - T_\alpha - S_n - R \tag{1.10}$$

Here, E_{beam} is the energy of the incident alpha beam, Q, is the Q-value for the reaction which reduces to zero for inelastic scattering reactions where the projectile remains intact, R is the recoil energy of the target nucleus, and S_n is the neutron separation energy. Figure 1.2 shows the energy relation between the measured and desired quantities. The higher neutron separation energy relative to the Q value for this reaction allows "negative" equivalent neutron values to be probed. For this reaction the upper limit on E_n is determined by the Coulomb limit, E_c [25]:

$$E_c = \frac{kq_\alpha q_{Pu-242}}{r} \tag{1.11}$$

where k is Coulomb's constant, r is the sum of the two nuclei radii, and q_i is the charge of the sub-scripted nucleus. The maximum equivalent neutron energy that can be attained using this reaction is 25.3 MeV. Once the Coulomb barrier is surpassed inelastic reaction are in direct competition with fusion induced events. When using experimental data further corrections to energy loss of α particles in the dead layers are incorporated.

Utilizing surrogate reactions to measure quantities of interest for short-lived nuclei has previously incorporated transfer reactions (d,p), stripping reactions (p,t), and inelastic scattering (p,p') to measure (n,γ), (n,f), and fission fragment anisotropies. This technique has never been applied to fission neutron multiplicities or (n,xn) measurements until the present work. Light ions are preferentially used due to the low angular momentum transfer. Transfer reactions such as (d,p) would not be suitable for this experiment, because the ^{241}Pu target would still be used. Additionally, the low binding energy of the deuteron would create a large neutron background. Inelastic scattering of protons on ^{242}Pu would require very thick

silicon detectors to stop the proton and measure the outgoing particle energy. Due to the half-life of neighboring isotopes stripping reactions with ^3He or p are unfeasible. Thus, the inelastical scattering of alpha particles was the most suitable surrogate for this measurement.

Chapter 2

Nuclear Reaction Theory

2.1 Nuclear Reactions

In the case of particle a incident on a heavier nuclei X:

$$a + X \longrightarrow b + Y \tag{2.1}$$

where b and Y are the reaction products, the angular momentum, parity, energy, and total nucleons must conserve the properties of their parent nuclei. Within these confines of the conservation constraints the energy of the incident particle influences the reactions mechanisms in which the particles interact further determining the energy distribution of the products. Moreover, by understanding the characteristics of nuclear processes, features in energy spectra are indicative of the reactions of interest. Figure 2.1 illustrates the reaction network available for light ions incident on a target nucleus.

Elastic Scattering

When the incident particle's energy is insufficient to reach the excited state of the target nuclei, or below the Q value for the evaporation of particles and fission; the elastic scattering channel is favored. In this reaction Equation 2.1 becomes:

$$a + X \longrightarrow a + X \tag{2.2}$$

and the internal energy of the constituent particles remains the same. In the case that the projectile a is a charged particle, both parents experience the Coulombic repulsion. When the light ion is far from the nucleus it follows a trajectory, dependant on $m_a \rho v_{a,0}$ and the impact parameter, as the particle approaches the target nucleus the nucleus will exchange some kinetic energy for potential energy and follow a hyperbolic trajectory around the distance of closest approach [25]. The resulting trajectory of the final nuclei must conserve the momentum of the initial particle, $m_a \rho v_{a,0}$. The differential cross-section, $\frac{d\sigma}{d\Omega}$, for this

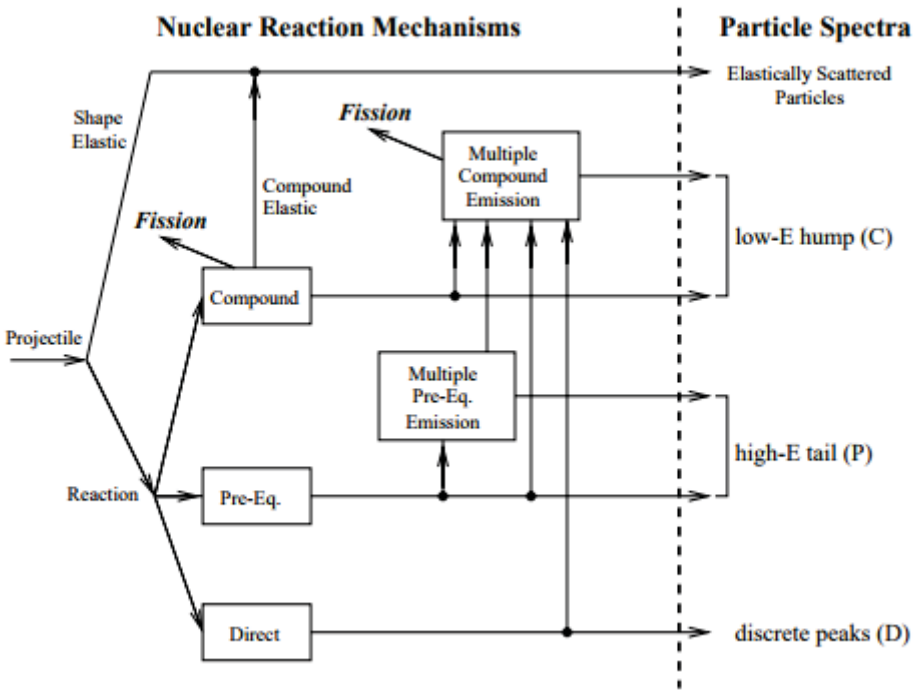

Figure 2.1: Diagram of reaction channels for light ions incident on heavier targets retrieved from Reference [24]. Each reaction channel weather elastic, direct, pre-equilibrium or compound; results in the emission of particles with characteristic energetic features.

reaction is described below [25].

$$\frac{d\sigma}{d\Omega} = \left(\frac{Z_a Z_x e^2}{4\pi\varepsilon_0}\right)^2 \left(\frac{1}{4T_a}\right)^2 \frac{1}{\sin^4 \frac{\theta}{2}} \tag{2.3}$$

Here Z is the charge of the individual nuclei, $e^2/4\pi\varepsilon_0$ is the fine structure constant, T_a is the kinetic energy of particle a, and θ is the outgoing angle. In experiments probing the nuclear interactions with large nuclei, placing detectors at large angles would significantly reduce Rutherford scattering events. For higher energy particles and neutrons the Coulombic scattering terms should be added with nuclear scattering cross-sections.

Discrete Excitation

During inelastic scattering, the target nucleus can be scattered to discrete excited states, i.

$$a + X \longrightarrow a + X + \sum_i \gamma_i \tag{2.4}$$

This process occurs at higher energies, 200 keV<E< 4 MeV, than where elastic scattering is dominant, E <200 keV. Due to the direct population of discrete states, there is no intermediate transition, and the nucleus decays based on the life-time of the excited state populated. The excited target will decay through the emission of characteristic gamma-rays. When the scattered light particle is detected at a fixed angle, there are discrete peaks corresponding the the location of excited states. These peaks are used to probe the nuclear structure of specific isotopes.

Compound Reactions

At medium nuclear energies $E < 50$ MeV reactions are dominated by compound reactions. Here, the de Broglie wavelength of the projectile is significantly larger than those of individual nucleons. Thus, it can only interact with the nucleus on a whole. In compound reactions the products form an intermediate state.

$$a + X \longrightarrow C^* \longrightarrow Y + b \tag{2.5}$$

In the compound nucleus C^* the excitation energy is shared among all nucleons forming a statistical equilibrium. These reactions are two step processes that entail the formation and decay of the compound nucleus [24]. Due to the time-scale of this interaction. $10^{-15} - 10^{-14}$s, compared to nuclear time scales, $10^{-21} - 10^{-17}$s, the compound nucleus will "forget" its formation and decay due to its statistical properties. By relying on the statistical properties of the compound nucleus, the angular momentum of any evaporated particles are isotropic and their energies follow a Gaussian distribution. The probability of evaporating particles is directly related to their separation energy, and rises and falls due to the energetic availability of other emission channels.

The Hauser-Feshbach formalism for compound reactions is heavily employed for theorizing the cross-section for a reaction under consideration [18].

$$\frac{d\sigma_{aX\to bY}}{dE_{bY}} = \pi\grave{\lambda}^2_{aX}\sum_{J\pi}\omega^J_{aX}\sum_{lsl's'I''}\frac{T^J_{aXls}T^J_{bYl's'}\rho_{I'}\left(U'\right)W_{aX\to bY}\left(J\right)}{\left(\sum'_{bY''l''s''}T^J_{bY''l''s''}+\sum'_{bY''l''s''I''}\int T^J_{bY''l''s''}\left(E_{bY''}\right)\rho_{I''}\left(U''\right)dE_{bY''}\right)} \tag{2.6}$$

Here, aX refers to the entrance channel $a+X$, and bY the exit channel for the Equation 2.5. The first terms that include $\pi\grave{\lambda}^2_{aX}\sum_{J\pi}\omega^J_{aX}$ represent the probability of forming a compound nucleus; where $\grave{\lambda}^2$ is the reduced wavelength, and ω^J is the statistical weighting factor. The rest of the equation represents the decay of the compund nucleus as described by:

1. Decay of the compound nucleus into statistical states of interest in the residual nucleus: $T^J_{aXls}T^J_{bYl's'}\rho_{I'}\left(U'\right)W_{aX\to bY}\left(J\right)$
2. Decays into discrete levels in the residual nuclei: $\sum'_{bY''l''s''}T^J_{bY''l''s''}$

3. Decays into regions described by a level density in the residual nuclei:
$\sum'_{bY''l''s''I''} \int T^J_{bY''l''s''} (E_{bY''}) \rho_{I''} (U'') dE_{bY''}$

In these terms l, l' describes the orbital momentum, s, s' refers to the channel spin, of the initial and final states, and I' describes the spin of the target nucleus. Additionally, T^J and $\rho_{I''} (U'')$ describes the transmission coefficient and level densities of spin I' at excitation U'. Note that in the Hauser-Feshbach formalism, all terms in the probability to form the compound nucleus are independent of the decay terms.

Pre-Equilibrium

As the name suggests, pre-equilibrium reactions occur when the nucleus has not formed a compound state and the reaction proceeds without an intermediate step [24].

$$a + X \longrightarrow b + Y \tag{2.7}$$

The wavelength of an incident particle decreases with increasing energies, such that it no longer interacts with the nucleus as a whole. In this case it can "see" individual nucleons, specifically valence nucleons on the nuclear surface. During these reactions, the energy transfer is not shared among the entire nucleus, as it does not reach a statistical equilibrium. Here the energy imparted on the bound nucleon, exceeds its separation energy and can then be liberated from the nucleus. Additionally, the short-time scales and the direct component of this reaction does not allow the nuclear to "forget" its formation, and is highly dependent on the statistical properties of the incident nuclei. Thus, the emitted particles have a high energy tail as their emission energy is correlated to the incident particle. During these interactions, individual nucleons can be emitted, and the resulting nucleus can form a compound nucleus. In this case the resulting compound nucleus will decay as described in the previous section.

2.2 Surrogate Theory

If the formation of a compound nucleus is independent of the decay, then the cross-section for a reaction of interest can be determined by simplifying Equation 2.6 to the sum of the cross-sections constituent parts [14]:

$$\sigma_{aX \to bY} (E_a) = \sum_{J,\pi} \sigma^{CN}_{aX} (E_{ex}, J, \pi) G^{CN}_{bY} (E_{ex}, J, \pi) . \tag{2.8}$$

The cross-section for forming a compound nucleus $\sigma (a + X \to C^*)$, at excitation energy E_{ex} for a given angular momentum and parity J and π is described by $\sigma^{CN}_{aX} (E_{ex}, J, \pi)$. The branching ratio for the decay of interest for the residual nucleus energy and quantum states is denoted by $G^{CN}_{bY} (E_{ex}, J, \pi)$. For reactions of interest, where the measurement of $\sigma_{aX \to bY} (E_a)$ is not experimentally feasible due to beam or target conditions, the quantity $G^{CN}_{bY} (E_{ex}, J, \pi)$

can readily be measured through the use of a surrogate reaction, δ. Instead of using the compound reaction in Equation 2.5, the surrogate is expressed as:

$$d + Z \longrightarrow C^* \longrightarrow b + Y, \tag{2.9}$$

where the cross-section for forming the compound nucleus through this reaction is given by $F_\delta^{CN}(E_{ex}, J, \pi)$. The probability for the entire reaction is then written as:

$$P_{\delta \to bY}(E_\delta) = \sum_{J,\pi} F_\delta^{CN}(E_{ex}, J, \pi)\, G_{bY}^{CN}(E_{ex}, J, \pi). \tag{2.10}$$

Weisskopf-Ewing Approximation

During experimental measurements, where the emitted particle of interest is not a gamma-ray, determining the angular momentum and parity of individual states becomes difficult. In these cases the Weisskopf-Ewing limit to the Hauser-Feshbach formalism is implemented [47]:

- The energy of the compound nucleus is sufficiently high that the decay into discrete channels is determined by the integral over the level states.
- Due to the first condition, dependence on width fluctuations become negligible.
- The transmission coefficients are independent of the spin of the states in the target nucleus.
- The spin dependencies of each level density is not dependent on the parity.

In short the Weisskopf-Ewing limit removes dependencies on angular momentum and parity. Using these assumptions Equation 2.8 can be reduced:

$$\sigma_{aX \to bY}(E_a) = \sigma_{aX}^{CN}(E_{ex})\, G_{bY}^{CN}(E_{ex}). \tag{2.11}$$

For surrogate reactions this the cross section becomes:

$$P_{\delta \to bY}(E_\delta) = \sigma_\delta^{CN}(E_{ex})\, G_{bY}^{CN}(E_{ex}). \tag{2.12}$$

Following the implementation of the Weisskopf-Ewing limit, the cross section can be determined through absolute means or through a ratio. In both measurements the branching ratio of decay into the state of interest can be determined experimentally by measuring the occurrence of surrogate reactions, N_δ, the emitted particle of interest, $N_{\delta bY}$, and the efficiency of measuring the exit particle, ε_{bY}:

$$G_{bY}^{CN}(E_{ex}) = \frac{N_{\delta bY}}{N_\delta \varepsilon_{bY}} \tag{2.13}$$

For absolute measurements the probability of forming the compound nucleus is determined through Optical models [13].

Internal Surrogate Ratio

In an effort to remove the dependencies on precisely measuring the quantity N_δ in Equation 2.13, another surrogate reaction can be introduced to form a ratio [13].

$$R = \frac{\sigma_{\delta 1 \to bY2}}{\sigma_{\delta 2 \to bY2}} \tag{2.14}$$

The subscripts $\delta 1$ and $\delta 2$ refer to the surrogate ratio of interest and the one implemented for a ratio respectively. The ratio can be expanded using the Weisskopf-Ewing limit:

$$R(E_{ex}) = \frac{\sigma^{CN}_{\delta 1}(E_{ex}) G^{CN}_{bY1}(E_{ex})}{\sigma^{CN}_{\delta 2}(E_{ex}) G^{CN}_{bY2}(E_{ex})} \tag{2.15}$$

Substituting the G^{CN} with the terms defined in Equation 2.13 yields an experimentally relevant ratio $R^{exp}(E)$:

$$R^{exp}(E) = \frac{\sigma^{CN}_{\delta 1}(E_{ex}) N_{\delta 1bY}(E_{ex}) N_{\delta 2}(E_{ex})}{\sigma^{CN}_{\delta 2}(E_{ex}) N_{\delta 1}(E_{ex}) N_{\delta 2bY}(E_{ex})} \frac{\varepsilon_{bY2}(E_{ex})}{\varepsilon_{bY1}(E_{ex})} \tag{2.16}$$

Given the efficiency and systematic errors are consistent within an experiment the efficiency terms are equal. Additionally, the number of observed reference reactions are scaled to match the number of surrogate reactions.

$$R^{exp}(E) = \frac{\sigma^{CN}_{\delta 1}(E_{ex}) N_{\delta 1bY}(E_{ex})}{\sigma^{CN}_{\delta 2}(E_{ex}) N_{\delta 2bY}(E_{ex})} \tag{2.17}$$

An ideal reference reaction for a surrogate reaction uses another target nucleus with similar nuclear properties. Under these conditions, it can be assumed that $\sigma^{CN}_{\delta 1}(E_{ex}) = \sigma^{CN}_{\delta 2}(E_{ex})$. The ratio of the two cross sections are then equal to the ratio of the detected projectiles.

$$\frac{\sigma_{aX_1 \to bY_1}}{\sigma_{aX_2 \to bY_2}} = \frac{N_{\delta 1bY}(E_{ex})}{N_{\delta 2bY}(E_{ex})} \tag{2.18}$$

The cross section for the reaction of interest is then determined by taking the ratio of the surrogate projectiles to the reference reaction projectiles multiplied by the known cross section for the direct reference reaction. Note, the reference reaction cross section is typically a known quantity and should have low uncertainties.

$$\sigma_{aX_1 \to bY_1} = \frac{N_{\delta 1bY}(E_{ex})}{N_{\delta 2bY}(E_{ex})} \sigma_{aX_2 \to bY_2} \tag{2.19}$$

The use of a reference reaction with a different nucleus relies on the assumption that $\sigma^{CN}_{\delta 1}(E_{ex}) = \sigma^{CN}_{\delta 2}(E_{ex})$. In the case a reference reaction with similar statistical properties is not available, an internal ratio may be applied. In this case the same surrogate is used to form the same compound nucleus, but the decay channel differs, G^{CN}_{cZ}.

$$R(E_{ex}) = \frac{\sigma^{CN}_{\delta}(E_{ex}) G^{CN}_{bY}(E_{ex})}{\sigma^{CN}_{\delta}(E_{ex}) G^{CN}_{cZ}(E_{ex})} \tag{2.20}$$

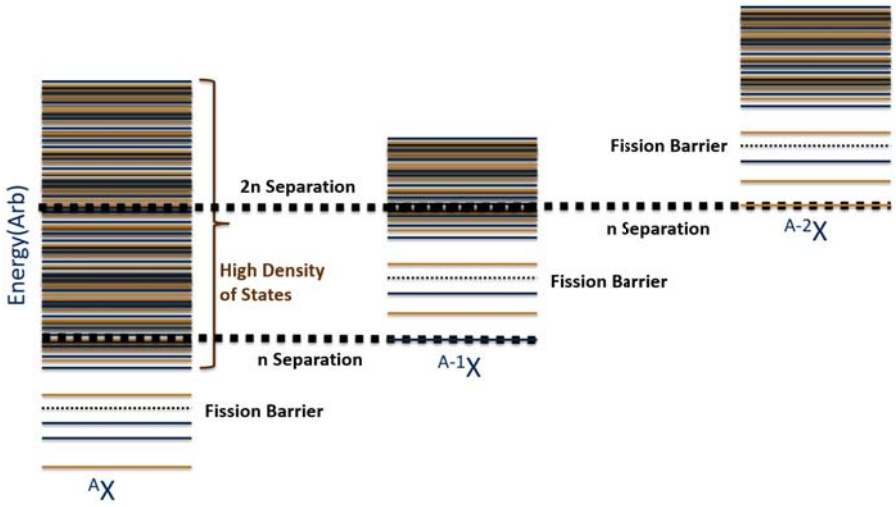

Figure 2.2: Illustration of the excitation energy for a hypothetical compound nucleus A^X. Blue lines represent states accessible through surrogate reactions, while gold lines are those available through direct reactions. At high excitation energies, the nucleus has a dense population of states and the dependencies on J^π are negligible.

Again replacing the branching ratio with the terms in Equation 2.13. The ratio for an internal surrogate reaction is then:

$$R^{exp}(E) = \frac{\sigma_\delta^{CN}(E_{ex})N_{\delta bY}(E_{ex})N_\delta(E_{ex})}{\sigma_\delta^{CN}(E_{ex})N_\delta(E_{ex})N_{\delta cZ}(E_{ex})}\frac{\varepsilon_{cZ}(E_{ex})}{\varepsilon_{bY}(E_{ex})} \tag{2.21}$$

When using an internal ratio, the reference reaction does not need to be scaled up, and can be canceled without manipulation.

$$\sigma_{aX\to bY} = \frac{N_{\delta bY}(E_{ex})}{N_{\delta cZ}(E_{ex})}\frac{\varepsilon_{cZ}(E_{ex})}{\varepsilon_{bY}(E_{ex})}\sigma_{aX\to cZ} \tag{2.22}$$

2.3 Limitations to Surrogate Reactions

Although, the surrogate method provides a convenient alternative to measuring the cross-sections and decay properties of unstable nuclei, there are constraints to this approach that are often addressed during the analysis of the measurement, or subsequently through modeling efforts. The Weisskopf-Ewing approximation, which is heavily employed during surrogate measurements is only valid for a highly excited nucleus. At low excitation energies the reactions pathways are limited by the J^π of the available states. For instance, if the J^π of the surrogate is significantly different than that of the direct reaction, at low excitation energies there is a low density of quantum states [17].

Consider that the surrogate reaction does not have the necessary spin or parity to access an energetically allowed state that would decay into the reaction of interest. The cross section for the surrogate will be significantly different than the direct reaction especially if the direct reaction can excite the nucleus to most of the states of interest. The same is true in the reversed case. As a result, discrepancies between surrogate reactions and direct reactions at sub-barrier energies, $E_{ex} < 2$ MeV. An illustration of this effect is seen in Figure 2.2. When a compound nucleus approaches a separation energy it may experience compound emission. If that emission further leads to the reaction of interest, (i.e. measuring fission after second chance fission.), the process does not satisfy the Weisskopf-Ewing due to the state of the residual nucleus following evaporation.

Recall, from Figure 2.1 at higher incident particle energies the interaction only involves individual nucleons and not the entire nucleus. The surrogate method is used to create the same compound nucleus, thus is inherently incapable of compensating for pre-equilibrium particle emission. Moreover, if the surrogate projectile is lighter than that of the direct reaction, the pre-equilibrium contribution from the surrogate must be considered when determining the cross section.

Chapter 3

NeutronSTARS Characterization

The experiment took place using the NeutronSTARS (**Neutron S**ilicon **T**elescope **A**rray for **R**eaction **S**tudies) detection array located at the Texas A&M Cyclotron Facility [2]. This array was commissioned for this experimental campaign. The NeutronSTARS, shown in Figure 3.1, allows for in-beam, low-energy-nuclear-reaction measurements that result in the emission of neutrons. The target chamber, referred to as the STARS chamber, contains a silicon telescope consisting of thin ΔE and thick E Micron S2 type annular silicon detectors to probe the energy transfer in a given reaction through the detection of light charged ions, and a fission silicon detector to detect fission fragments and identify fission events [31]. A large segmented volume filled with gadolinium-doped liquid scintillator, referred to as NeutronBall surrounds the target chamber to detect neutrons. NeutronSTARS is located in Cave 4 of the Texas A&M University Cyclotron Institute.

3.1 Target Chamber

The NeutronSTARS target chamber facilitated the in beam observations and the medium energy reactions during the experiment. The outer dimensions of the physical chamber are 47.3 cm x 31.1 cm x 21.6 cm (18.625 in x 12.25 in x 8.50 in) and is made entirely of 3.8 cm (1.5 in) thick aluminum. Encased in the chamber are a target wheel with eight target positions and a remotely controlled motor, a silicon telescope, a silicon fission detector, an LED light, and a micro CCD camera. A picture of the physical target chamber is shown in Figure 3.2. Aside from the silicon telescope and fission detector, the other features in the target chamber facilitate experimental operations. The LED and micro CCD camera allow for observation of the beam spot when fluorescence targets are loaded for beam tuning. To amplify the signals while minimizing noise, a pre-amp rack is located next to the chamber in copper boxes. The pre-amp board and fans are powered through nearby power supplies.

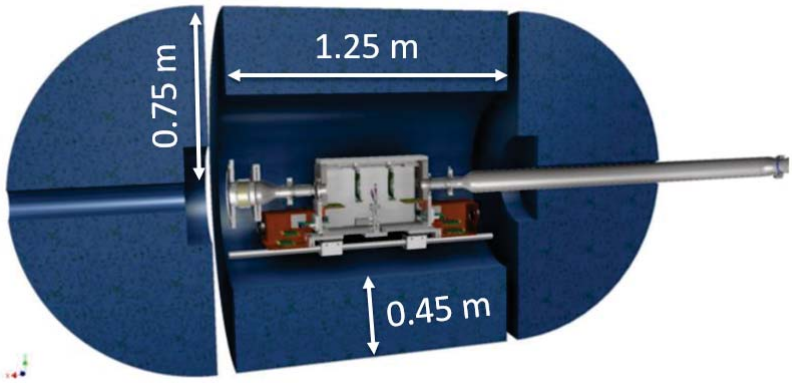

Figure 3.1: CAD drawing of the NeutronSTARS array. The NeutronBall is comprised of a central cylinder segmented into four quadrants and two hemispherical endcaps. Each endcap has four PMTs while the four central cylinder segments each have three PMTs, making 20 PMTs in total. The scattering chamber has an upstream fission detector and downstream silicon telescope. The silicon detector signals are amplified close to the target chamber in pre-amplifiers housed in copper boxes.

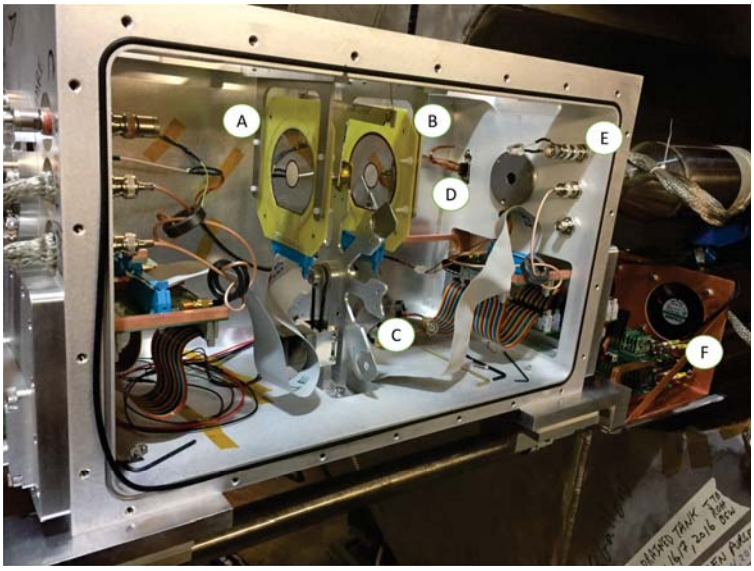

Figure 3.2: Opened target chamber used in the NeutronSTARS array. The silicon telescope [A], down stream fission detector [B], a target wheel [C], LED [E] and micro CCD camera [D]. A copper box containing pre-amplifier boards and cooling fans are located on both sides of the target chamber [F].

CAEN Input	**1**	**3**	**5**	**7**	**9**	**11**	**13**	**15**
Signal Cable	A1	A2	A3	A4	A5	A6	A7	A8
S/R	R1	R3	R5	R7	R9	R11	R13	R15
Original	2,4	8,6	10,12	16,14	18,20	24,22	28,26	32,30
CAEN Input	**17**	**19**	**21**	**23**	**25**	**26**	**27**	**28**
Signal Cable	A9	A10	A11	A12	A13	A14	A15	A16
S/R	R17	R19	R21	R23	S1	S2	S3	S4
Original	34,36	40,38	42,44	48,46	1,2	3,4	5,6	7,8
CAEN Input	**2**	**4**	**6**	**8**	**10**	**12**	**14**	**16**
Signal Cable	B1	B2	B3	B4	B5	B6	B7	B8
S/R	S5	S6	S7	S8	R24	R22	R20	R18
Original	9, 10	11, 12	13,14	15,16	45,47	41,43	37,39	33,35
CAEN Input	**18**	**20**	**22**	**24**	**29**	**30**	**31**	**32**
Signal Cable	B9	B10	B11	B12	B13	B14	B15	B16
S/R	R16	R14	R12	R10	R8	R6	R4	R2
Original	29,31	27,25	21,23	17,19	13,15	9,11	5,7	1,3

Table 3.1: Relation between the rings and sectors in a silicon detectors and the inputs used for one CAEN module. The Original relates to the ring and sector before the wires were bussed together. For additional modules for the other silicons the designater A and B are indexed alphabetically.

Silicon Detectors

In the current configuration three silicon detectors are used: a 140 μm fission detector to gate on fission events, a 140 μm δE detector as part of the silicon telescope to record energy loss, and a 1000 μm thick E detector as part of the silicon telescope to stop and track particle trajectories. Each detector is segmented into 48 rings (n-type) and 16 sectors (p-type) as shown in Figure 3.3. The sectors are enumerated beginning with the bottom-center-left, and continuing clockwise. The rings are organized such that the inner-most is labeled 1, while the outer-most is 48. Following a deposition read on a given sector or ring, the signals follow through the pins located on the bottom of the detector.

As seen in Figure 3.4, the readout for the sectors and rings are coupled to 8 signals from the sectors and 24 from the rings. The rings are split on the board with the odd number rings going one side and the even number rings being read out on the other side. The sectors are on the outer most pins while the rings are on the interior. These signals are then mapped to a custom board that outputs the collapsed rings and sectors. These signals are then pre-amplified before going into a CAEN shaper/amplifier. From tracing the signals from the rings and sectors through the signals on the circuit board, the detector readout used for the CAEN module is displayed in Table 3.1.

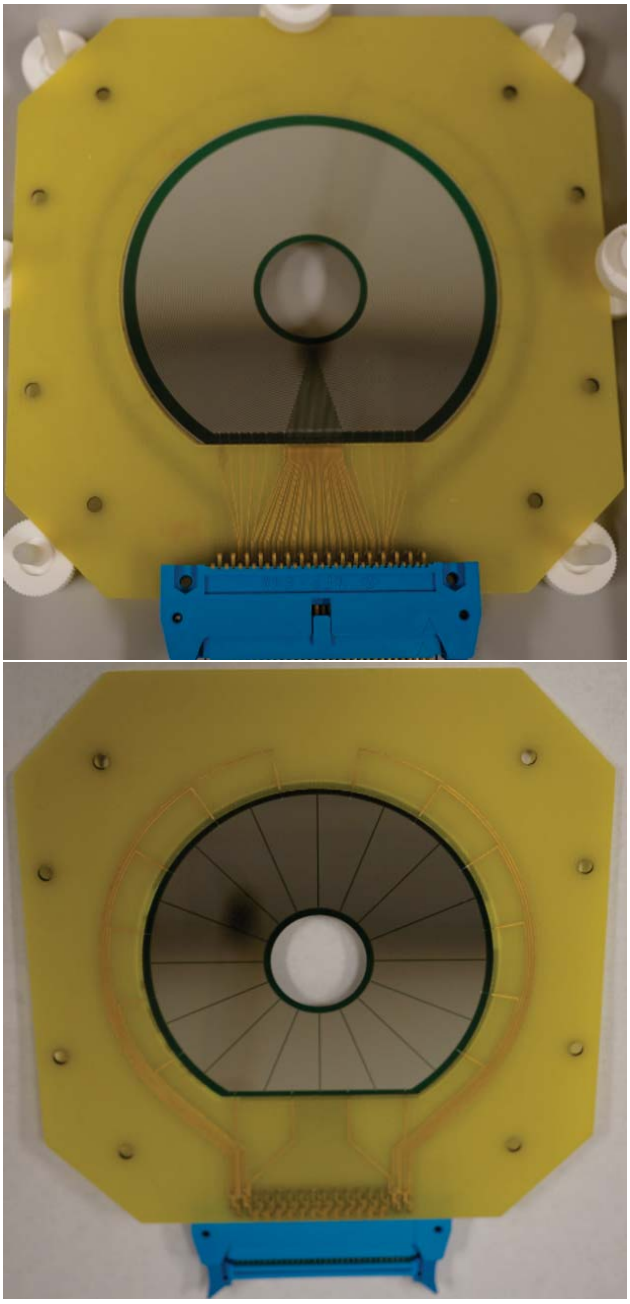

Figure 3.3: Photographs of the silicon detectors used in the silicon telescope and the fission detector. The detector consists of 48 rings [Top] and divided into 16 sectors [Bottom], but red out into 24 rings and 8 sectors.

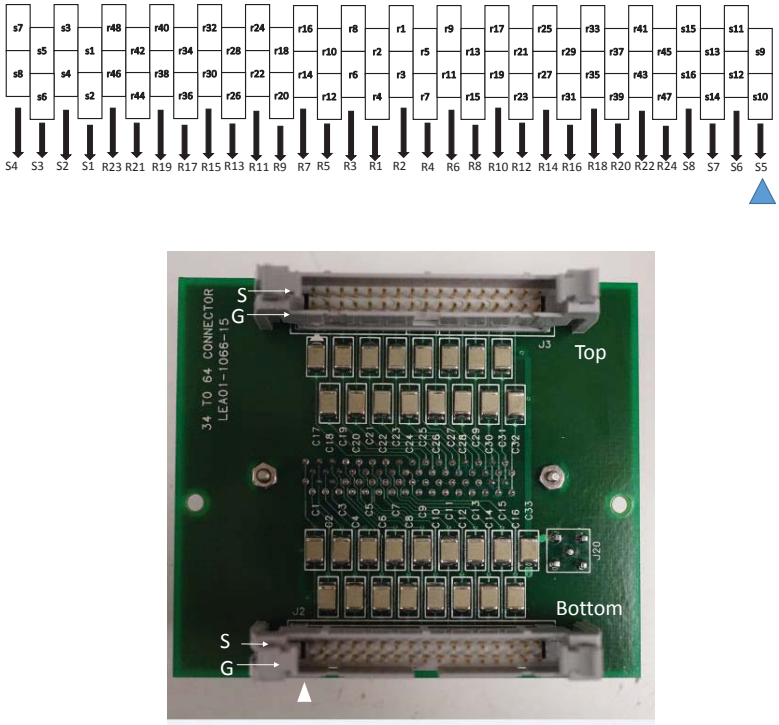

Figure 3.4: Sector and ring pins [Top]. The lowercase s denotes sector, while the lower case r is for ring for the individual markers. When the signals are combined a capital S and R are used. The blue triangle correlates to the first pin on the circuit board. Circuit board for the collapsed silicon diode detector signals [Bottom]. The S and G in white represent either the ground or signal readout. The top and bottom labels represent orientation. The white triangle shows where the first pin is located.

Silicon Detector Calibrations

The two silicon detectors that make up the silicon telescope were calibrated using a ^{226}Ra source. Known calibration lines occur at 4784, 5489, 6002, and 7686 keV from the alpha decay of ^{226}Ra, ^{222}Rn, ^{218}Po, and ^{214}Po respectively. The E detector's response to the ^{226}Ra source s shown in Figure 3.5. The energy resolution of the telescope is 55 keV (FWHM) for alpha particles at 7686 keV. Higher energy calibrations can be determined in beam using charged particles to excite targets such as lead, carbon, and mylar (oxygen and carbon). A ^{252}Cf source is used to perform calibrations to determine the fission energy threshold, and by placing the source 14 mm from the fission detector. During the experiment the actinide target is likely to undergo alpha decay, thus to eliminate false coincidences between the silicon detector a threshold to discriminate alpha particles from fission fragments is set at 40 MeV. The efficiency of the fission detector was found to be $(40.1 \pm 1.3)\%$. The spectral response of the detector can be seen in Figure 3.5.

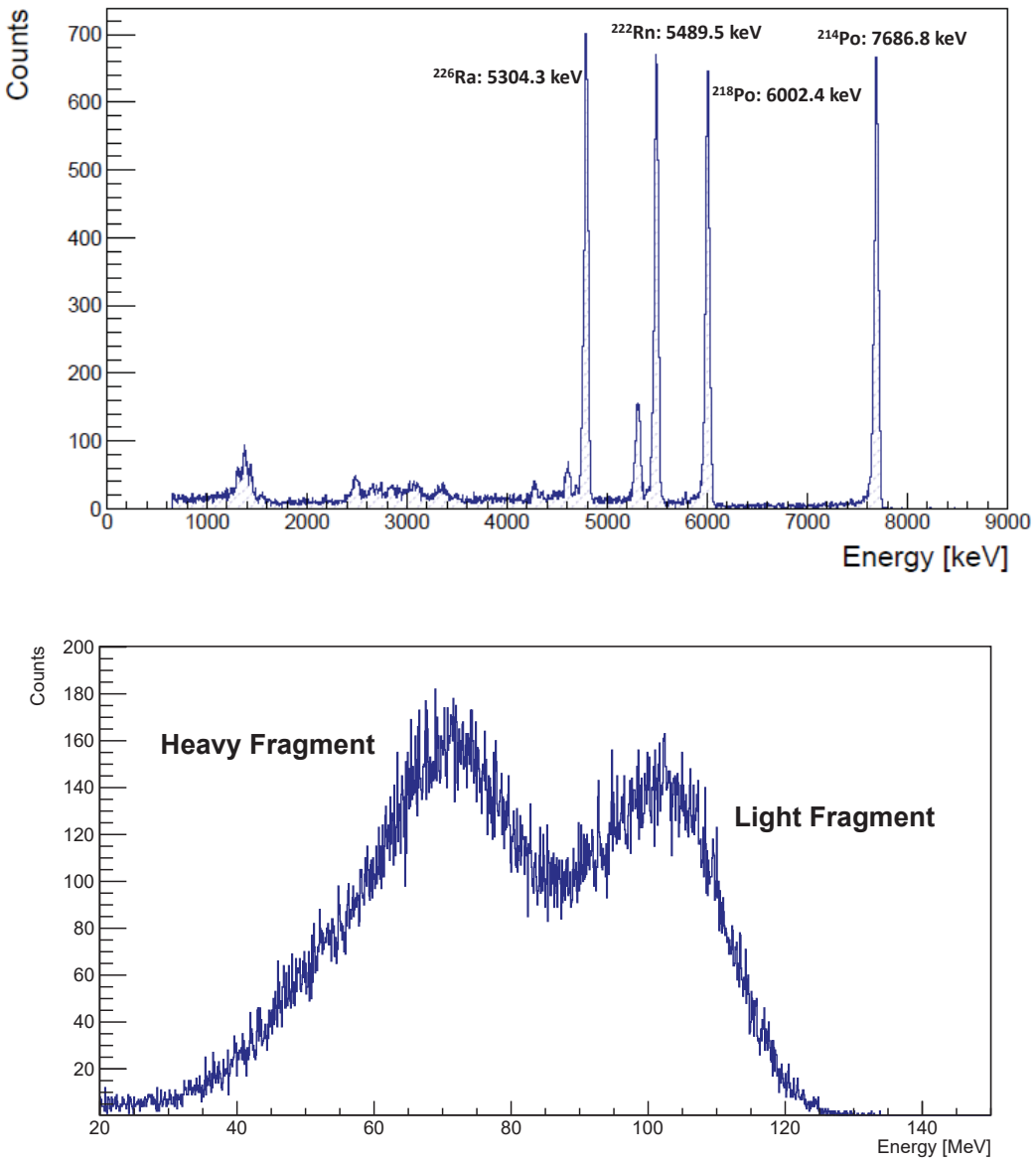

Figure 3.5: Alpha spectrum from a ^{226}Ra source in the E detector. The known alpha energies occur at 4784, 5489, 6002, and 7686 keV [Left]. Fission energy spectrum for ^{252}Cf using the fission detector. The lower energy peak corresponds to the heavier mass fragment while the lighter fragment carries more kinetic energy following a fission event [Right].

3.2 NeutronBall

Following a charged particle induced reaction, the emitted neutrons are detected using a large gadolinium doped scintillator. The neutrons emitted will scatter on the hydrogenous material in the scintillator before slowing to thermal energies. Following thermalization the neutrons are captured on either gadolinium or hydrogen. Neutron capture on Gadolinium results in an 8 MeV gamma-ray cascade primarily from the capture on ^{157}Gd, while neutron capture on hydrogen will result in a single 2.2 MeV gamma-ray. The gamma-rays will then interact with the scintillator causing florescent light that is detected through photo-multiplier tubes mounted to the array.

The geometry of the array can be broken down into two hemispherical end-caps and a central cylinder divided into four quadrants. The endcaps and inner cylinder have an outer radius of 0.75 meters; 20 cm gaps separate the endcaps from the inner cylinder, while the inner cylinder segments are separated from each other by 10 cm. The aluminum casing for the inner cylinder is 6.35 mm thick on each side except the side where the PMT's are mounted have a thickness of 19.05 mm. The aluminum casings for the endcaps have an inner chamber wall thickness of 12.7 mm and an outer chamber wall thickness of 25.4 mm.

NeutronBall Refurbishment

The NeutronBall was inherited from the Texas A&M Cyclotron Institute's NIMROD-ISIS Array. The original array contained 3.5 tons of 0.3% gadolinium doped pseudocumene [48, 42]. As the liquid aged, the gadolinium in the scintillator precipitated out of solution and the scintillator degraded, reducing optical transmission. The original PMTs were also in poor condition, when removed from the array some had cracked casing near the diodes, others had scratches on the surfaces of the lenses, and the solder on the wiring of the bases no longer formed connections.

In order for an experiment to be conducted on the array, the scintillator and the PMTs had to be replaced. New 5 inch diameter 10 stage PMTs were purchased through ADIT. Replacing the liquid scintillator was more difficult given the financial constraint. To avoid further delays and stay compliant with the host facility the a new array or interaction medium for neutrons was not considered. The cost of Ga doped liquid scintillator scales linearly with the Gd content and the volume of material. To determine the optimal configuration for the new scintillator simulations in MCNPX-PoliMi were performed.

When the neutron capture and gamma-ray energy deposition was observed over the spatial area of the detector in Figure 3.6, it was apparent that most of the interactions occurred in the central cylinder. Although the endcaps contained roughly half the volume of the scintillator, due to the solid angle between the target location and the individual components, neutrons were preferentially captured in the central cylinder (78.4 %) rather than the endcaps (21.6 %). As a result of these simulations, only the scintillator in the central cylinder was replaced.

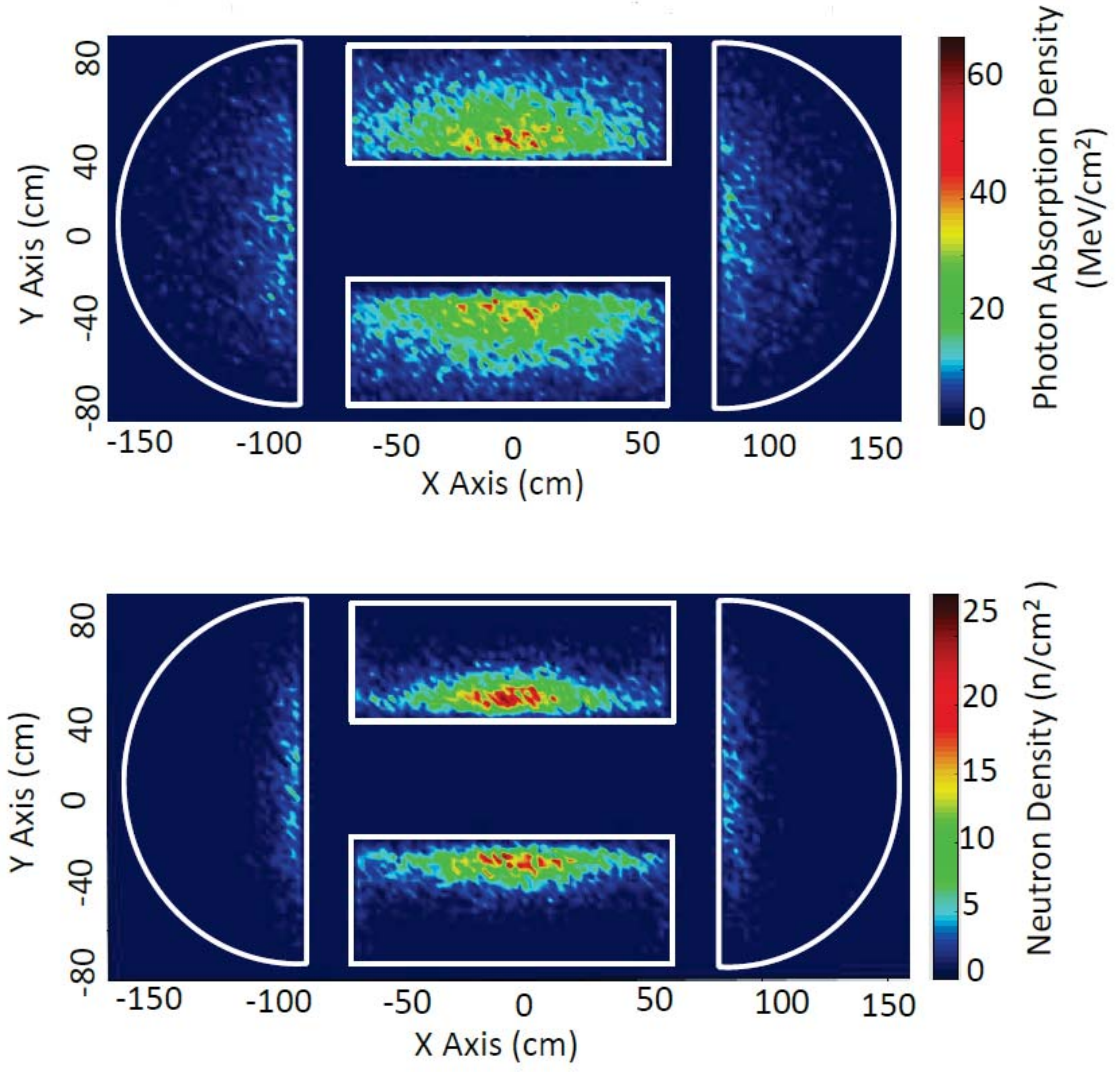

Figure 3.6: MCNPX-PoliMi simulation of 100,000 neutrons at 1 MeV in the NeutronSTARS array. [Left] Gamma-ray flash following neutron capture in the scintillator. [Right] Neutron capture locations in the scintillator.

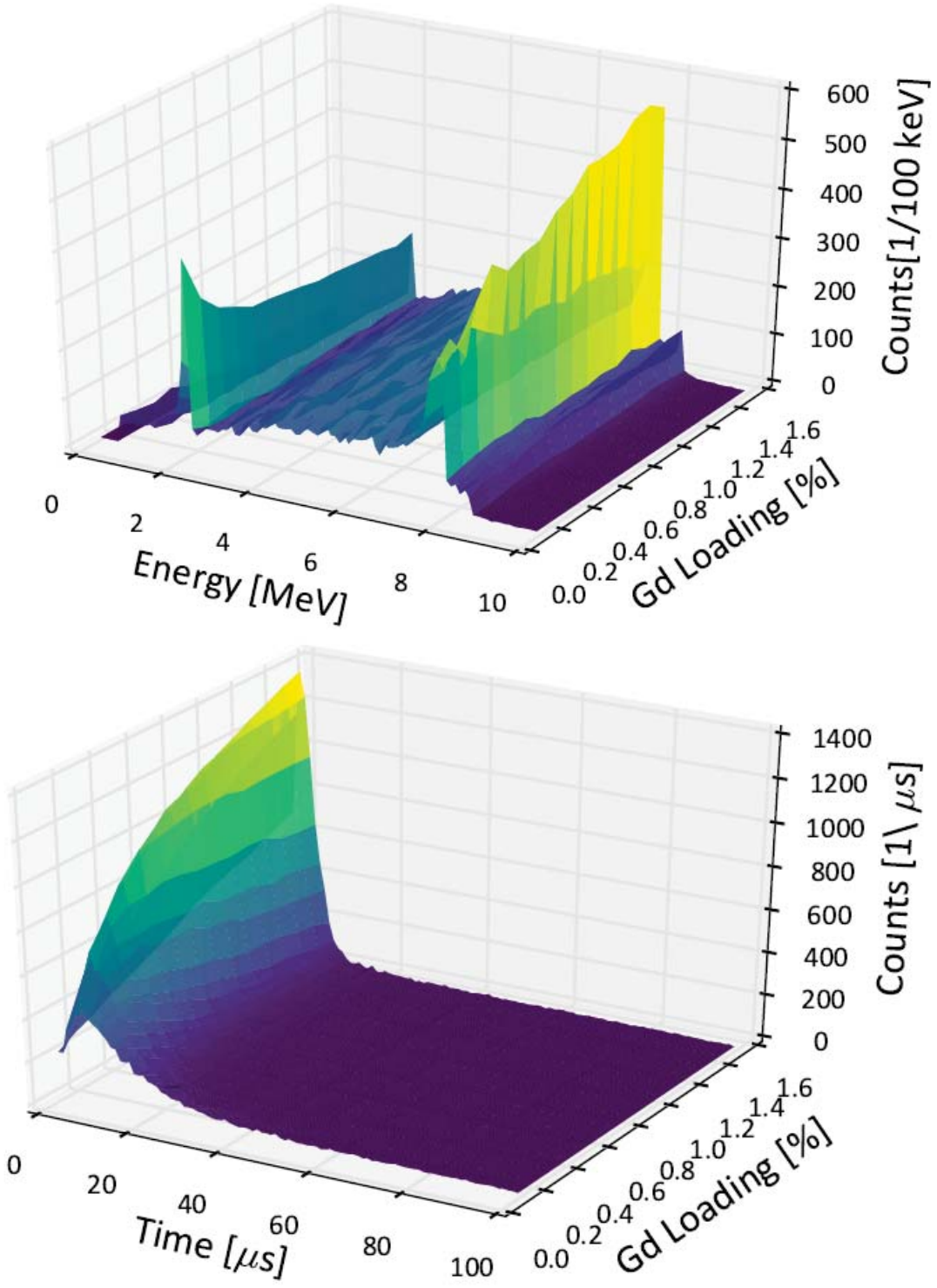

Figure 3.7: Neutron capture energy deposition and times obtained through MCNPX-PoliMi simulations. Increasing the Gd content in the liquid scintillator results in a marginally higher capture efficiency and dramtically decreasing the lifetime of the neutron in the scintillator.

Simulations were also performed with varied gadolinium loading from 0.1 to 1.6%. The resulting energy deposition and timing spectra for each were determined. From Figure 3.8, one can see that increasing the gadolinium content increases the 8 MeV deposition feature, while captures on hydrogen are reduced, as shown with a decreasing 2.2 MeV detail. The hydrogen content remains the same regardless of the gadolinium loading. Due to the higher cross section for neutron capture, increasing the Gd in the array biases the captures away from hydrogen.

Assuming an experimental 2 MeV energy threshold in the scintillator results in an efficiency change of 3% between the 0.1 and 1.6 % loading. Furthermore, higher Gd loading results in a faster neutron capture time. The neutron capture lifetime decreases nearly three fold from 16.4 to 4.17 μs over the range of Gd loading observed. Short neutron lifetimes are not ideal in counting measurements due to concerns of pile-up and differentiation between neutron capture events and the prompt interaction gamma-rays becomes experimentally challenging without pulse shape discrimination capabilities. The lower Gd doping was determined to be more effective for these measurements. The scintillator was replaced with EJ-335, a 0.25% gadolinium-loaded liquid scintillator from Eljen Technology [12].

MCNP-PoliMi Simulations

In addition to experimental measurements, simulations were used to gain a better understanding of the detection system. Monte Carlo simulations of the entire array (the target chamber and NeutronBall) were performed using MCNPX-PoliMi [36] to understand neutron interactions with NeutronBall. The array model used in the simulation is shown in Figure 3.8. MCNPX uses Monte Carlo methods to simulate nuclear interactions for neutral particles by sampling the interaction probabilities using known cross-section libraries. While constructing the simulation, ENDF libraries were used unless unavailable, then LLNL libraries were implemented. MCNPX is often used to model large systems like nuclear reactors, and impose an average treatment. For instance, neutron capture on Gadolinium would show the distribution of the gamma-ray cascade over successive iterations and only report the average capture, escape, and interaction time for both neutrons and gamma-rays. MCNPX-PoliMi expands on MCNPX and takes correlated interactions into effect. Each event is given a time, energy, position, and interaction type. Moreover, secondary particles are given the same treatment and attributed to the original event in which they were created.

Throughout the characterization of the array, specific event features were compared to the results from the simulation to validate the model. Additionally, experimental data was also incorporated into the simulation. Due to the capabilities of MCNPX-PoliMi, only the neutron and gamma-ray events were tracked, and the optical photons were not included. Additionally, the array exists in a "world" full of air, the cyclotron cave was not included in the model which primarily effects neutrons scattering out of the detector, onto concrete and back into the array.

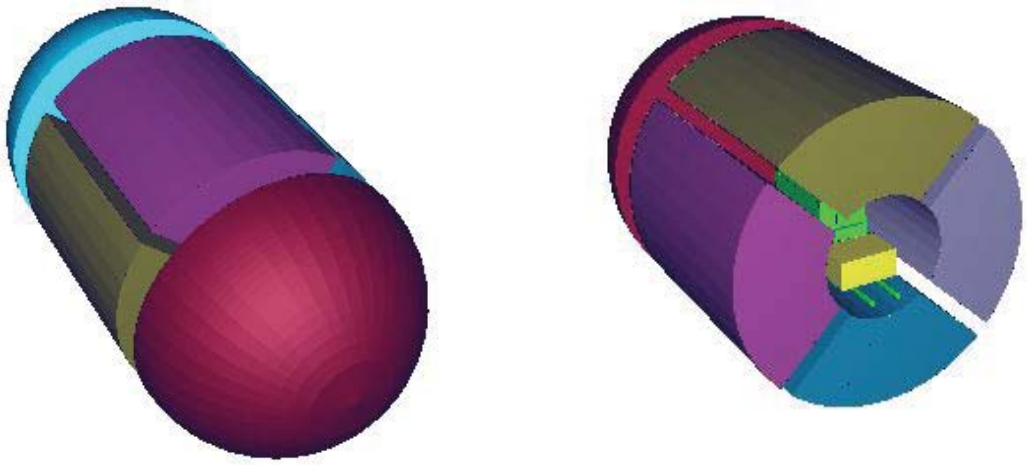

Figure 3.8: MCNPX model of the NeutronSTARS array. The aluminium casing of both the target chamber and NeutronBall, the copper pre-amplifier boxes, the scintillator, and some of the beam components are modeled.

After the detector was refurbished the configuration of the array was modeled. Figure 3.9 shows the neutron capture and gamma-ray deposition in multiple profiles of the array. Energy emitted from neutron capture on gadolinium is not contained in one gamma ray. Because the nucleus de-excites through an isotropic gamma-ray cascade, the gamma ray energy is deposited over a larger volume than the neutron captures. Evidence of neutron capture on the inactive scintillator can also be seen on the far edges facing the endcaps. Although events are not recorded in those segments they still contribute to the detector from neutrons scatters off the hemispheres or neutrons capturing in the segments and the resulting gamma ray depositing energy in the scintillator.

PMT Gain Match and Calibration

Following a neutron capture on gadolinium, only a fraction of the gamma-rays' energy are deposited in each segment. Moreover, only a fraction of the scintillation light produced is detected by each PMT. Simply placing a check source inside the array does not guarantee all the light will be seen by one PMT. Additionally, the position sensitivity of the detectors to source location may skew results. Matching the PMT bias based on observed background rates is also insufficient, the PMTs in the center of a quadrant have more shielding than the other two that surround it, additionally the geometry of the room affects the observed radiation of each quadrant. For effective event reconstruction, an absolute calibration of all

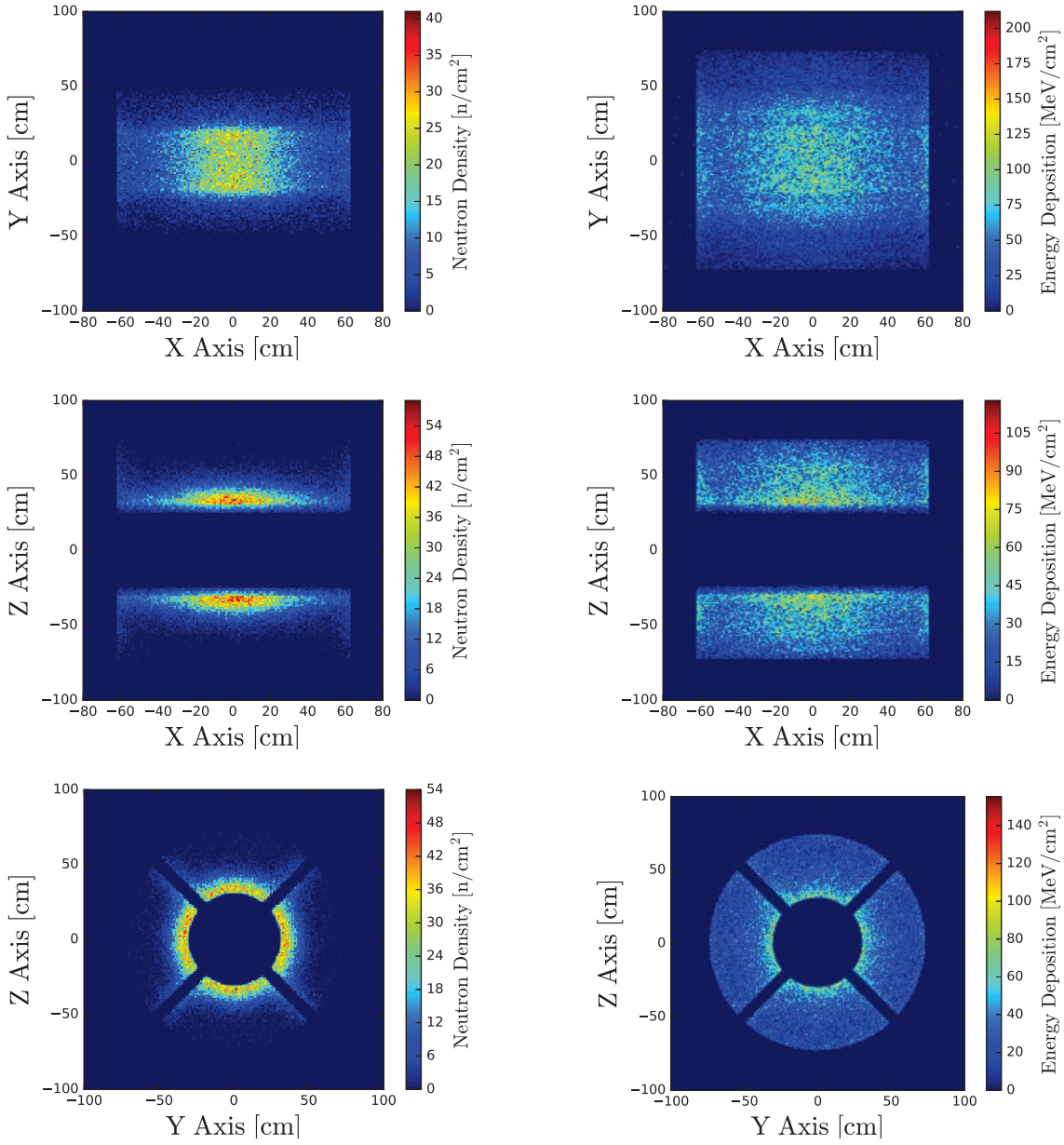

Figure 3.9: MCNP-PoliMi simulation of neutron capture events [left] and gamma-ray energy deposition [right] in NeutronBall in the XY, YZ, and XZ plane. Most neutrons capture close to the edge of the scintillator while the gamma-ray energy is deposited over a larger volume.

PMT	K	α	χ^2/df
M1	$1.40\times10^{-3} \pm 1.78\times10^{-5}$	$6.43\times10^{-1} \pm 1.23\times10^{-2}$	2.66/4
M2	$1.34\times10^{-3} \pm 1.71\times10^{-5}$	$6.63\times10^{-1} \pm 1.71\times10^{-2}$	3.36/4
M3	$1.26\times10^{-3} \pm 1.18\times10^{-5}$	$7.58\times10^{-1} \pm 1.22\times10^{-2}$	3.16/4
M4	$1.40\times10^{-3} \pm 1.80\times10^{-5}$	$6.46\times10^{-1} \pm 1.26\times10^{-2}$	4.46/4
M5	$1.24\times10^{-3} \pm 1.43\times10^{-5}$	$7.29\times10^{-1} \pm 1.51\times10^{-2}$	3.75/4
M6	$1.39\times10^{-3} \pm 1.88\times10^{-5}$	$6.29\times10^{-1} \pm 1.30\times10^{-2}$	1.77/4
M7	$1.36\times10^{-3} \pm 1.54\times10^{-5}$	$6.81\times10^{-1} \pm 1.19\times10^{-2}$	0.80/4
M8	$1.40\times10^{-3} \pm 1.66\times10^{-5}$	$6.55\times10^{-1} \pm 1.17\times10^{-2}$	1.58/4
M9	$1.29\times10^{-3} \pm 1.56\times10^{-5}$	$6.84\times10^{-1} \pm 1.41\times10^{-2}$	5.20/4
M10	$1.30\times10^{-3} \pm 1.54\times10^{-5}$	$6.85\times10^{-1} \pm 1.34\times10^{-2}$	7.00/4
M11	$1.33\times10^{-3} \pm 1.70\times10^{-5}$	$6.63\times10^{-1} \pm 1.37\times10^{-2}$	1.41/4
M12	$1.39\times10^{-3} \pm 1.64\times10^{-5}$	$6.64\times10^{-1} \pm 1.18\times10^{-2}$	0.64/4

Table 3.2: Results of the single photoelectron gain calibrations for the 12 PMTs used in the experiment. The notation M1-12 refers to the PMTs grouped on NeutronBall.

the PMTs must be performed.

Single photo-electron (SPE) counting was employed to obtain an absolute calibration point for the PMTs [1, 9]. In this procedure the PMTs are placed in a dark box with a pulsed blue LED (5 kHz)at its lowest applied voltage necessary to observe a signal above the dark current (-1.495 V) in the PMT. The SPE was then determined by analyzing the resultant spectra, as shown in 3.10. The low charge component is a result of thermal-ionic noise at the dynodes. The subsequent peaks refer to the single, double, and triple photo-electron emission. The exponential term results from back-scattered electrons at the primary diodes that do not result in full multiplication of the induced signal. The location of the SPE peak was determined at various applied voltages to determine the gain of each PMT as a function of applied voltage:

$$G(V_d) = \gamma(KV_d)^{\alpha n} \tag{3.1}$$

Here, $G(V_d)$ refers to the gain of the PMT at a given voltage (V_d), which is evenly applied to n dynodes. The gain of the preamplifier used to see the SPE signal is accounted for with the γ term, which is the same for all of the PMT's. Structural materials causing deviations from linear current application are accounted for by the α term, and K is a constant. Figure 3.10 shows the resulting gain curve for three PMTs. During the experiment the PMTs are biased as to have the same SPE gain. The tabulated results to these fits for all PMTs used in the experiment are shown in Table 3.2

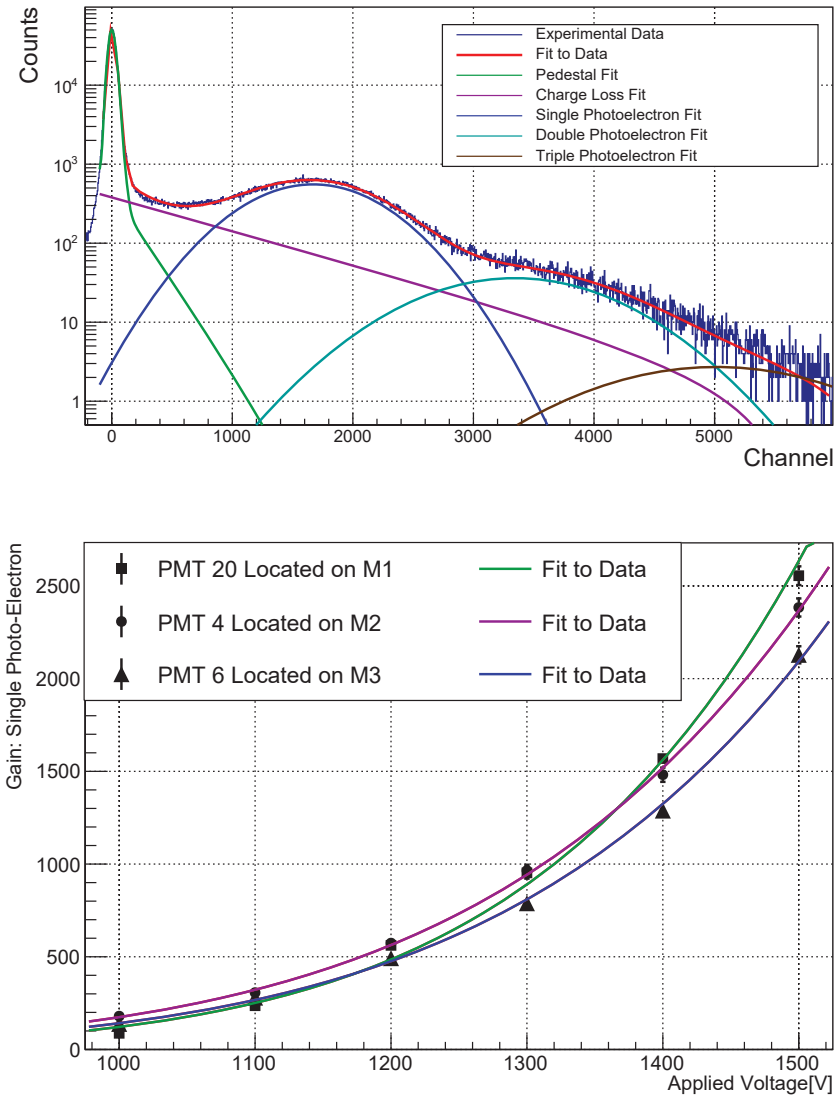

Figure 3.10: Example of single photo-electron counting for one PMT at a 1300 volt bias [Top]. The first pedestal peak represents the electronic noise and dark current. The subsequent peaks feature the single, double, and triple photo-electron peaks. The exponential charge loss term arises from partial charge collection due to loss among the dynodes.SPE gain curves for the PMTs in one quadrant. The M1, M2, and M3 labels refer to the location of the PMT on NeutronBall [Bottom].

Quadrant	m [keV/SPE]	b [keV]
Top	0.734276	-66.9649
Wall	0.517733	41.452
Room	0.517733	41.452
Bottom	0.775924	-122.0
Total	0.8082	135.68
Source	Energy[keV]	FWHM [keV]
^{137}Cs	662	98.01
^{60}Co	1253	358.8
^{228}Th	2614	895.9
^{12}C(α, α')	4438	1244.3

Table 3.3: Results of the NeutronBall calibration for all the quadrants and the total array. The energy response of the calibration sources are also displayed. The energy response for ^{60}Co, ^{228}Th, and ^{12}C(α, α') are misleading due to the two gamma-ray emission in ^{60}Co and the coupled single and double escape peaks in both ^{228}Th and ^{12}C(α, α').

Gamma-Ray Response

The NeutronBall detects neutrons indirectly by detecting the gamma-ray signature indicative of neutron capture. As a result the NeutronBall's response to gamma-ray sources was used to calibrate the energy deposited following neutron capture. Gamma rays from^{137}Cs, ^{60}Co and ^{228}Th at 662, 1253 and 2614 keV respectively; along with inelastic scattering of alpha particles to the first excited state of ^{12}C at 4438 keV were used to calibrate the detector, when the PMTs were at the same effective gain. For the gamma-ray check sources, the source was placed at the center of each segment and counted for 20 minutes. After a background run was taken for the same amount of time, the run was subtracted from the source signals. Each individual segment was calibrated separately to determine the energy response from gamma-rays. It is possible for gamma-rays to scatter from one segment and deposit the rest of its energy into an adjacent detector. The sources were again observed using the entire array instead of individual segments, and another small calibration was applied to the entire array. The results of the NeutronBall calibration are found in Table 3.3. The energy response in each segment was found to be linear.

The gamma-ray energy deposition was also used to inform the NeutronBall simulation. As noted earlier in the text, MCNP-PoliMi cannot perform optical transport. To determine the energy broadening due to optical transmission, emission, and leakage properties, the full width half-maximum (FWHM) of the gamma-ray energies was fit to the following:

$$\text{FWHM} = a + b\sqrt{E + cE^2} \tag{3.2}$$

where a represents the locus dependent light transmission, b statistical behavior, and c broadening due to noise; as a function of gamma-ray energy E in MeV. Using standard

notation the energy resolution of the array was determined to be $(29.7\pm2.1)\%/\sqrt{E[MeV]}$. A comparison of the unbroadened and broadened simulations for the gamma sources with the experimental data can be found in Figure 3.11.

Neutron Response

After the gamma-ray response in the NeutronBall was calibrated, the single neutron efficiency for the array was determined using an ^{241}AmBe source in the target chamber. When the alpha emitted from ^{241}Am fuses with ^{9}Be the ^{13*}C* compound nucleus is formed. When that nucleus de-excites it releases a neutron, and if ^{12}C is left in the first excited state it will release a 4.4 MeV gamma-ray. As a result, every time a 4.4 MeV gamma ray is emitted, a correlated neutron was also emitted.

In order to tag on the 4.4 MeV gamma ray, a 3 inch (7.62 cm) diameter 3 inch thick (7.62 cm) NaI(Tl) detector was added to the center of the array. Due to the size of the detector and neutron energy spectrum for AmBe neutrons, it is assumed that the NaI(Tl) detector did not affect the transmission of neutrons. To maximize the neutron tagging events, the 4.4 MeV peak, single escape peak, and double escape peak in the NaI(Tl) detector were used as a trigger [45]. When a 4.4 MeV gamma-ray was detected in the NaI(Tl) detector, prompt and delayed gates of 40 μsec width, beginning at 2 us and -42 μsec relative to the trigger, were used to determine coincident neutron events as well as uncorrelated background events in NeutronBall. With a gamma-ray energy threshold of >2 MeV, the neutron efficiency for the detector was found to be $(48.12 \pm .51)\%$. The neutron detection efficiency quoted is conservative and can be increased substantially by lowering the energy threshold in the scintillator and increasing the width of the timing gate.

The energy response was compared to the MCNPX-PoliMi simulation with Gaussian broadening and can be seen in Figure 3.12. Discrepancies in the simulation and experimental data can be seen at low energy ranges, which are attributed to phosphorescence or after glow in the scintillator.

The timing spectrum for NeutronBall events with energies >2 MeV following a NaI(Tl) event trigger was plotted with the timing spectrum from the simulation as well as a fit to the expected timing distribution $h(t)$ for a gadolinium doped scintillator [42, 35]:

$$h(t) \propto \frac{\lambda^2\beta}{(\lambda-\beta)^2}[e^{-\lambda t}[(\lambda-\beta)t-1]+e^{-\beta t}] \tag{3.3}$$

Here, λ refers to the slowing down parameter, and β is a parameter based on the properties of the scintillator and gives insight to the gadolinium content of the scintillator. The results of the fit to the data is shown in Table 3.4. Fitting the experimental data yielded a mean capture time of (12.98± 0.33) μsec and a gadolinium content of (0.268 ± 0.009)% for a quoted 0.25% gadolinium doping. Discrepancies in the fit and data arise from the geometry of the detector. The probability of capture used in the fit function assumes a continuous volume, whereas the NeutronBall is segmented with air gaps between each quadrant.

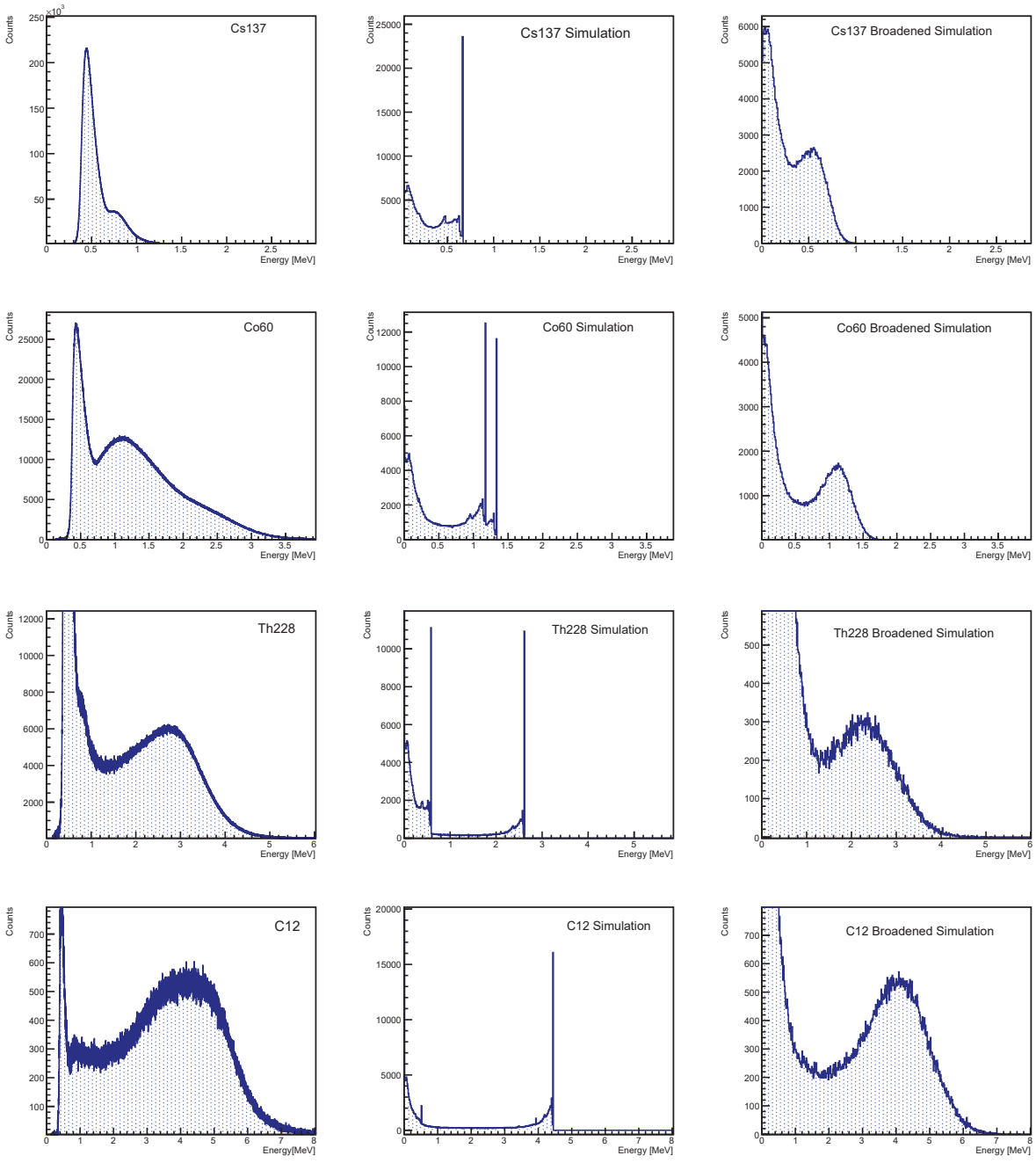

Figure 3.11: Comparison of the experimental response to ^{137}Cs, ^{60}Co, ^{228}Th, and ^{12}Ca in NeutronBall to the simulated response with broadened and discrete energy resolution. There is gamma summing in the actual spectrum for the ^{60}Co in the real spectrum but not the simulation.

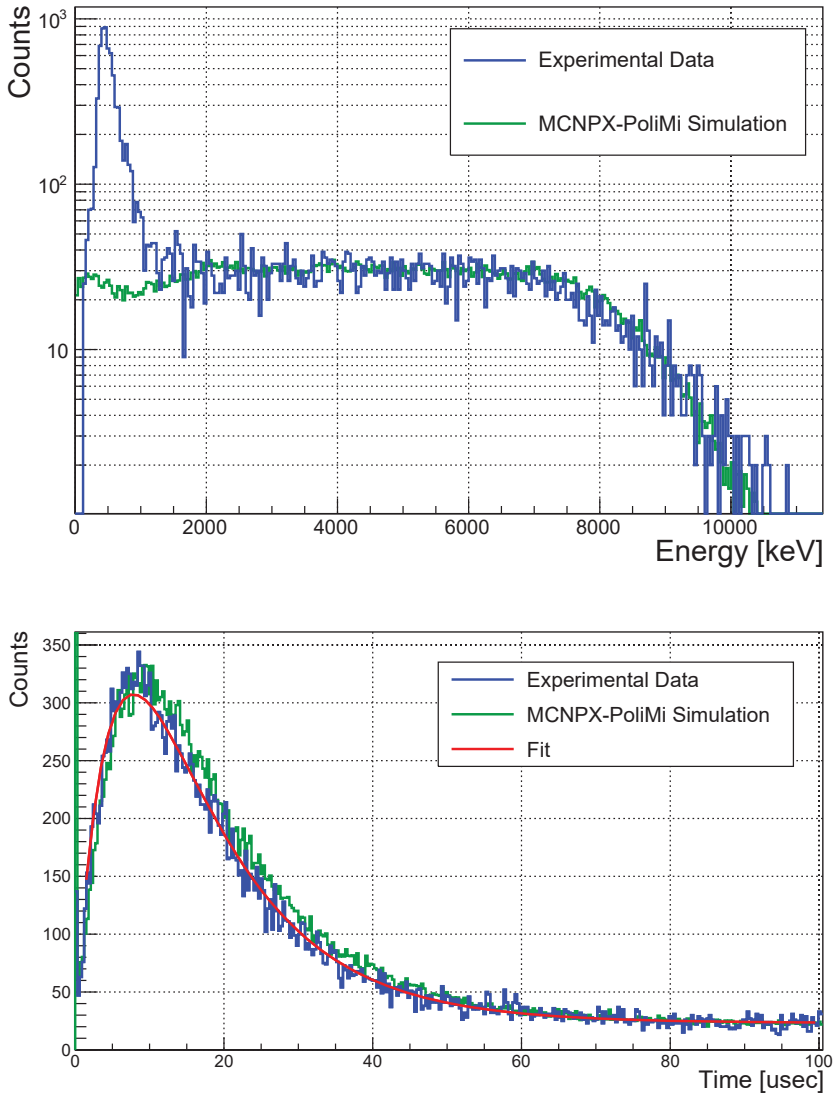

Figure 3.12: NeutronBall response to AmBe neutron source. The timing spectrum for the experiment was compared to the timing spectra from the MCNPX-PoliMi simulation, and was fit to the expected timing curve for gadolinium doped scintillators[Top]. The fit resulted in a χ^2 of 1.05/df. The energy response from NeutronSTARS was also compared to the MCNP simulation [bottom].

Parameter	Description	Value
β	Gd Constant	0.0722 ± 0.004
λ	Moderation Parameter	0.154 ± 0.012 μsec^{-1}
t	Mean Capture Time	12.98 ±0.33 μsec
C_{gd}	Gadolinium Conc.	0.268 ± 0.009%
χ^2/df	Reduced χ^2	353/326

Table 3.4: Results from fitting the experimental data to Equation 3.3

3.3 Neutron Efficiency

The neutron detection efficiency was determined using a combination of single neutrons from an AmBe source, multiple neutron emission from a ^{252}Cf source, and MCNP-PoliMi. All measurements and simulations took place within the target chamber. When using an AmBe source the efficiency of the array was found to be $(48.12 \pm 0.51)\%$ for neutrons tagged with a 4.4 MeV gamma-ray. Using the fission detector to tag on fission fragments, the efficiency of detecting neutrons from a ^{252}Cf source was determined to be $(50.81 \pm 0.15)\%$ using the same timing gates and energy cuts. As shown in Figure 3.13, the differences in the neutron efficiency from the two sources arise from the neutron energy spectra.

The average neutron energy from a tagged AmBe source is roughly 5 MeV, where the ^{252}Cf source follows a Maxwell-Boltzmann distribution with an average neutron energy of about 2 MeV [40, 41]. Due to room return the simulation shows a lower efficiency across all energies than those that are measured. As a check to the neutron energy effect, the ratio of the AmBe and ^{252}Cf efficiencies was used. When coupling the efficiency with that of the AmBe and ^{252}Cf , the ratio of the two efficiencies was $(93.76 \pm 0.66\%)$; consistent with the ratio of measured efficiencies of $(94.34 \pm 0.97\%)$. Because the neutron energy spectrum for following fission follows a Maxwell-Boltzmann distribution with a similar average neutron energy as ^{252}Cf, no correction to the efficiency from ^{252}Cf is needed when assessing neutron multiplicities from fission. For neutrons emitted from surrogate (n,2n) reactions, the efficiency is corrected using the expected neutron energy spectrum for (n,2n) obtained through NADS (Nuclear and Atomic Data Systems) as shown in Figure 3.14 [34]. A ratio of the simulated neutron captures between the (n,2n) and ^{252}Cf neutrons will be multiplied by the measured ^{252}Cf efficiency to deduce the neutron detection probability for (n,2n) reactions. The generalized efficiency for (n,xn) reactions is given by:

$$\varepsilon(E_{(n,xn)m}) = \frac{\varepsilon(E_{(n,xn),s})}{\varepsilon(E_{Cf-252,s})}\varepsilon(E_{Cf-252,m}) \tag{3.4}$$

Where ε is the efficiency and the subscripts s and m refer to the simulation and measurement values respectively.

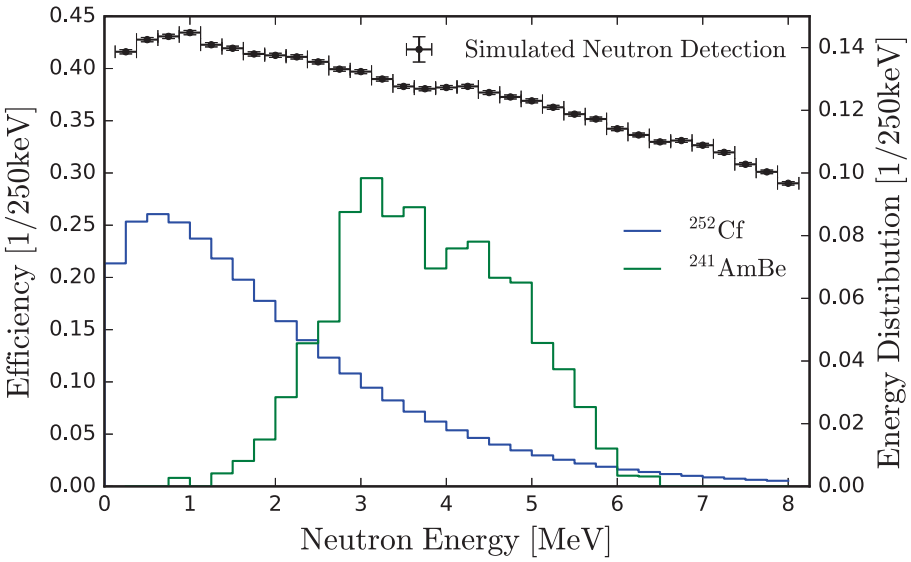

Figure 3.13: The simulated neutron efficiency of the NeutronBall using a 2 MeV energy lower energy cut and 2 to 42 μs prompt and -42 to -2 μs background window. Additionally, the ^{252}Cf and AmBe neutron energy spectra are plotted to explain the source of disagreement between the two efficiencies; higher energy neutrons are less likely to be detected in the array.

3.4 Multiplicity Reconstruction

Whether measuring neutrons from fission or determining (n,xn) cross-sections, the function of the array is to determine correlated neutron multiplicities. As a test to reconstruct the neutron efficiency and determine neutron multiplicities a, ^{252}Cf source was used. After tagging on fission fragments from the fission detector, two timing windows of 40 μsec length were set at 2 μsec and -42 μsec for signal and background neutrons, respectively. Two raw multiplicities were extracted from the measurement: prompt multiplicities with signal and background neutrons, and delayed multiplicities with background neutrons. The background can be subtracted using a fit to the following linear combination:

$$D[i]B[i,j] = P[i] \tag{3.5}$$

Here P represents a one dimensional vector and i corresponds to the detected multiplicity for each integer neutron without background correction. The quantity D represents the background corrected neutrons detected by the array. Uncorrelated random backgrounds tend to follow a Poisson distribution. During in beam experiments the contribution of fusion-fission neutrons yields background distributions with large deviations from a Poisson distribution. As a result, the determined background distribution from ^{252}Cf is used instead of a Poisson shape. The matrix $B[i,j]$ is an upper diagonal matrix composed of the background

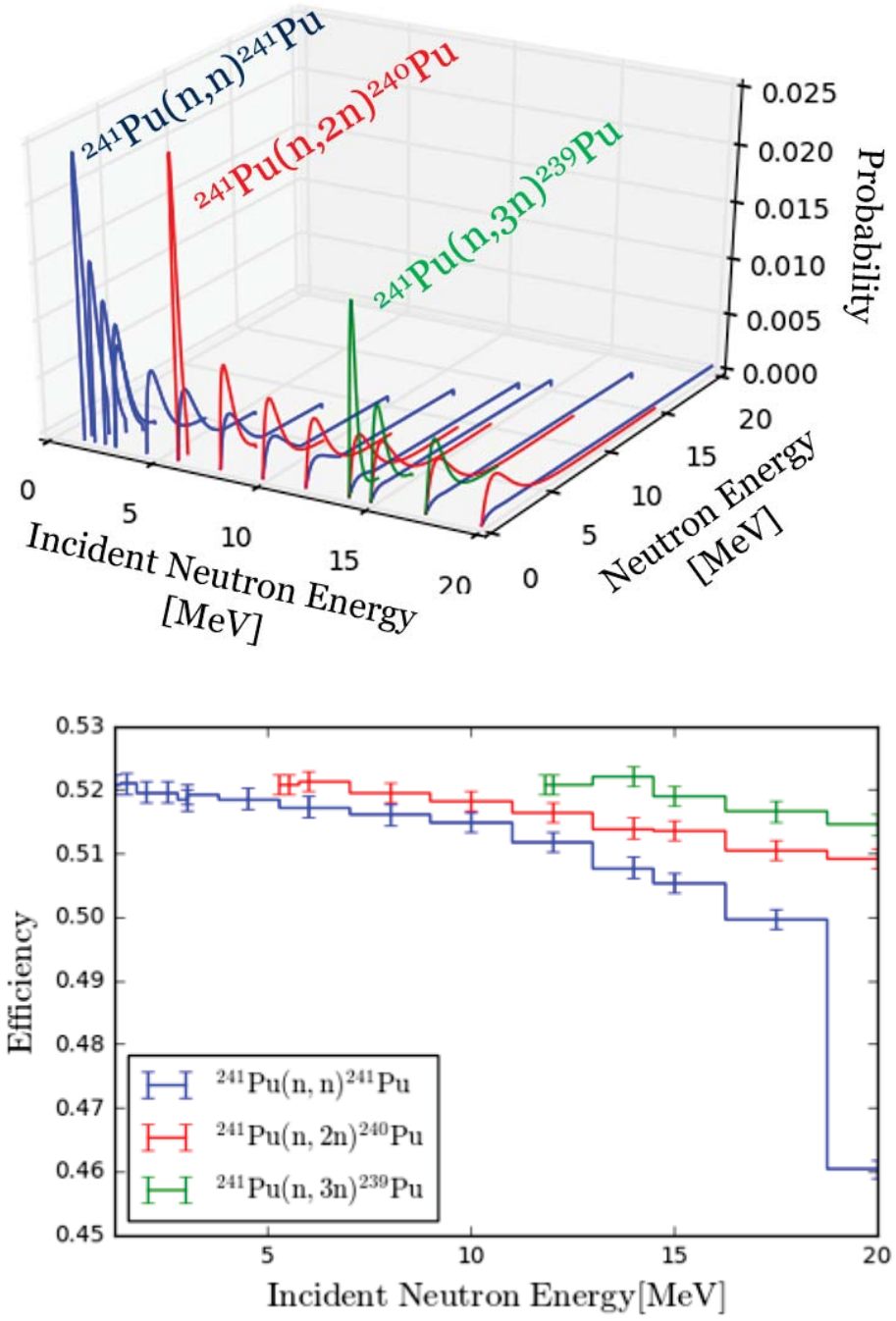

Figure 3.14: Emitted neutron energy distributions for (n,xn) reactions obtained from NADS [Left]. The neutron energy was combined with the detector simulation to determine the efficiency of the array for specific (n,xn) reactions as a function of energy [Right].

multiplicity $b[i]$ for n neutrons:

$$B[i,j] = \begin{cases} B[j-i] & \text{if } j >= i \\ 0, & \text{otherwise} \end{cases} \tag{3.6}$$

Instead of inverting the background matrix, the parameters of $D[i]$ are determined by floating the individual components until a reasonable fit to the detected neutrons on-top of the characterized background matches the prompt neutrons detected. If i neutrons are detected there is a finite probability that j neutrons were emitted. Because neutron detection follows a binomial distribution, the probability matrix containing the probability that i neutrons were detected for a real multiplicity of j for a given efficiency ϵ is as follows:

$$Bi[i,j] = \begin{bmatrix} j \\ i \end{bmatrix} \varepsilon^i (1-\varepsilon)^{j-i} \tag{3.7}$$

Here Bi represents the binomial distibution matrix used to apply the efficiency correction. High efficiency, 90% arrays can use the inverse of this matrix to determine the efficiency corrected neutron multiplicity. This array is about 50% efficient, so applying a de-convolution to the background corrected matrix yields large uncertainties in the result. Instead, a least squares fit is applied with a skewed Gaussian distribution, a well characterized neutron multiplicity shape, multiplied by the determined binomial matrix to the detected multiplicity distribution. An example of this can be found in Figure 3.15. When the resulting fitted skewed Gaussian distribution was compared to the existing literature, the multiplicity agreed to the known values within their uncertainties. Additionally, an average multiplicity of (3.78± 0.03) neutrons was consistent to the literature value of (3.76± 0.01) neutrons [39].

Many multiplicity analyses correct for the dead-time of the detector when reconstructing fission neutrons. In this system each individual PMT has a 500 nsec dead-time. Due to the segmentation of the detector and efficiency of the array, dead-time has a negligible effect on the detector. This was further verified by confirming the efficiencies from using a single neutron source, AmBe, and a multiple neutron source, ^{252}Cf as previously discussed.

3.5 Electronics

The data-acquisition system allows for charged-particle and neutron events to be recorded in close time coincidence, with the flexibility to trigger on fission fragments. Most of the electronics are housed in a VME crate. Additionally, all 20 photomultiplier tubes (PMTs), the ΔE, E, and fission detector are biased in MPOD crates using multiple ISEG modules [33]. When charged particles deposit energy in the ΔE, E, and/or fission detector,the resulting ionization drifts through the detector. These signals are amplified using amplifiers housed in copper crates adjacent to the STARS chamber to minimize noise. The signals are transported to an electronics rack via 60 foot (18.3 meters) cables and are further amplified through CAEN N568B spectroscopy amplifier before being sent to a CAEN programmable

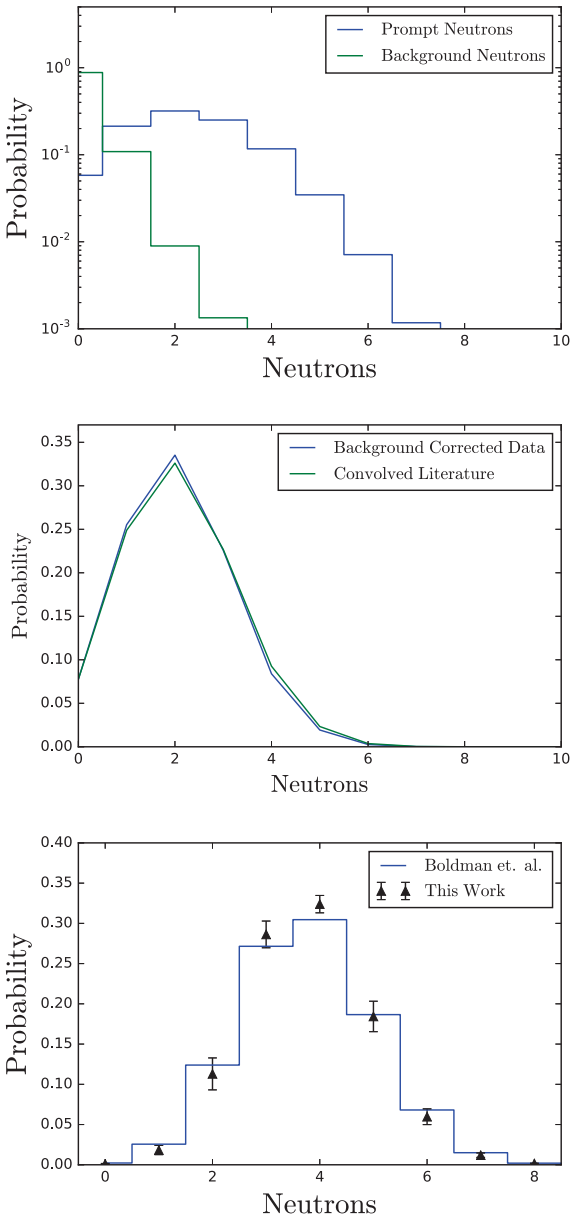

Figure 3.15: ^{252}Cf multiplicity construction. [Top] Detected neutron multiplicities in prompt and delayed times. [Middle] Background corrected multiplicity for detected neutrons plotted against the known ^{252}Cf multiplicity multiplied by the binomial probability matrix. [Bottom] Determined ^{252}Cf multiplicity using data obtained with NeutronSTARS compared to the literature value[5].

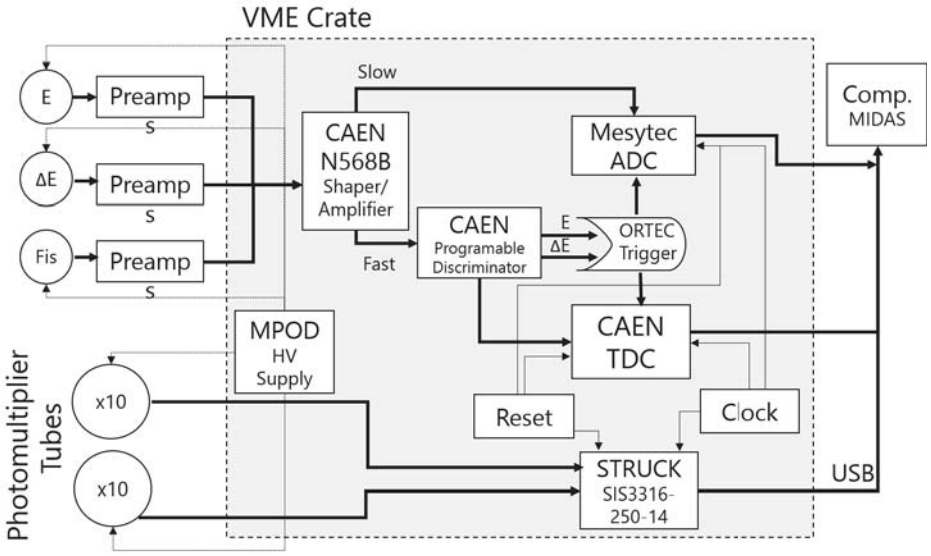

Figure 3.16: Diagram of the NeutronSTARS electronics. The PMTs are directly read into STRUCK SIS3316-250-14 modules with a clock syncing the timing signals from the silicon detectors and the PMTs. The silicon telescope and fission detector are pre-amplified and then shaped and amplified through CAEN N568B modules where the slow signal is sent to a Mesytec ADC and the fast output to a CAEN TDC before being read out through MIDAS software on a computer. All electronics are powered through an MPOD high voltage supply.

discriminator [6]. The ΔE-E coincidence trigger uses logic outputs taken from the amplifier fast output. The fast output is also sent to the CAEN TDC, while the signals pertaining to energy deposition are sent to the Mesytec ADCs [30].

The data from the Mesytec ADCs and CAEN TDC are recorded on a central computer for data storage and online analysis. The STARS electronics are similar to those used for the Hyperion Array [20]. When PMTs read out fluorescence created in the scintillator, their signals are sent directly to Struck SIS3316-250-14 module [44]. The resulting energy signal, and time signatures are recorded in a set of accumulator time windows for online and offline processing. Real time analysis of the data is performed using MIDAS (Maximum Integrated Data Acquisition System) and in-house software previously used with the STARLiTeR array [7, 26, 32]. A graphical representation of the electronics can be found in Figure 3.16.

Chapter 4

Experimental Calibration

The experiment to measure the surrogate reactions for ^{241}Pu took place over a three week span. In total roughly six terabytes of data was obtained, four of which was pertinent to the ^{241}Pu (n,fxn) and (n,xn) analysis. Before the data from the experiment can be sorted to account for kinematics, particle type, and inter-event correlations, the conditions specific to the experiment should be quantified. While the previous chapter focused on the general NeutronSTARS setup, the following describes the features specific to the experiment.

4.1 Targets

Throughout the experiment, multiple targets were placed in path of the beam. These targets either provided the signal of interest for the intended measurement, quantified backgrounds, or were used for in-beam calibrations and source placement. A summary of the targets run during the experiment are shown in Table 4.1. Note, ^{240}Pu was run for a separate surrogate measurement for ^{239}Pu. The location of the beam spot and energy is important when determining kinematic corrections specifically energy losses through dead layers and recoils. Because this is an under-defined problem, ^{208}Pb was run to determine the beam energy. A detailed description of how the isotope is used to determine information about the beam is found in Section 4.2. The phosphorus targets were run to ensure the beam spot was central on the target location during the experiment.

Events of interest for this experiment are inelastic scattering events on ^{242}Pu. The ^{242}Pu target consisted of 140 μg of plutonium oxide electroplated on a 100 μg carbon backing. Given the composition of the signal target, scattering events from the oxygen and carbon concentration will pollute the signal of interest. An alpha beam of 55 MeV incident on carbon, oxygen, and plutonium was simulated using TALYS [24]. The angular and energy distributions of emitted or scattered alpha particles are plotted. From the simulated alpha scattering events shown in Figure 4.1, the reaction cross sections can be observed. The events near the alpha energy show elastic scattering events off the ground state and discrete excitation from inelastic scattering from the low lying states in plutonium. The broad feature

Target Wheel Location	Target	Thickness [μg/cm^2]	Experimental Purpose
1	^{208}Pb	200	Beam Energy Calibration
2	^{240}Pu	140	Reaction of Interest
3	3/4" Blank Frame	0	Background Quantification
4	Mylar	2.5	Quantify the Oxygen Background
5	1/4" Phosphorus	200	Beam Energy Calibration
6	^{242}Pu	140	Reaction of Interest
7	Solid Phosphorus	3×10^3	Beam Tuning
8	Natural Carbon	100	Quantify the Carbon Background

Table 4.1: Targets run during the experimental campaign. All targets are either used to observe the reaction of interest, quantify backgrounds, or help with the beam tune and calibration.

Isotope	^{238}Pu	^{239}Pu	^{240}Pu	^{241}Pu	^{242}Pu	^{241}Am
Activity (μCi)	0.29	0.0018	0.028	3.44	2.25	0.25
Mass (μg)	0.169	0.290	1.230	0.332	5.71×10^3	0.729

Table 4.2: Isotopic concentration of the ^{242}Pu sample used electroplated on the target used in this work. Small concentrations of ^{238,239,240,241}Pu and ^{241}Am are present.

reflects compound reactions that result in events of interest such as neutron emission and fission. The lower energy isotropic band is indicative of alpha evaporation. Under 20 MeV, enough energy is stored in the compound nucleus that alpha evaporation is possible. For the ^{16}O and ^{12}C the discrete peaks from the ground and first excited states can be seen. The energy of the discrete alpha scattering is less than the beam energy due to the recoil energy from lighter targets. The elastic peaks from carbon and oxygen are the most prominent feature from the three targets in the energy range of interest for the experiment.

The carbon and oxygen content are known backgrounds that exist throughout the experiment. To ensure proper background subtraction to isolate the plutonium content, natural carbon and Mylar targets were also run. The carbon target is identical to the carbon backing that the plutonium target is electroplated onto, while the Mylar target is a polyester film with a chemical formula of $C_{10}H_8O_4$. Natural carbon and oxygen concentrations are assumed in all targets, and the plutonium target was about 99.9% pure. A summary of the plutonium contaminants are shown in Table 4.2.

4.2 Beam Conditions

During the experiment a 55 MeV alpha particle beam with a current of 60 ppA was requested. From online diagnostics and primary observations, it became apparent the beam conditions

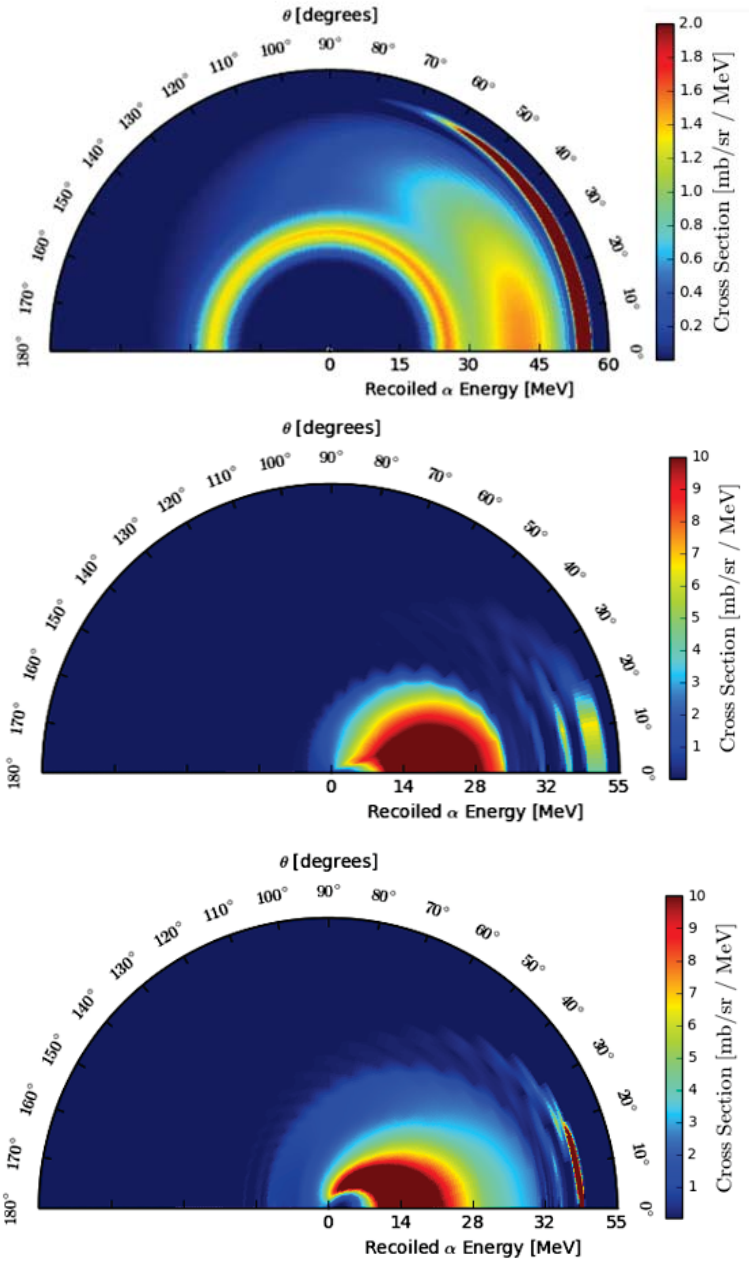

Figure 4.1: TALYS simulation of 55 MeV alpha particle incident on ^{242}Pu [Top], ^{12}C [Middle], and ^{16}O [Bottom]. The angular and energy distributions of emitted alpha particles following interaction from either scattering or evaporation are shown. Note the scales on the cross-sections are not consistent between the three isotopes.

were not consistent throughout the experiment. Although the energy of the beam remained consistent, the beam spot and intensity were variable throughout the runs. The beam conditions are imperative to properly assessing the kinematic corrections for the analysis. The energy of the beam along with a variable beam spot as a function of time was determined for the experiment.

Beam Spot

Ray-tracing was employed to determine the variable beam position. Measurements were previously performed to determine the distance from the target wheel to the ΔE detector (1.8808 cm) and the distance between the ΔE and E detector (0.5241 cm). With known Z_b coordinates, the location of the beam is assumed to be at ($X_b = 0$, $Y_b = 0$, $Z_b = 0$), while the coordinates of the ΔE detector are varied based on the known ring and sector hits:

$$X_{\Delta E} = (1.5 + 0.1R_{\Delta E}) \times \cos\left(\frac{\pi(4S_{\Delta E} + 1)}{16}\right) + B_x \tag{4.1}$$

$$Y_{\Delta E} = (1.5 + 0.1R_{\Delta E}) \times \sin\left(\frac{\pi(4S_{\Delta E} + 1)}{16}\right) + B_y \tag{4.2}$$

The subscripts ΔE refer to the thin detector, and is interchangeable with the E detector when determining the location of interaction for the thick detector. The S and R designations are given based on the ring and sector which had the largest charge deposition for a given interaction, while B refers to the floating parameters for the beam location. Note the radius of the silicon detectors are 1.5 cm and the total radius of the rings increments by 0.1 cm which each additional ring. The unit vector, $\hat{U}$, for the particle path can then be determined:

$$\hat{U} = \frac{(X_{\Delta E} - X_E)i + (Y_{\Delta E} - Y_E)j}{\sqrt{(X_{\Delta E} - X_E)^2 + (Y_{\Delta E} - Y_E)^2}} \tag{4.3}$$

A scalar, T, is then defined as the location from the beam location ($X_b = 0$, $Y_b = 0$, $Z_b = 0$) to the location in which the ray trace would intersect with the target.

$$(T_x, T_Y) = \left(\frac{X_{\Delta E} - (X_e - X_{\Delta E})Z_B}{Z_E - Z_{\Delta E}}, \frac{Y_{\Delta E} - (Y_e - Y_{\Delta E})Z_B}{Z_E - Z_{\Delta E}}\right) \tag{4.4}$$

The B_x and B_y coordinates were varied along the area of the target until the dot product of T and $\hat{U}$ were minimized. An example of the minimization procedure can be seen in Figure 4.2. From online observations, it became apparent that the beam was drifting throughout the experiment. For each one hour run, the beam location was determined and applied to the relevant kinematic corrections.

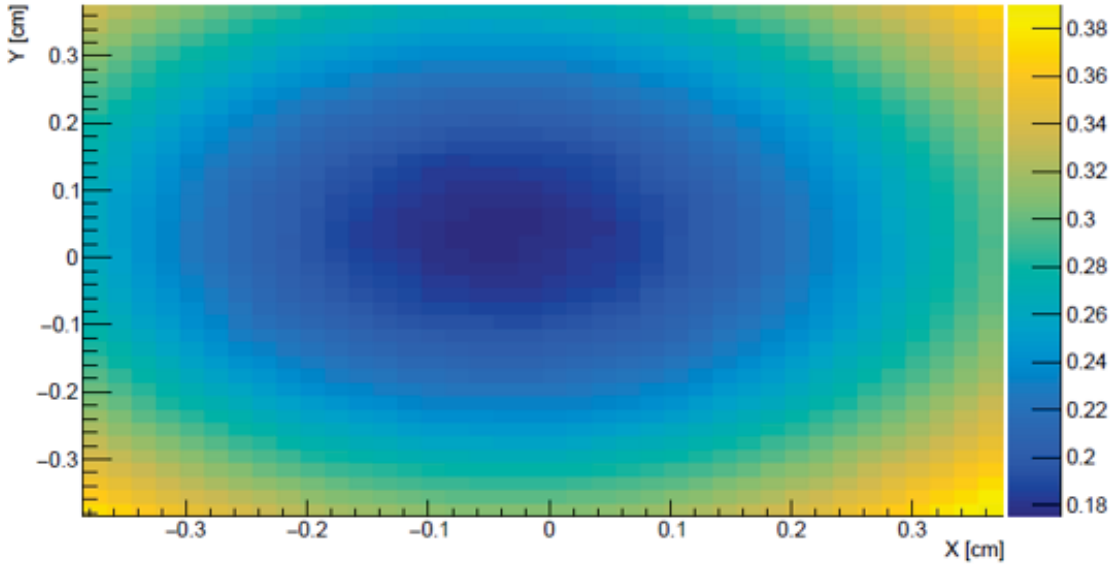

Figure 4.2: Minimization of the projection of the beam spot location to the ray traced location of the particle origin.

Beam Energy

Once the variable beam location was determined, the energy of the incident alpha particles was determined by observing the ^{208}Pb calibration. In the target chamber, there are non-detector like materials the alpha particle must transverse before deposing some energy in the ΔE and stopping in the E detector. The angle in which the alpha particle is scattered effects the energy loss in the so called "dead-layers". Energy Loss and Scattering Tool (ELAST) was used to correct for energy deposition in the dead layers. The program takes the following inputs: incident beam, target composition, angular range, projectile energy range, and thickness of the dead layer; then ELAST returns the following outputs: emitted angle, incoming projectile energy, outgoing projectile energy, and energy loss.

The beam location was previously determined to the incident angle , θ, then follows:

$$\theta = \arctan\left(\frac{\sqrt{(X_{\Delta E} - X_B)^2 + (Y_{\Delta E} - Y_B)^2}}{Z_{\Delta E} - Z_B}\right) \tag{4.5}$$

Experimental observables of interest are the energy losses in the ΔE and E while the energy loss in the target, aluminum δ shield, gold rings on the ΔE silicon detector, and the aluminum sectors on the ΔE and E detectors. Working backwards the energy right before the energy loss from the E detector is known by the measured energy of the E detector. A bi-linear interpolation of the emitted energy and the angle determined the amount of energy lost in the aluminum layers of both the sectors for the silicon detectors. Note the silicon detectors are facing each other from the aluminum side and the orientation of the E detector's sectors

has been switched in the software to reflect that of the ΔE detector. Once the energy loss through the aluminum sectors was determined, the energy was added to the recorded energies of the E and ΔE to find the energy following loss in the gold rings. These inputs allowed for the energy loss through the gold rings by using ELAST. The same procedure was done to determine the energy loss through the δ shield and lead target.

Using the energy loss and silicon detector energy deposition, the energy of the emitted alpha particle can be deduced. The last energy correction to implement is then the energy loss due to the recoil of the target nucleus. Referring to Equation 2.5 the outgoing particle energy $E_{b,out}$ is then:

$$E_{b,out} = E_{\Delta E} + E_E + E_{\delta shield} + E_{Au} + E_{Al} \tag{4.6}$$

Here, the subscripts represent the energy losses of the various dead layers and silicon detectors. Applying energy and momentum conservation laws, the energy loss due to recoil is then:

$$E_{rec} = \frac{E_a(m_Y - m_X) - E_{b,out}(m_3 + m_Y) + m_Y Q + 2\sqrt{E_a E_{b,out} m_X^2}\cos\theta}{m_Y} \tag{4.7}$$

Note the Q value for these reactions are zero, and the mass increase due to excitation of the target is considered negligible throughout the rest of the experiment. The energy of the beam was then determined by varying the assumed energy over a 10 MeV range in 10 keV increments. The energy of the ΔE and E detector was also determined for the elastic peak for each pixel location. The varied energy that yielded the minima among the pixels for the energy difference between the varied beam energy and the total losses including the recoil energy, dead-layer losses, and detector losses was determined to be the beam energy. An example is shown in Figure 4.3. Once the beam location and energy was determined the uncertainty in the beam energy is determined by observing the scattered alpha particles detected energies while implementing a correction for the energy losses and kinematic corrections.

Applying the corrections to the alpha energy spectrum incident on the lead target resulted in Figure 4.4. Evaluating the energy distribution of the elastic peak yielded the uncertainty of the energy resolution. Assuming a Gaussian distribution for the alpha spectra lead to an uncertainty of 115.4$\pm$0.4 keV. Note the largest impact to the energy uncertainty is the resolution of the silicon detectors through ray tracing. The interaction location was assumed to be at the center of the pixel, although there are events that may occur closer to the edge reducing the energy resolution. Additionally, when using the track of the alpha particle through the ΔE and E detectors, the distance between the two interactions is assumed to be fixed at .54 cm based on the measured distances between the midpoint thickness of the two detectors. Given that the E detector is 1000 microns thick, the location in which the alpha particle stops within the detector is variable and dependent on the angle and energy of the scattered alpha. For more precise energy reconstruction the ΔE and E detectors can be read out through the total 48 rings and 16 sectors.

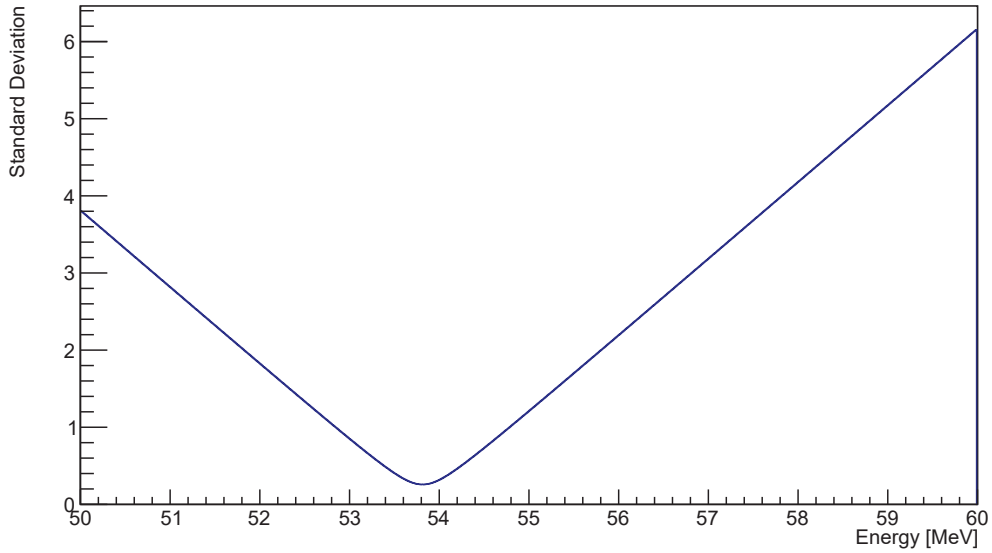

Figure 4.3: Standard deviation of the varied beam energy and energy losses difference between multiple pixel. The varied energy shows a local minima at the energy of the beam, 53.960 MeV.

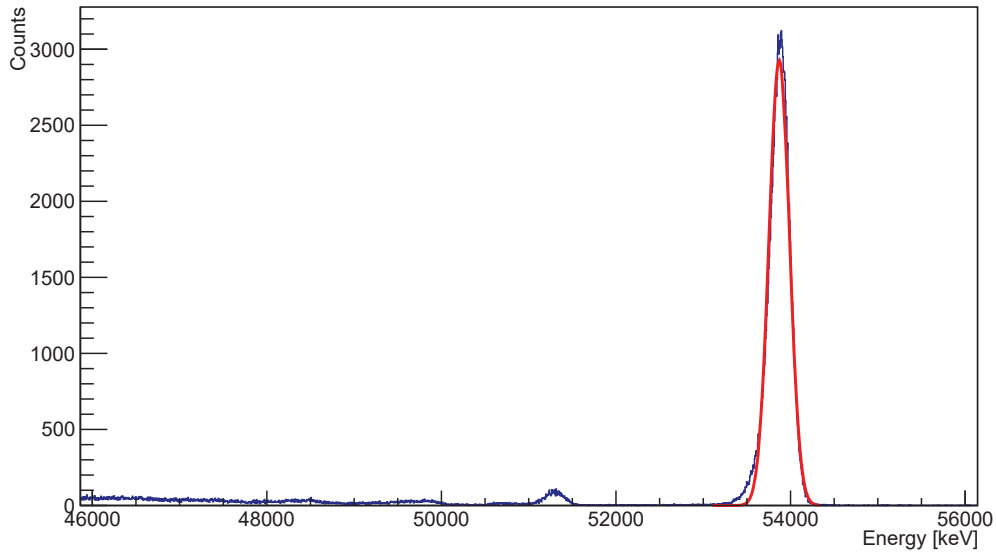

Figure 4.4: Detected scattered alpha particles on ^{208}Pb with the Gaussian fit for confirming the peak energy and determining the uncertainty in the beam energy.

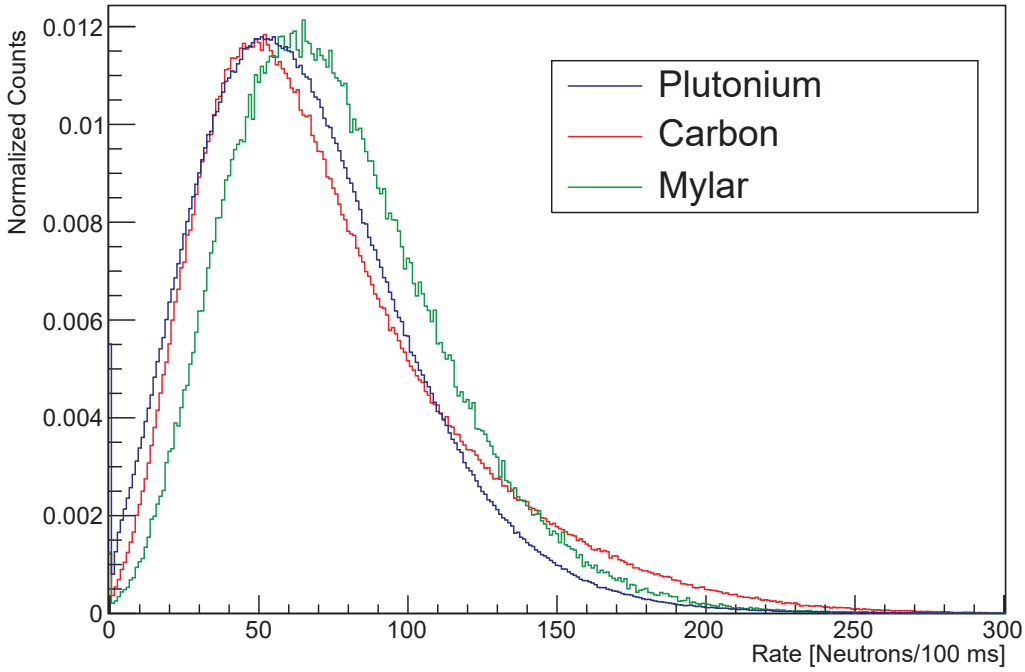

Figure 4.5: Neutron rate for Plutonium, Mylar, and Carbon throughout the experiment. The figures have been normalized based on the total number of events for each target. Due to the inconsistencies in the rate between targets and within an individual target, the experiment is broken down into multiple rate histograms for effective background subtraction.

Beam Intensity

In addition to fluctuations in the beam spot, the intensity of the beam also changed through the experiment. When the background subtraction is performed in Equation 3.5 a consistent background neutron distribution is assumed. In the case the background is not consistent, fluctuations occurring on time scales smaller than the event time do not average out the variable rate when observing neutron multiplicity distributions. As shown in Figure 4.5, the total rate (events/100 ms) in the entire NeutronBall is not consistent in time or between different target runs. To account for changes in the beam intensity the experiment is broken down into 50 groups based on the rate up to 300 events per 100 ms in the NeutronBall. From Figure 4.5 the neutron rate in the liquid scintillator follows a different distribution for the three targets. The carbon runs have a lower mean rate and narrower distribution than plutonium and Mylar, yet has a larger high rate tail. The rate within the Mylar target displayed a higher mean rate in the neutron ball than the other two targets.

Sources of Systematic Energy Uncertainty	σE [keV]
Energy Loss in Dead Layers	32 to 114
Angular Resolution	20 to 55
Energy Resolution in Telescope	42 to 64
Cyclotron Beam	60
Total Systematic Uncertainty	154 to 293

Table 4.3: Sources of systematic uncertainty for the energy resolution in the silicon telescope.

4.3 Systematic Uncertainties

From the corrections implemented in Section 4.2 and previous knowledge of the STARS array the systematic uncertainties was determined to arise from energy straggle, angular resolution, intrinsic detector energy resolution, and the cyclotron beam energy. The energy loss through dead-layers in the experiment was determined on an event-by-event basis, using the detected kinematics, detector materials and the composition of the targets. Due to the range of alpha particles relative to other light ions, the total energy loss ranged from 400 keV to 2.5 MeV. To reduce computational time, the energy loss in the material was fitted to a parameterization as a function of energy and angle. The uncertainties in the fits ranged from 32 to 114 keV.

The angular coverage of the detector spans from 30 and 65 °; given the discrete coverage of the rings, a 0.7 to 2.2 ° uncertainty in the scattered alpha particle translating into a 20-55 keV uncertainty in the recoil correction for ^{242}Pu. The δE and E detector were previously calibrated using a Radium-226 check source, the uncertainties in the detected alpha's span from 42 to 64 keV. Finally, the cyclotron beam has some spread in the energy of the alpha particles. When compiling all the apparent systematic uncertainties, the energy spread is found to range from 154 to 293 keV. A summary of the discussion in this section can be found in 4.3. Although the uncertainty in energy does not exceed 300 keV, the bin width for the results may be larger to accommodate low counting statistics.

Chapter 5

Analysis

For this work, an (n,xn) event is triggered by alpha events in the ΔE and E detector, while fission events require the additional coincidence with the detection of a fission fragment in the fission detector. Neutrons detected following this trigger are then measured to determine a neutron distribution. During the experiment, multiple events that are not of interest can deposit energy in either the ΔE/E silicons, fission detector, and/or the liquid scintillator. To reduce the contribution of background events from light ions (m $\leq$ 4 a.m.u.), fusion-fission events, muongenic/spallation events, and other sources of radiation from the room or beam; appropriate cuts to signals identified in multiple detectors must be made.

5.1 Particle Identification

Due to the energy of the incident bream, the evaporation of light particles and transfer reactions are kinematically feasible, additionally the beam halo may induce similar signals in the detectors as the scattered alpha particles of interest. When light ions induce charge in either the ΔE or E, if the interaction is close to the border of two rings or sectors, the charge is shared inducing multiple events in adjacent rings or sectors. Additionally, charge collection may induce cross-talk in adjacent pixels before the signals are amplified through pre-amplifiers. To ensure real signals are recorded, the largest energy deposition in both silicon rings or sectors is used to determine the pixel location. Sectors in the silicon detector have larger surface areas than that of the rings reducing the cross talk and charge sharing, and their energy is used as the recorded energy loss of the alpha particle.

In an effort to reduce random coincidences and backgrounds from the alpha beam, a ray trace condition must be met by events triggering the ΔE and E detector. First the silicon sectors in which the ΔE energy is registered must match the sector in which the E detector sees the particle. Second there is a tolerance for the ring number differential between the two detectors in the telescope. Only events in which the ring in the E detector exceeds the ring number in the ΔE detector by no more than 5 rings, is considered a possible trigger. The segment and ring coincidences between the ΔE and E detector are shown in Figure 5.1. The

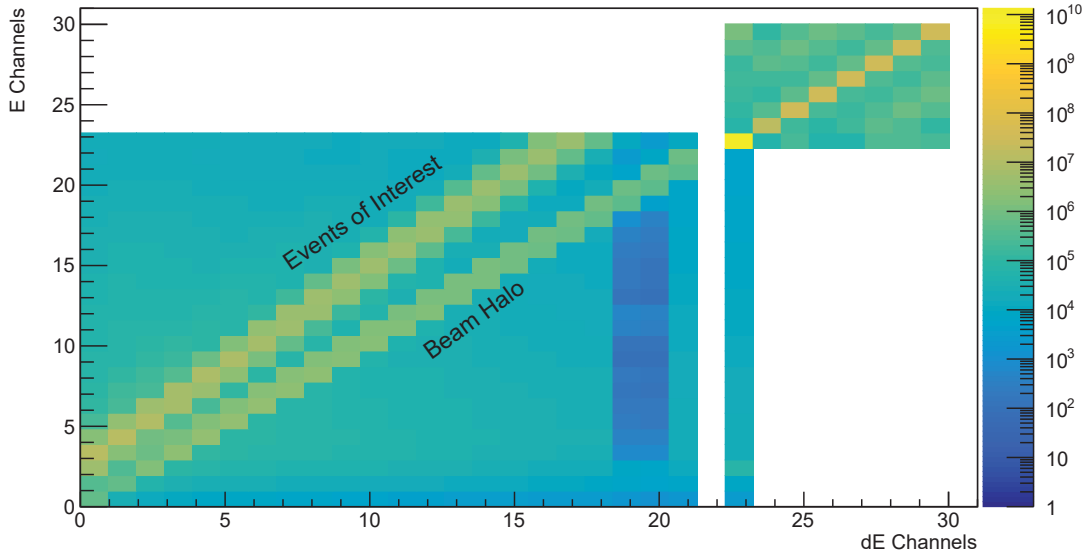

Figure 5.1: Ray Trace of the ΔE and E detectors. The 0-23 channels represent the rings while the 24-31 channels are the sector locations. Both scattered beam and events of interests can be observed.

channels 0-23 show events on the ring. Two distinct features are present around the slope ΔE=E and around ΔE < E. The first feature at ΔE=E shows the beam halo, subsequent cuts can further reduce these events. The second are the events of interest, which are also present on the sector channels' Ray Trace on the ΔE=E.

To ensure events that trigger the system are from scattered alpha particles, the energy loss in the ΔE can be plotted against the energy loss in the E detector. Recall the classical energy loss for charge particles follows the Bethe-Bloch formula:

$$-\frac{dT}{dX} = \frac{4\pi e^4 Q^2}{m_e v^2} NB \tag{5.1}$$

where the stopping number B is defined as:

$$B = Z\left(\ln\frac{2m_e v^2}{I}\ln\left(1-\frac{v^2}{c^2}\right) - \frac{v^2}{c^2}\right) \tag{5.2}$$

The energy loss is seen to be dependant on v the velocity of the charged particle, Q the charge of the particle, N the number density of absorber atoms, the atomic number of the absorber Z m_e the rest mass off the electron, e the electron charge, and the excitation and ionization potential I. For multiple charged particles incident on the same material, the mass, charge, and energy effect the stopping power and the energy loss. For this experiment, when the energy loss in the ΔE is plotted against the energy of the particle once stopped in

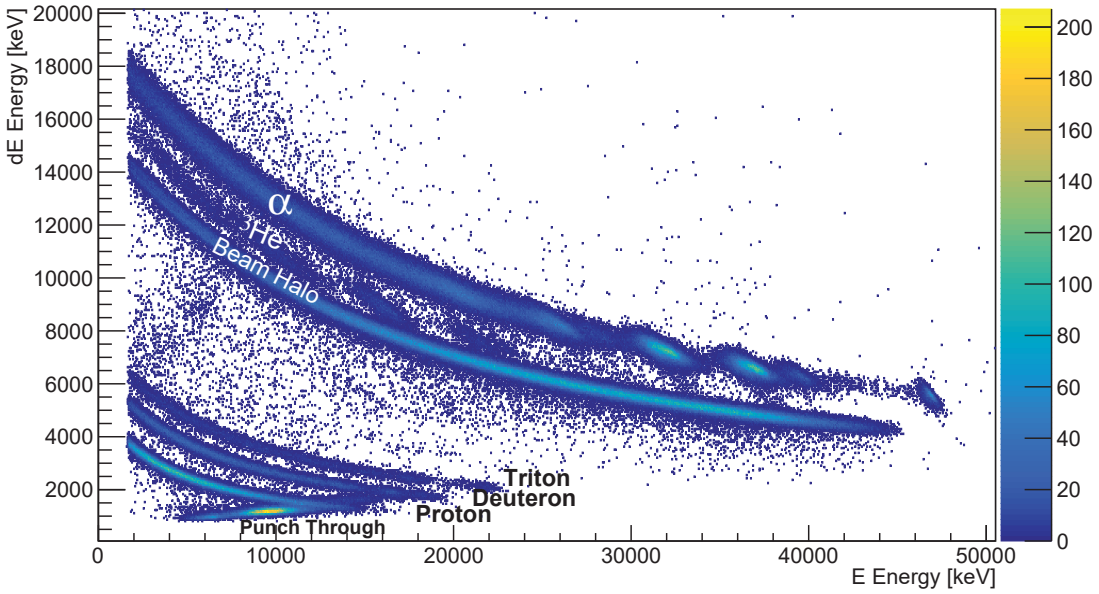

Figure 5.2: Particle Identification (PID) plot resulting from alpha particles incident on ^{242}Pu the bands in decending order represent alpha particles, ^{3}He (faint), the beam halo, tritons, deuterons, and protons.

the E, clear features distinguishing the light ions can be seen. This shows clear separation of the light ions by mass and charge.

The resulting particle identification (PID) plot can be shown in Figure 5.2. The first band shows the scattered alpha particles. Additionally, the discrete excitation of lower lying states in ^{242}Pu, carbon, and oxygen are observable in the peaks. The second faint band shows the ^{3}He ions. This band is the least intense due to the binding energy of the alpha particle. Following the ^{3}He, the next band shows the beam halo. Although the beam consists of α particles, it can be separated from the scattered particles of interest due to the angles at which the particles enter the silicon detectors. Beam related α particles have a shallow scattering angle reducing the amount of silicon the particle transverses through, which then reduces the amount of energy that can be loss by passing through the ΔE detector. The next three band from increasing ΔE energy are tritons, deuterons, and protons. The perpendicular feature to the protons are a result of so called "punch" through. In these cases the E detector was not thick enough to fully stop the proton and the full energy is not deposited.

To perform effective cuts on lower mass ions that are not of interest, empirical fits to the ΔE and E detector were applied to linearize the PID plot into an effective thickness. Instead of the energy loss as a function of the stopping energy, the total silicon distance the ions transverse in the silicon are plotted as a function of the total energy of the scattered

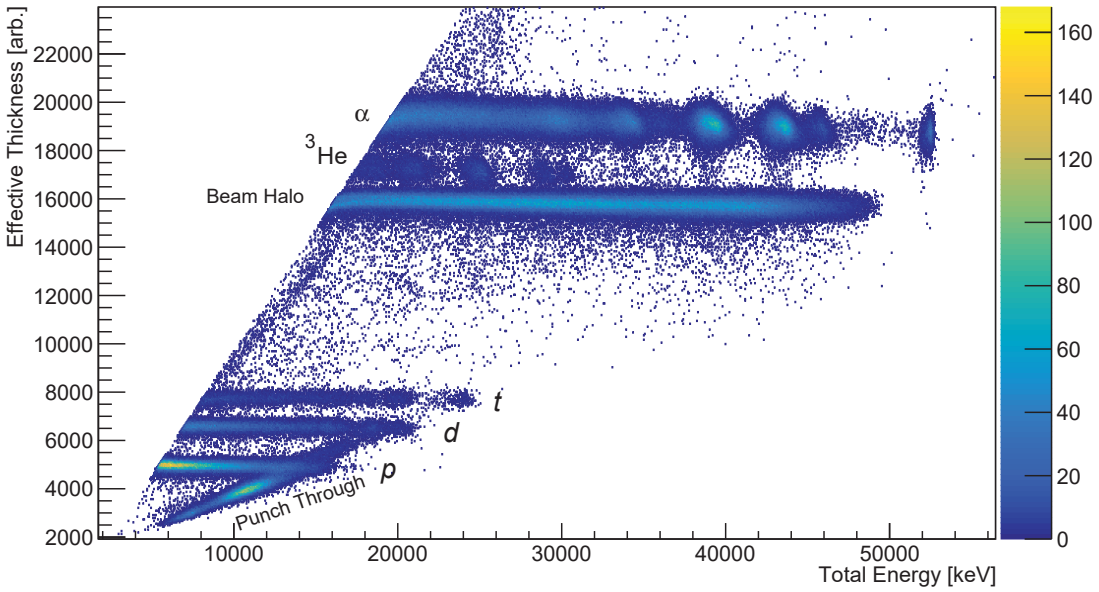

Figure 5.3: Linearized PID plot. Each light ion is located within a distinct effective thickness to representing the normalization of the variable range these particles have in silicon as a function of energy.

particles in Figure 5.3 using the following paramerteriztion:

$$PID_{lin} = 0.001\left(E_{sum}^{1.8} - \left(E_{sum} - \frac{dE}{dx} * 0.15\right)^{1.8}\right)\frac{1}{1.8} \tag{5.3}$$

The resultant features allows for software cuts to neglect events that are not alpha particles (18,000 < effective thickness < 22,000).

5.2 Alpha Particle Singles

When observing the alpha particle singles as a function of the related excitation energy in the nucleus the resulting spectrum is shown in Figure 5.4 in 500 keV energy bins. The most prominent feature are the elastic scattering events. Above 5000 keV the continuum of events contains discrete scattering events from carbon and oxygen as well as plutonium. As discussed in Section 5.4, each detected alpha particle of interest for a given energy range has a related neutron distribution. To properly attribute the neutrons that originate from ^{242}Pu, the alpha particle singles originating from carbon and oxygen must be identified and subtracted along with their corresponding neutron events.

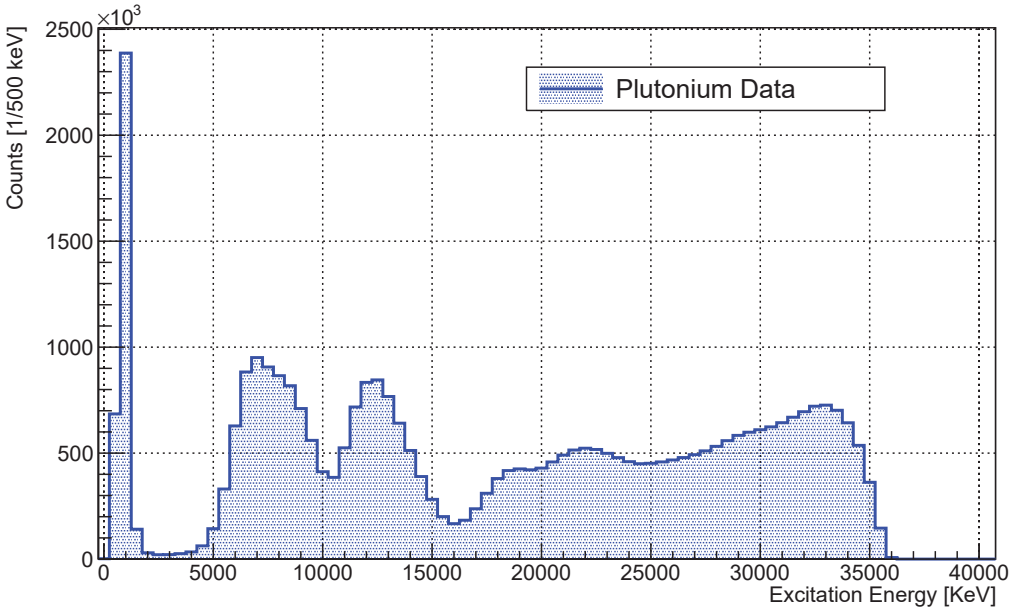

Figure 5.4: Alpha particle single events in the plutonium target. Events from carbon, oxygen, and plutonium contribute to the presented spectrum.

To evaluate the carbon and oxygen contributions in the target, the carbon backing and Mylar target were run under the same conditions. The resulting alpha particle singles are shown in Figure 5.5. In addition to the Mylar alpha particle single, the oxygen concentration can be extracted using the carbon data. Once the carbon is subtracted from the spectra, the elastic scattering and discrete excitation from the ground state and first excited state, respectively, can be observed. When comparing the carbon and oxygen alpha particle singles in Figure 5.5 to that of plutonium in Figure 5.4, it is evident that a majority of the events above 5 MeV are from the lighter elements.

To quantify the carbon and oxygen sample in the sample a Least-Squares fit to the plutonium alpha single spectrum, $\alpha_{Pu}(E)$, with a combination of the carbon,$\alpha_C(E)$, oxygen,α_O, and linear function,$L(E)$, with a negative slope was performed assuming:

$$\alpha_{Pu}(E) = L(E) + \gamma \times \alpha_C(E) + \zeta \times \alpha_O(E) \tag{5.4}$$

Here the fitted parameters γ and ζ represent the carbon and oxygen content in the spectra. Recall the elemental composition of Mylar is $C_2H_6O_2$. Previous surrogates have shown the contribution of particle scatters off hydrogen are negligible to the final result [43]. Including the alpha singles from Mylar directly results in the following:

$$\alpha_{Pu}(E) = L(E) + (\gamma - \zeta)\alpha_C(E) + \zeta(\alpha_O(E) + \alpha_C(E)) \tag{5.5}$$

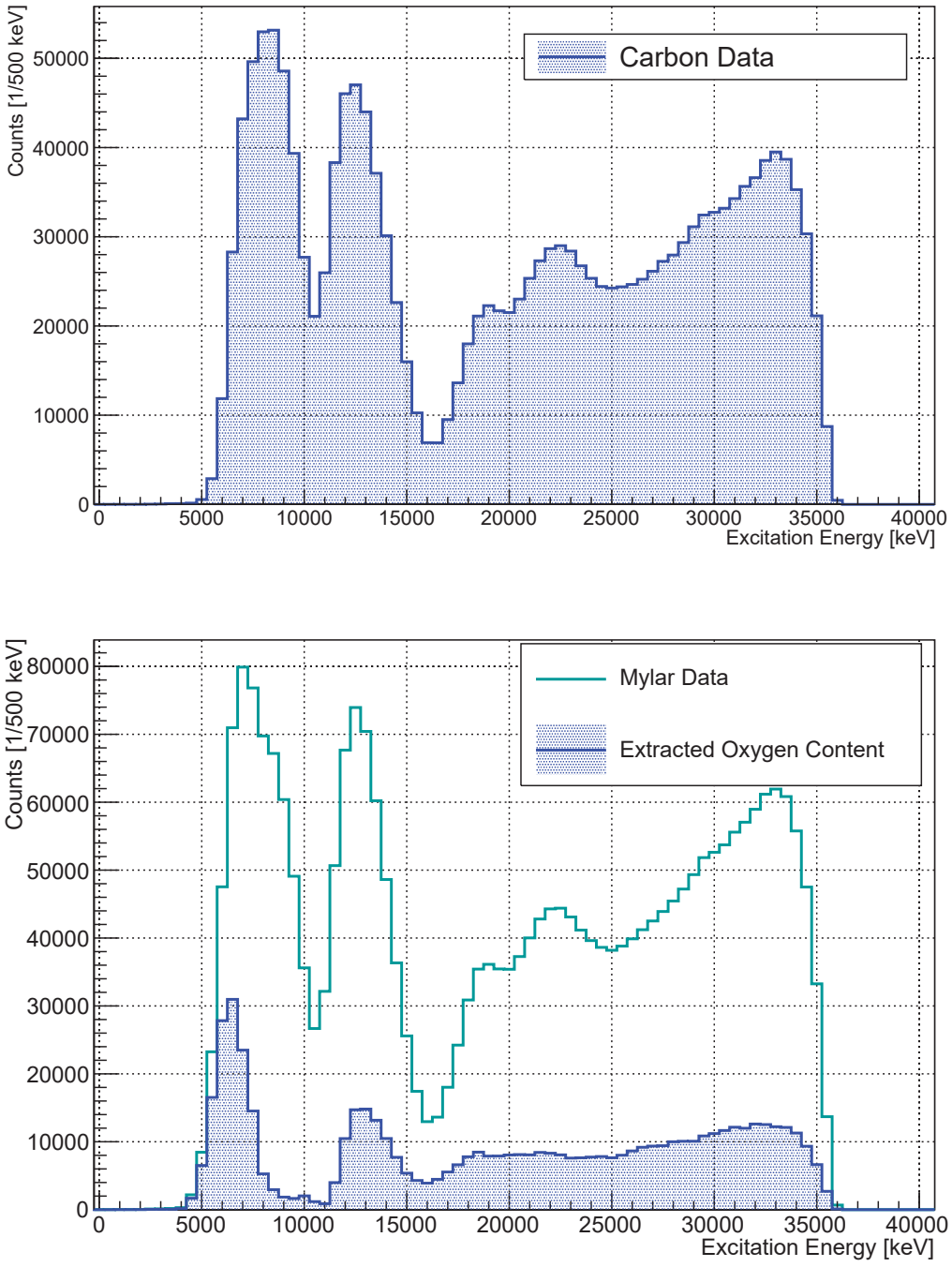

Figure 5.5: Alpha particle singles for Carbon [Top] and Mylar [Bottom] targets in the recoil correction frame for ^{242}Pu. The carbon content has been subtracted from the Mylar target using the carbon spectrum to observe events pertaining to oxygen.

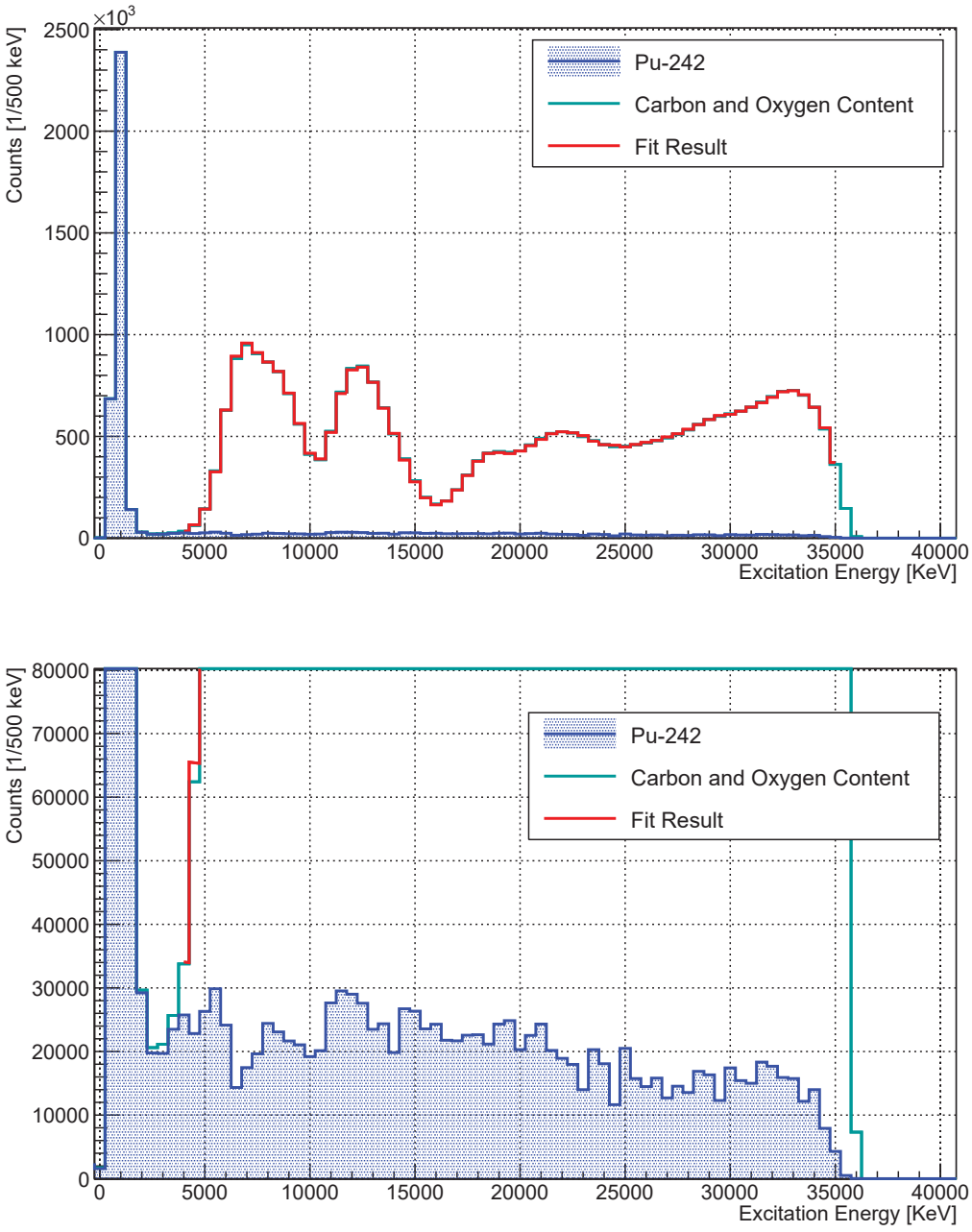

Figure 5.6: Result of the subtraction of the carbon and oxygen content from the plutonium alpha particle singles. Both the top and bottom figures are the same but due to the relative contribution of scattering events from light elements to plutonium in the target, the bottom plot shows the plutonium alpha singles in detail.

The scaled Mylar contribution, $\zeta'\alpha_M(E) = \zeta(\alpha_O(E)+\alpha_C(E))$, accomidated both the oxygen content and a fraction of the carbon content. The remaining carbon events can be subtracted by using the events from the carbon backing target,$\gamma'\alpha_{Cb}(E) = (\gamma-\zeta)\alpha_C(E)$. Reducing the equation to only use the carbon and Mylar target results in:

$$\alpha_{Pu}(E) = L(E) + \gamma'\alpha_{Cb}(E) + \zeta'\alpha_M(E) \tag{5.6}$$

The resultant spectral fit can be seen in Figure 5.6. Once the carbon and mylar are subtracted, the remaining events contain inelastic scattering from ^{242}Pu.

5.3 Fission Identification

Events needed to characterize the fission neutron multiplicities required a triple coincidence between the ΔE, E, and Fission silicon detectors. The fission detector spectrum for the plutonium target is shown in 5.7 over all angular ranges in the detector. The fission detector is capable of detecting light ions as well as fission fragments, and the alpha particles from the natural decay of ^{242}Pu can be seen at lower energies. Due to the pulse height defect from the fission fragments used to calibrate the fission detector and alpha particles, the energy deposited from alpha decay is registered higher than the expected 4.90 MeV (BR=77.5 %) and 4.896 MeV (BR=22.4 %) alphas. The broad higher energy continuum shows the fission fragments from ^{242}Pu. To properly understand the contribution of the carbon and oxygen elements in the target, the fission detector spectra from the carbon and Mylar target were analyzed, the resulting spectra can be seen in Figure 5.8.

Here, events can be seen in the fission detector from the break-up of carbon and oxygen into multiple alpha particles. From the Mylar fission spectrum, the oxygen events are lower in energy than the carbon due to the energy sharing of the emitted alpha particles as the carbon breaks up into three alpha particles while it is assumed that oxygen breaks up into one alpha particle and carbon-12 evident by the double peak shown in the fission detector spectrum. These break-up events only occur at lower energies within the fission detector.

To avoid false triggers from carbon, oxygen, and alpha particles from the decay of ^{242}Pu; a 40 MeV threshold is set on the fission detector. The largest source of neutron emission in the experiment occurs from fusion-fission events. Here the alpha particle is absorbed by the ^{242}Pu nucleus and undergoes fission. The coincidence gate between the silicon telescope and the fission detector is about 3 microseconds long. As a result random fusion-fission events in coincidence with scattering events off of carbon and oxygen in the target can mimic a surrogate fission event. Due to the high rate of both occurring throughout the experiment this background is non-negligible. To remove the contribution of false fission triggers in the experiment, a coincidence window and background window between the E detector and fission detector firing was taken. In Figure 5.9 the time difference spectrum shows the true fission events in coincidence with $t = 0$ sitting upon an oscillate background from the cyclotron frequency. The signal fission events was taken at a time of -50 to 150 ns, while the background was characterized using the timing window 250 to 2000 ns.

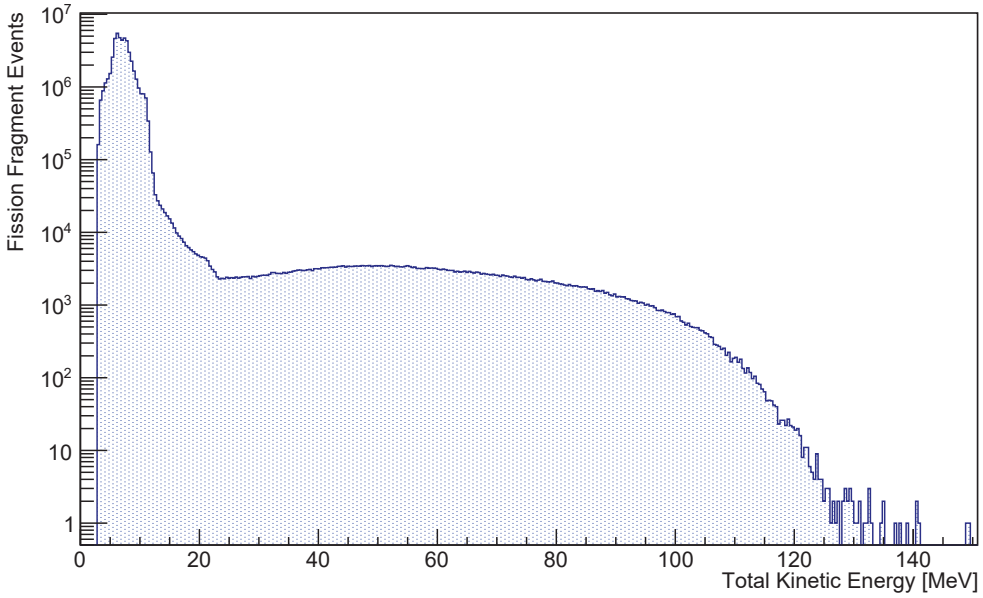

Figure 5.7: Fission detector spectrum from ^{242}Pu(α,α'f). The low energy feature shows contributions from alpha decay and the breakup of lighter elements in the sample. Above 30 MeV the fission fragment energy deposition in the fission detector is evident. Note the spectra is summed over all angles and energies reducing the ability to clearly distinguish the light and heavy fission fragment.

The resulting fission spectra as a function of excitation energy from ^{242}Pu fission as a result of inelastic scattering by alpha particles can be seen in Figure 5.10. Here features consistent with nuclear structure are present. Below the neutron separation energy, S_n = 6.31 MeV few sub-barrier fission events occur until S_n where the fission rate is the most intense. At other separation energies: 11.6 MeV, 18.1 MeV, and 23.8 MeV evidence of multi-chance fission is present from the shallow peaks in the spectrum. The excitation energy corresponding the the alpha particle energy at which the Coulomb barrier is penetrated occurs at 30.6 MeV. Here a sharp decrease in fission events can be seen due to the competition with fusion and nuclear scattering.

Quantifying the occurrence of fission events in the analysis has multiple applications. The fission neutron multiplicity analysis is a branching ratio normalized to the fission events observed. Additionally, the (n,xn) cross sections are based on a ratio with the recorded fission events from ^{242}Pu(α, α'f) and the known fission cross section for ^{241}Pu.

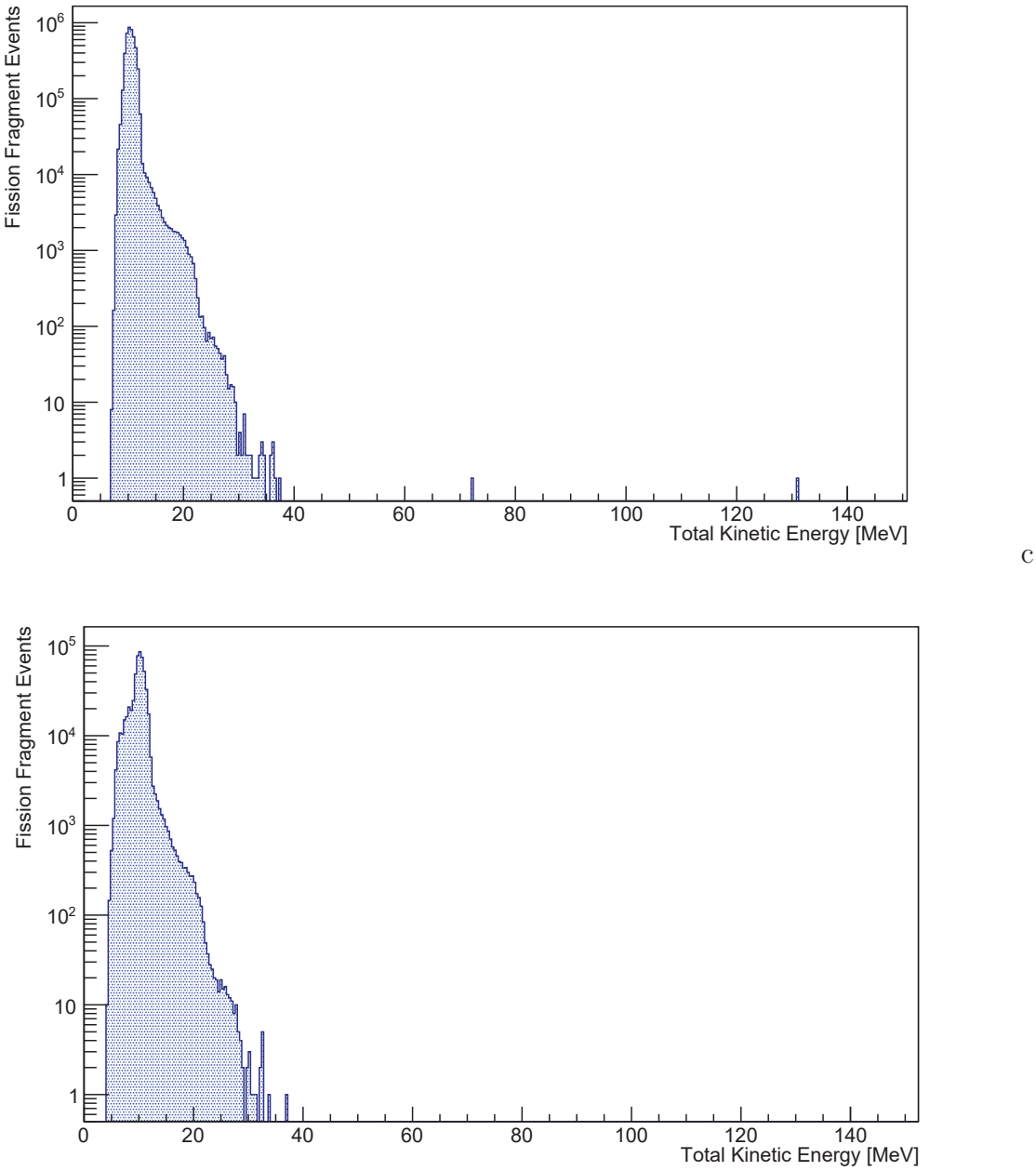

Figure 5.8: Fission detector spectrum from the Carbon [Top] and Mylar [Bottom] targets. Note the difference in scale on the X-axis between the plutonium runs from the carbon and Mylar targets.

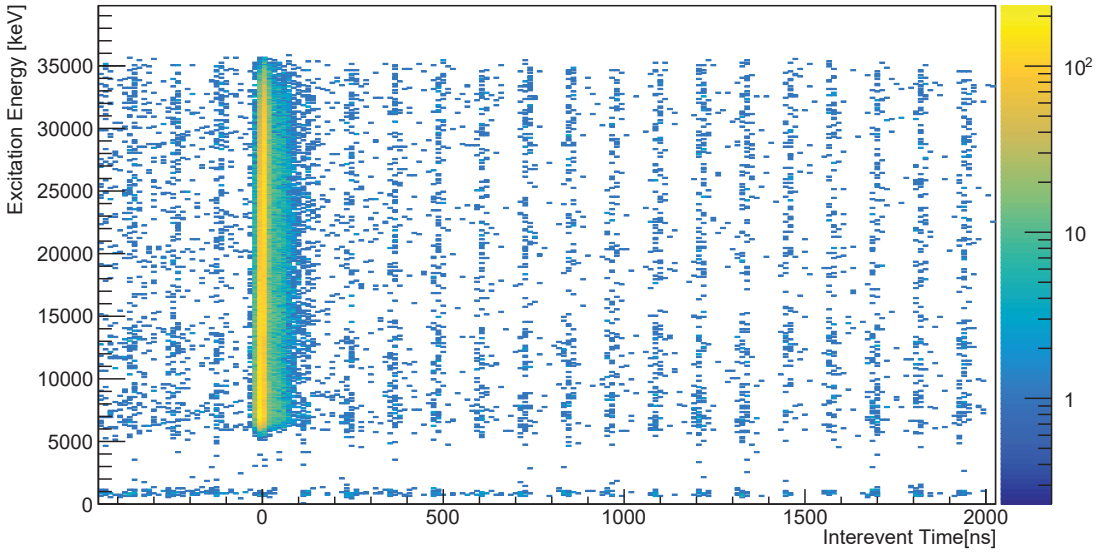

Figure 5.9: Timing distribution between the silicon telescope and the fission detector as a function of excitation energy in the ^{242}Pu target.

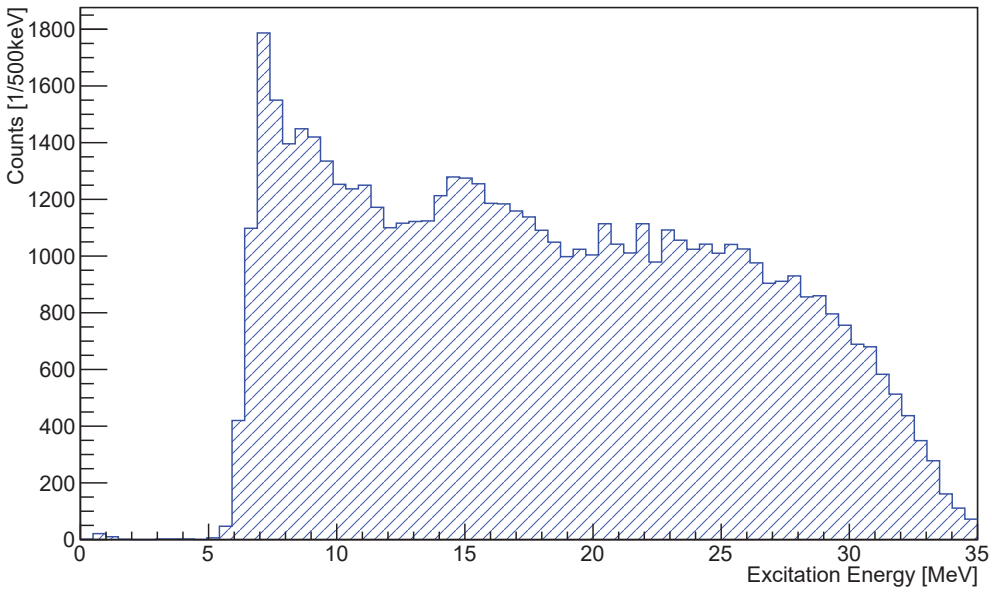

Figure 5.10: ^{242}Pu(α,α'f) events following corrections for accidental fusion-fission backgrounds.

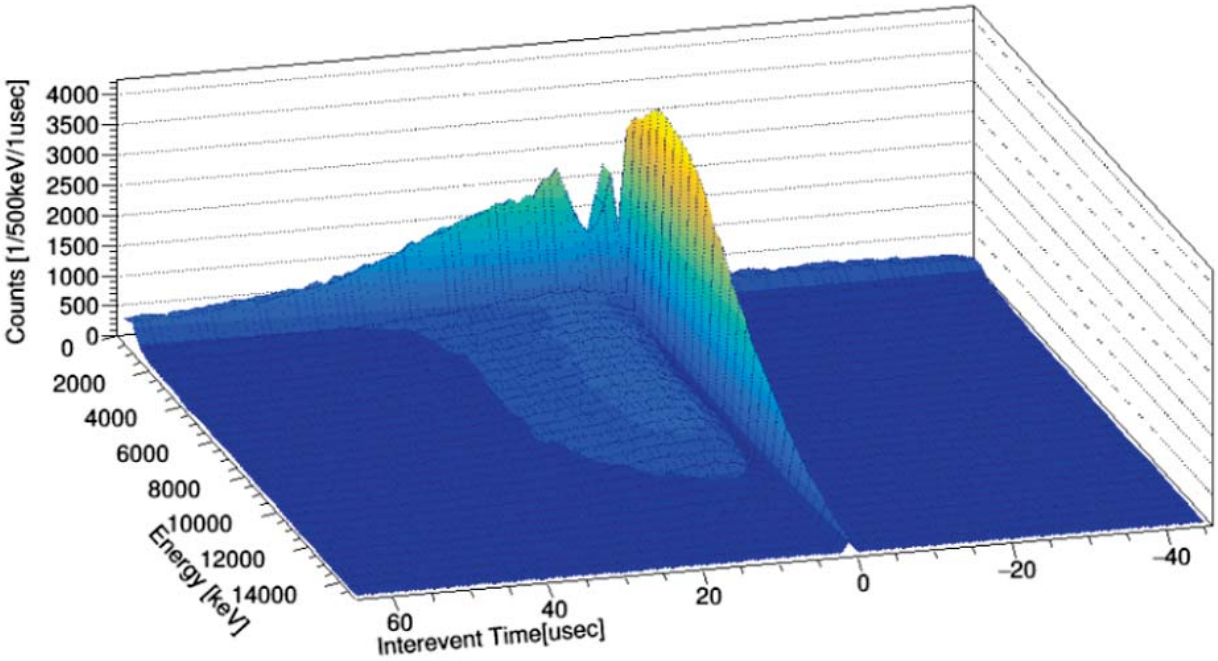

Figure 5.11: Correlated energy deposition in the NeutronBall as a function of time between event triggers in the target chamber.

5.4 Correlated Neutron Detection

Once an event triggers either the silicon telescope with or without a fission coincidence, correlated neutrons detected in NeutronBall are used to determine the neutron multiplicity of the events. Figure 5.11 shows the energy deposition as a function of time from an event trigger in NeutronBall. The most prominent features are seen at $t = 0$ and $E = 0$. At negative times the distribution of events in NeutronBall is flat due to the Poisson or random characteristics of neutrons produced. At $t = 0$ prompt gamma-rays from fission, and discrete excitation of states from light elements can be seen. A few microseconds following the gamma-ray flash, the gamma-ray cascade from neutron captures on gadolinium can be seen. Due to the thermalization time of neutrons relative to the transit time of prompt gamma-rays, there is a distinct separation in time between the two.

At lower energies evidence of ion after pulsing and phosphorescence are present. These events are caused by large energy deposition in the scintillator that either liberate a contaminant ion on the inner surface of the PMT face or from excitation of the scintillator into the triplet states with a longer decay time. As a result these events mirror the fission flash and the neutron capture events. Due to the time dependence of these events, applying the background correction to subtract their influence on the result is not sufficient. Instead, a low energy cut of 2 MeV is applied to the analysis.

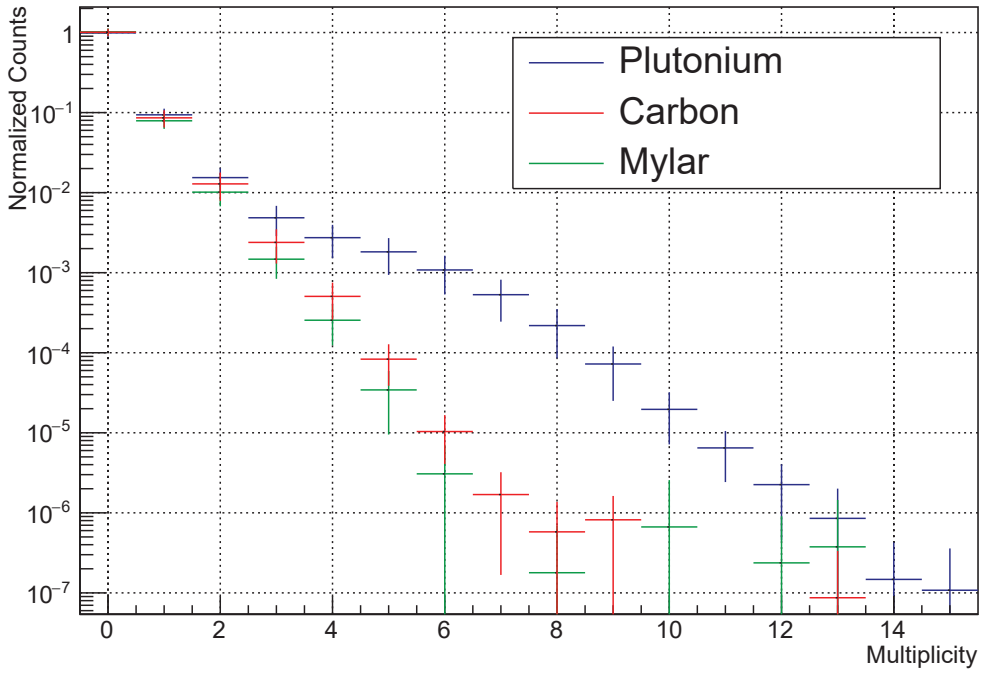

Figure 5.12: Neutron multiplicity of the backgrounds in the Mylar, carbon, and plutonium target. The uncertainties in the figures represents the standard deviation between the ten groups in each target.

The same multiplicity reconstruction described in Section 3.4 is applied to this analysis at each 500 keV energy bin, for the ten rate-based groups described in Section 4.2. In Figure 5.12 the normalized background multiplicity and standard deviation (represented as errors) are shown for the ten groups in each target. Although the background has been shown to be flat, the rate at which events occur does effect the multiplicity in the background in an event by event analysis. Additionally, when comparing the background distribution among the three targets, the Plutonium target background multiplicity shows higher order neutron multiplicities due to the fusion-fission and fission in the target that is not present in Mylar or Carbon. Due to the thickness of the Mylar target relative to the carbon target, fewer higher multiplicity events are observable.

Similarly to the ^{252}Cf multiplicity reconstruction, the background distribution is removed from the prompt neutron detection spectrum using the matrix operations described in Equation 3.5 and 3.6. Recall using this approach the net detected neutrons $D[D_i]$ is determined by a fit of the real neutrons of interest multiplied by the background distribution $B[b_i]$ to the neutrons in the prompt gate $P[P_i]$.

$$\begin{bmatrix} P_0 & P_1 & P_2 & \dots & P_{N-1} & P_N \end{bmatrix} = \begin{bmatrix} D_0 & D_1 & D_2 & \dots & D_{N-1} & D_N \end{bmatrix} \begin{bmatrix} b_0 & b_1 & b_2 & \dots & b_N & \\ 0 & b_1 & b_2 & \dots & b_{N-1} & \\ \vdots & \vdots & \vdots & \ddots & \vdots & \\ 0 & 0 & 0 & \dots & b_0 & b_1 \\ 0 & 0 & 0 & \dots & 0 & b_0 \end{bmatrix} \quad (5.7)$$

The signal neutrons for the targets and data streams of interest are shown in Figure 5.13 and 5.14. In the carbon, Mylar, and plutonium (non-fission) data most of the events are contained in the zero neutron multiplicity channel. This is due to the overwhelming rate of elastic scattering events on oxygen and carbon in addition with discrete excitation from the higher lying states. Moreover, the one neutron channel in these targets is populated by the neutron emission from the naturally occurring ^{13}C and ^{17}O isotopes in the targets. For fission the detected neutron multiplicity rises as a function of excitation energy. Due to the triple coincidence required to observe these events, the zero and one neutron events do not overwhelm the detected neutron distribution.

5.5 Extracting (α,α'xn) and Fission Neutrons

Neutrons correlated to a fission tag were considered fission neutrons, while any neutron (or zero neutrons) in coincidence with only the silicon telescope and not the fission detector are candidates for (α,α'xn). Following adjustments for rates in the experiment and background corrections, the quantity of interest for fission and (α,α'xn) were determined.

Fission

The average neutron multiplicity, $\bar{\nu}(E)$ for ^{241}Pu was determined by a simple comparison between the events in the prompt gate, $P(E)$, and background gates, $B(E)$, relative to the total number of fissions observed at each energy, $F(E)$ corrected for the contributions from fusion-fission:

$$\bar{\nu}(E) = \frac{\sum P_i(E) \times i - \sum B_i(E) \times i}{\sum F_i(E) \times i} \times \frac{1}{\varepsilon} \quad (5.8)$$

Here ε refers to the efficiency of the array as determined in Section 3.3. The uncertainties for the neutrons in both gates and the total number of fission events follow basic counting statistics $\sqrt{N}$, propagated to include the subtracted contribution of elastic scattering in coincidence with fusion-fission. The uncertainty of the efficiency was previously determined using a ^{252}Cf source. A summary of the total uncertainty pertaining to $\bar{\nu}(E)$ can be seen in Table 5.1. The dominant source of uncertainty arises from the total number of fission events in the experiment. The contribution from Fusion-Fission would be larger if the entire 2500

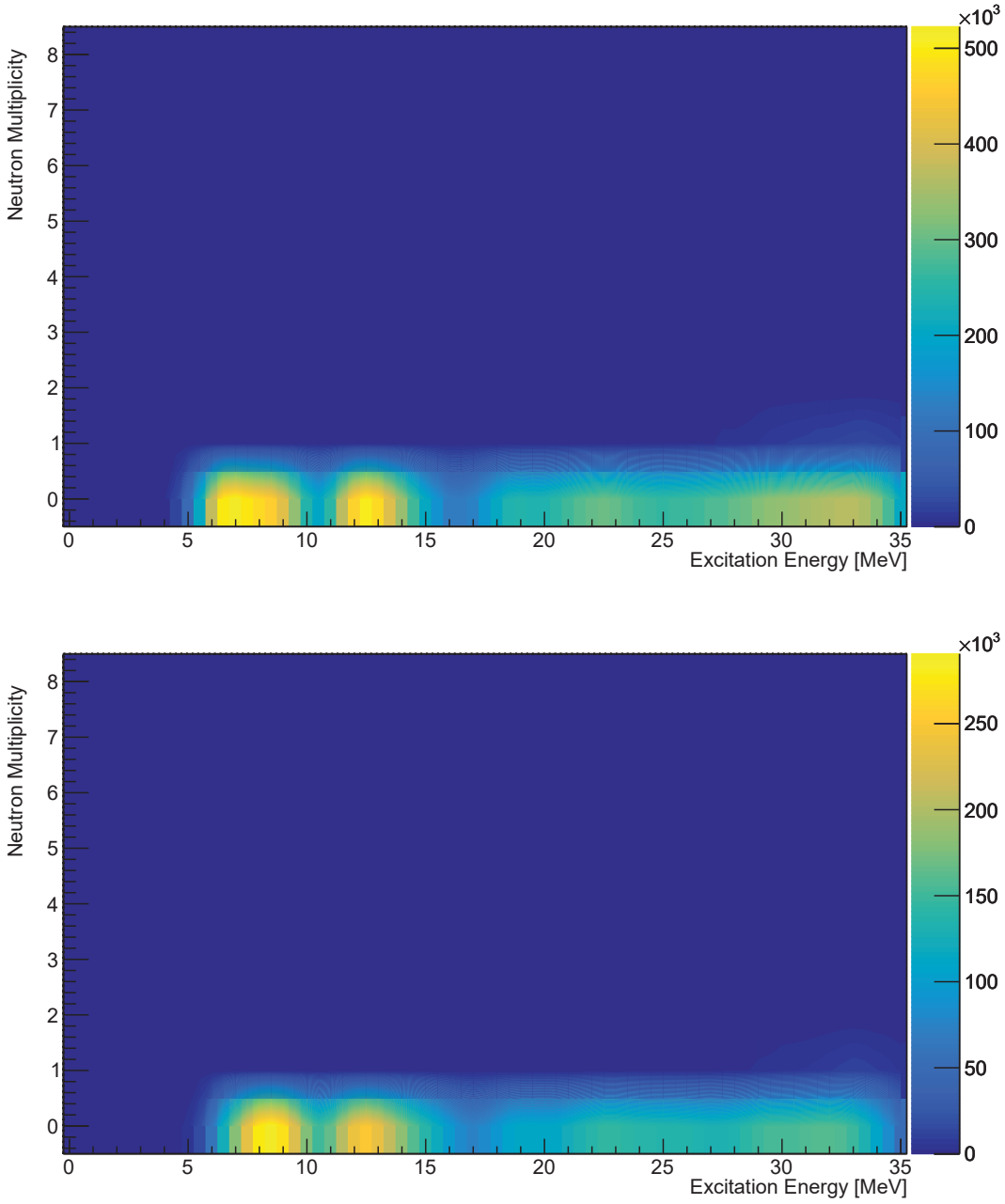

Figure 5.13: Background corrected counts as a function of excitation energy for Mylar(α,α'xn) [Top] and Carbon(α,α'xn) [Bottom] targets as a function of neutron multiplicity. The zero multiplicity channel dominates both spectra, with some event in the one neutron multiplicity bin.

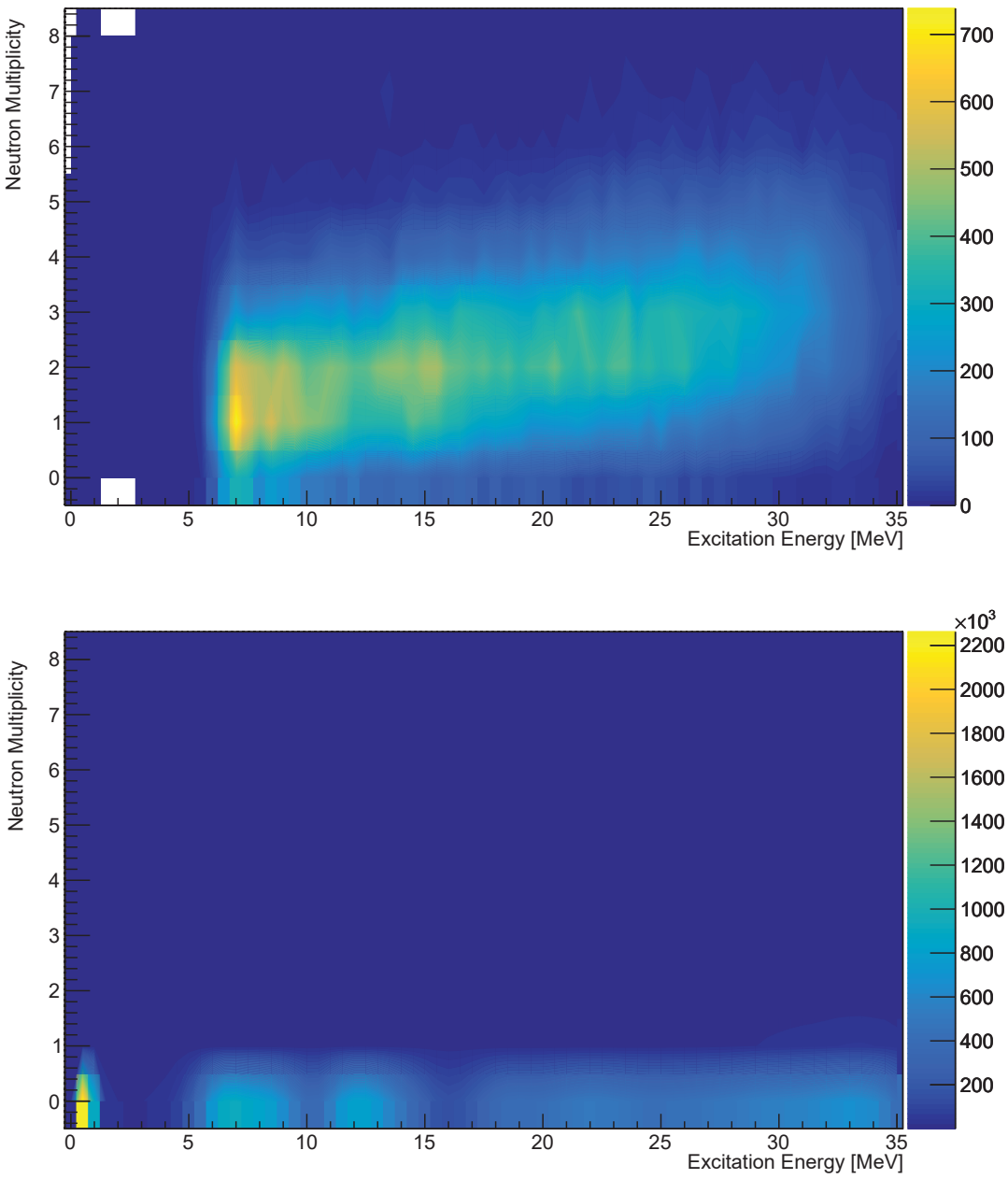

Figure 5.14: Background corrected counts as a function of excitation energy for ^{242}Pu (α,α'fxn) [Top] and ^{242}Pu (α,α'xn) [Bottom] as a function of neutron multiplicity.

Parameter	Uncertainty
Prompt Neutrons	1.8-2.0%
Background Neutrons	0.48-0.67%
Fission Counts	2.3-3.1%
Fusion-Fission	0.28-0.46 %
Efficiency	0.53 %
Total Uncertainty	3.2-4.1%

Table 5.1: Uncertainties in the average neutron multiplicity from fission for ^{241}Pu. The largest source of uncertainty arises from the total number of fissions observed in the experiment.

ns gate between the E detector and the fission detector were observed, the prompt fission gate reduced this contribution by an order of magnitude.

Similarly to the ^{252}Cf multiplicity re-construction, the fission neutron multiplicity was determined by making a fit of the background corrected detected neutron distribution to a skewed Gaussian distribution multiplied by the Binomial matrix reflecting the efficiency of the array, ε:

$$\begin{bmatrix} D_0 & D_1 & D_2 & \dots & D_N \end{bmatrix} = \\ \begin{bmatrix} G_0 & G_1 & G_2 & \dots & G_N \end{bmatrix} \begin{bmatrix} 1 & 0 & \dots & 0 \\ \binom{1}{0}(1-\varepsilon)^1\varepsilon^0 & \binom{1}{1}(1-\varepsilon)^0\varepsilon^1 & \dots & 0 \\ \vdots & \vdots & \ddots & \vdots \\ \binom{N}{0}(1-\varepsilon)^N\varepsilon^0 & \binom{N}{1}(1-\varepsilon)^{N-1}\varepsilon^1 & \dots & \binom{N}{k}(1-\varepsilon)^{N-k}\varepsilon^k \end{bmatrix} \quad (5.9)$$

Here the emitted neutrons, $G[G_\nu]$ are composed of the skewed Gaussian distribution:

$$G[\nu] = \frac{1}{2\pi\sigma^2}\exp\left(\frac{(\nu-\mu)^2}{2\sigma^2}\right)\left(1+\mathrm{erf}\left(\frac{\beta(\nu-\mu)}{\sqrt{2}\sigma}\right)\right) \quad (5.10)$$

Here μ, σ, and β refer to the average of the distribution. the standard deviation and the skew parameter respectively. Note the the average of the distribution is not the same as the expectation value of the function, $P(\nu)$, or the average neutron multiplicity, $\bar{\nu}$. For a given σ and μ the normal distribution can extend to negative values, while the neutron multiplicity must remain in physical parameters (i.e $\nu \geq 0$). The reduced χ^2 for these measurements ranged from .161 to 4.65; although a Gaussian based shape is assumed the poor agreement in some of the fits at given energies show a deviation from this distribution. From the fitted multiplicity distribution the neutron multiplicity moments ν_1, ν_2, and ν_3 can be derived.

$$\nu_1 = \sum_{\nu=1}^{max} \nu P(\nu) \quad (5.11)$$

Parameter	Uncertainty		
	ν_1	ν_2	ν_3
μ	1.33-6.90%	0.31-7.93%	1.15-20.8%
σ	<0.1-2.40%	3.14-16.3%	5.08-31.4%
β	<0.1-3.42%	<0.1-8.80%	<0.1-7.69%
Total Uncertainty	2.02-11.9%	4.78-34.7%	7.96-64.3%

Table 5.2: Summary of skewed Gaussian parameters to the range of uncertainties in the fission neutron moments.

$$\nu_2 = \sum_{\nu=2}^{max} \nu(\nu-1)P(\nu) \tag{5.12}$$

$$\nu_3 = \sum_{\nu=3}^{max} \nu(\nu-1)(\nu-2)P(\nu) \tag{5.13}$$

Note, ν_1 is the same value as $\bar{\nu}$ which was determined directly. The comparison between the two serves to provide consistency between the two parameters. A summary of the parameters' uncertainty contribution can be found in Table 5.2. The uncertainties increase as the uncertainties increment, however large uncertainties in given fits skew the average uncertainties for the higher order moments.

^{242}Pu(α,α'xn)

A coincidence in the ΔE and E detector the raw spectra contains elastic and inelastic scattering events on carbon and Oxygen, which is accounted for through recorded events on Mylar and Carbon targets.

$$\phi = \frac{(1-\varepsilon_f)}{\varepsilon_f} \tag{5.14}$$

Here ϕ represents the scaling factor needed to correct for the percentage of fission detected in the fission detector, where ε_f is the efficiency of the fission detector; and ^{242}Pu(α,α'xn) reactions. Following background corrections to the raw ^{242}Pu, fission, carbon, and Mylar spectra; the detected (α,α'xn) reactions were determined by subtracting the carbon and Mylar neutron contributions determined in Equation 5.6. Neutrons in the 4-6 multiplicity range was assumed to be attributed to fission. Although the efficiency of the fission detector was previously determined using a ^{252}Cf source, the differences in target geometry and fragment excitation energy may have an effect the detection of fragments. As a result the higher multiplicities (4-6) were fitted as a function of energy to the same multiplicity of the energy dependent fission spectrum. Note, the same factor to scale the fission spectrum, ϕ, is again used in the fission ratio to extract the cross-section. The detected (α,α'xn) can be determined as follows:

$$D_{(\alpha,\alpha' xn)}(E,M) = D_{Raw}(E,M) - \gamma' D_C(E,M) - \zeta' D_{My}(E,M) - \phi D_F(E,M) \tag{5.15}$$

Here the coefficients are consistent with those used in Equation 5.6, and the subscripts refer to the detected spectra mentioned in the discussion above. The multiplicity in the zero neutron channel is primary caused from the carbon and Mylar spectrum. Following the

Parameter	Uncertainty
Detected Spectrum	<0.1-12.64 %
Efficiency	12.4-32.4%
Carbon Spectrum	2.64-15.5%
Mylar Spectrum	4.44-16.2%
Fission Spectrum	5.21-16.1%
Fission Cross-Section	2.41-5.64%
Total Uncertainty	14.6-44.8 %

Table 5.3: Summary of uncertainties that contributed to the total error in the (n,xn) cross sections used in the analysis.

subtraction the detected counts were corrected for the efficiency of the array. Unlike the fission neutron multiplicities (n,xn) reactions do not follow a pre-defined shape, and the emitted neutrons were determined directly by making a fit to the individual constituents in $E[E_i]$. Due to the energy distribution of neutrons due to the excitation energy of the nucleus, and the multiplicity distribution the efficiency of the array was consistent for each reaction. As a result the efficiency correction in 5.16 can be modified using the efficiency determined in Section 3.3:

$$\begin{bmatrix} D_0 & D_1 & D_2 & D_3 \end{bmatrix} = \begin{bmatrix} E_0 & E_1 & E_2 & E_3 \end{bmatrix} \times \begin{bmatrix} 1 & 0 & 0 & 0 \\ \binom{1}{0}(1-\varepsilon_{n,n'})^1 & \binom{1}{1}\varepsilon^1_{n,n'} & 0 & 0 \\ \binom{2}{0}(1-\varepsilon_{n,2n})^2 & \binom{2}{1}(1-\varepsilon_{n,2n})^1\varepsilon^1_{n,2n} & \binom{2}{1}\varepsilon^2_{n,2n} & 0 \\ \binom{3}{0}(1-\varepsilon_{n,3n})^3 & \binom{3}{1}(1-\varepsilon_{n,3n})^2\varepsilon^1_{n,3n} & \binom{3}{2}(1-\varepsilon_{n,3n})^1\varepsilon^2_{n,3n} & \binom{3}{3}\varepsilon^3_{n,3n} \end{bmatrix} \tag{5.16}$$

The efficiency correction results in the measured ^{242}Pu(α,α'xn) reactions. To convert this quantity into a cross section a ratio is made using the fission events occurring during the experiments and the ^{241}Pu fission cross section, previously measured by Tovesson and Hill [46]. The resulting ^{241}Pu(n,xn) reaction can be determined using the following:

$$\sigma_{^{241}Pu(n,xn)} = \frac{E_x \times \varepsilon_f}{N_f} \times \sigma_{^{241}Pu(f)} \tag{5.17}$$

Note the efficiency of the fission detector is energy dependent and determined through the ratio of the higher order neutron multiplicities in both the fission and raw spectrum:

$$\varepsilon_f = \frac{1}{\phi + 1} \tag{5.18}$$

The uncertainty in the surrogate cross section is then determined by the results of the fit, the known fission cross-section, the fission fraction, the fission efficiency, the efficiency of the neutron detector, and the detected (α,α'xn) counts. To determine the contribution from individual uncertainties to the final result a Monte Carlo approach based on the uncertainties in the individual parameters was implemented.

A summary of the error contributions can be found in Table 5.3. Although the final results are represented as (n,n),(n,2n), and (n,3n) the uncertainties are correlated across the multiple cross sections as well as through the energy ranges. The statistical uncertainty contains the square root of the counts in each bin for ^{242}Pu (α,α'xn), ^{242}Pu (α,α'fxn), Mylar(α,α'xn), and Carbon(α,α'fxn). The uncertainty in the fission cross-section used for the ratio is predetermined from the original publication and is correlated with the neutron multiplicities as a function of energy [46]. Correlated uncertainties for individual cross-sections as a function of energy include the Carbon, Mylar, and Fission scale factors as determined by the fits from their subtraction.

Chapter 6

Results

The results of the analysis are expressed in terms of the equivalent neutron energy by relating the excitation energy of the ^{242}Pu nucleus to that of ^{241}Pu by implementing the Equation 1.10. For quantities with existing data, a comparison between the previous measurements and the current work can be found in the subsequent text.

6.1 Fission Neutron Multiplicity

The results of the average neutron multiplicity as a function of equivalent neutron energy can be found in Figure 6.1. The results are compared to direct measurements where a large liquid scintillator was used to detect emitted neutrons. When compared to the previous literature the average neutron multiplicity agrees at lower equivalent neutron energy. A systematic disagreement at 12 MeV is apparent between this work and Frehaut's data although all results are consistent within the uncertainties reported for both experiments. Sources of the disagreement may arise from multiple factors. In Frehaut's experiment the target consisted of 97% ^{241}Pu. Although the isotopic contribution of the contaminants are not identified, the purity of the of the sample is enough to account for the 1% discrepancy. Additionally, the 12 MeV energy threshold for the discrepancy is consistent with that of pre-equilibrium. In a direct reaction a neutron incident on ^{241}Pu may interact with individual nucleons causing an (n,2n) reaction. If excess energy is left in the residual nucleus it may de-excite through fission. As mentioned in Section 2.1 and 2.3 using (α,α') reactions removes all contributions from pre-equilibrium for the energy range in this analysis. The multiplicity result represents fission caused from the compound nucleus of ^{242}Pu.

Following a fit to the detected fission multiplicity spectrum to the known efficiency integrated with the skewed Normal distribution with floating parameters, the μ, σ, and β terms were determined and are reported in A. Note, the μ term typically refers to the average of a distribution, but when observing the $P(\nu)$ and $\bar{\nu}$ terms the two are different. Numerically a Gaussian distribution can extend below zero, but for fission neutrons the spectrum is confined to non-negative numbers. Figure 6.2 was constructed by applying all the parameter

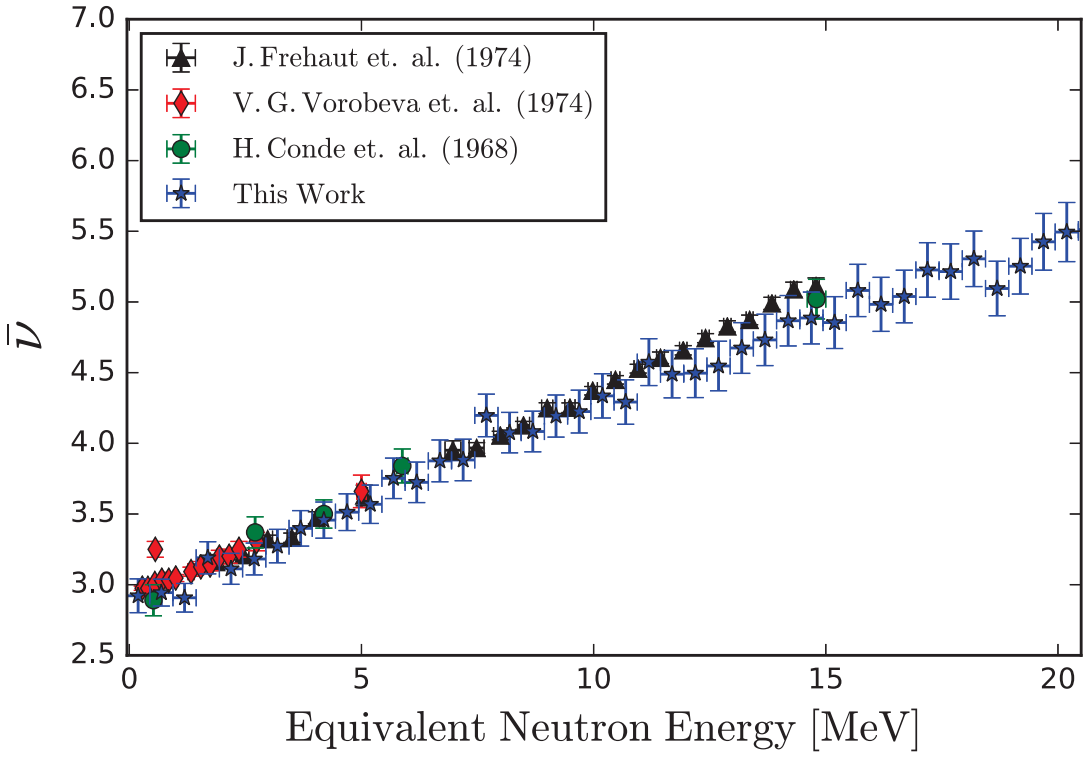

Figure 6.1: Results of the average neutron multiplicity for ^{241}Pu compared to the existing literature. The results presented from this work are in agreement with previous measurements and expand the known quantities of $\bar{\nu}$ for ^{241}Pu from 14 MeV up to 20 MeV.The present work is compared with results from J.Frehaut et. al, V.G. Vorobeva et. al, and H. Conde et. al [8, 11, 15].

terms as a function of energy in 500 keV bins from from 0 to 20 MeV. From Figure 6.2, bin to bin discontinuities in both σ and μ are apparent. One would assume that the peak of the distributions and the spread in the shape would have a continuous increase as a function of energy. Given the χ^2 for some of the fits and the large uncertainties in some of the fit parameters, it is likely that the defined shape may not be representative of the neutron emission at all energies.

The multiplicity distribution was based on an assumption that fission neutron follow a skewed Gaussian distribution, and from this distribution the neutron moments were derived. However, the discontinuity in the multiplicity spectrum draws concern over this assumption. As a test of the assumed shape to deduce the moments, the first neutron multiplicity moment was compared to the average neutron multiplicity which was determined directly. In Figure 6.3, the first neutron moment was consistent with the average neutron moment, although deriving this quantity through an assumed shape increases the uncertainty of the

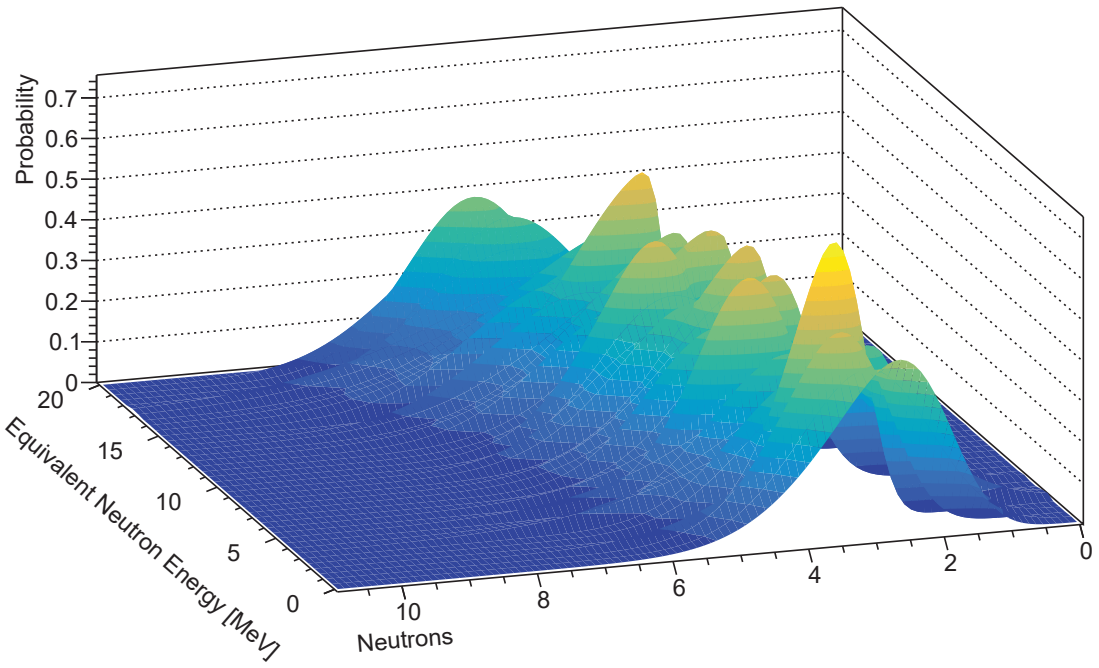

Figure 6.2: Fission neutron multiplicity spectrum assuming a skewed Gaussian distribution as a function of equivalent neutron energy. There appears to be bin to bin discontinuities in the spectrum indicating the assumed shape may not be representative of the neutron emission for some energy ranges.

measurement due primarily to uncertainties in the μ parameter. By applying Equations 5.12 and 5.13, the second and third neutron multiplicity moment was determined and is found in 6.3.

For the subsequent moments, there was no existing data to compare the results with. As a result, the first moment and average neutron multiplicity moment serves a "benchmark" to this approach. The uncertainty increases significantly with the higher order moments, but similarly to the $\bar{\nu}$ all moments have linear trends with respect to the equivalent neutron energy. In all three moments there are a few points which deviate from the observed trend. The neutron separation energies in this range are 6.3 Mev, 11.6 MeV, and 18.08 MeV. At separation energies the residual nucleus following evaporation has significantly less energy. Additionally, the Weisskopf-Ewing limit requires enough excitation energy for reactions to occur where the nucleus has a high density of states. Aside from the separation energies, reducing the neutron multiplicity spectrum to neutron multiplicity moments reduces the observed bin to bin discontinuities.

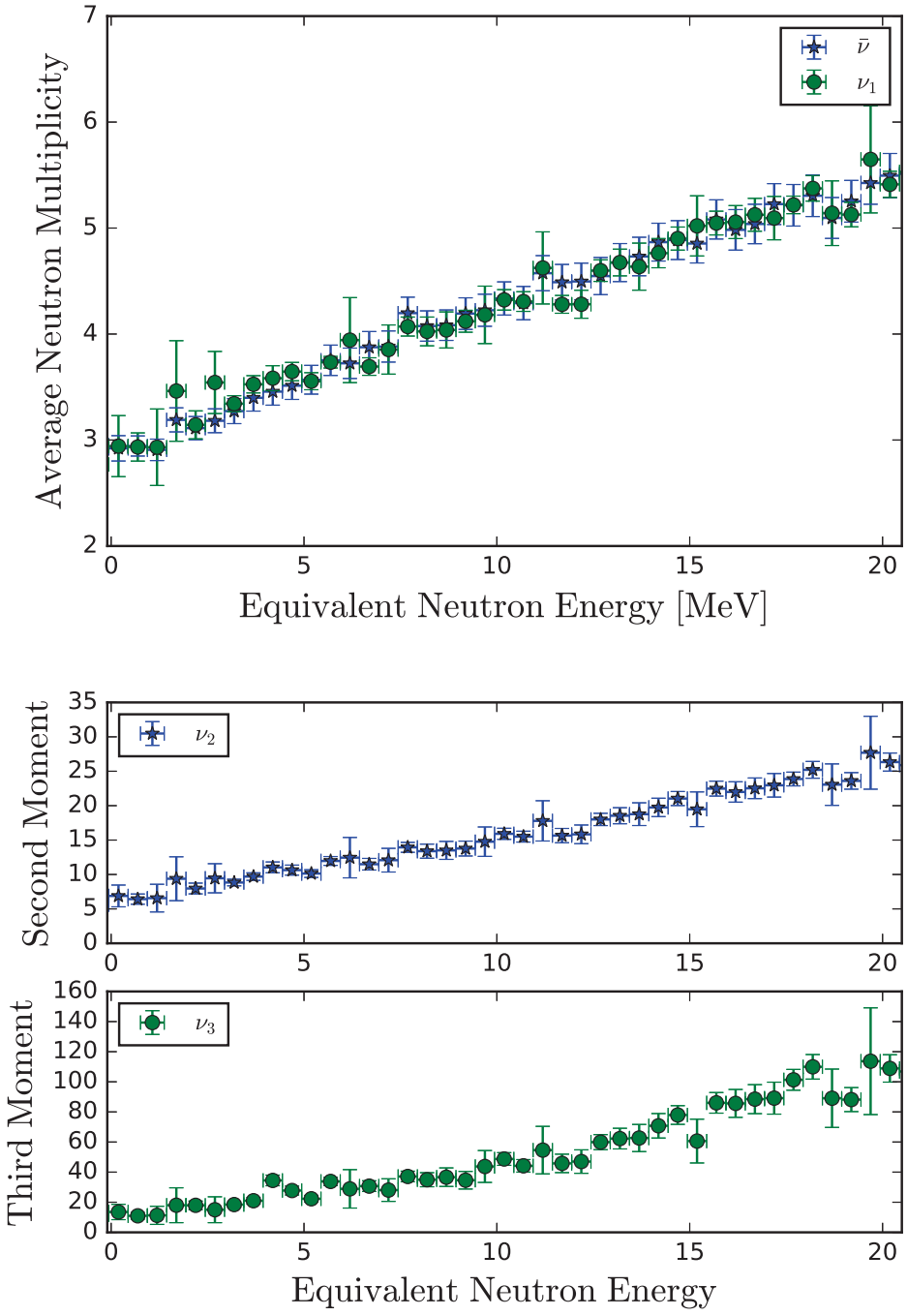

Figure 6.3: Derived neutron multiplicity moments for ^{241}Pu as a function of equivalent neutron energy. The first neutron multiplicity moment was compared to the average neutron multiplicity as a benchmark to the methodology.

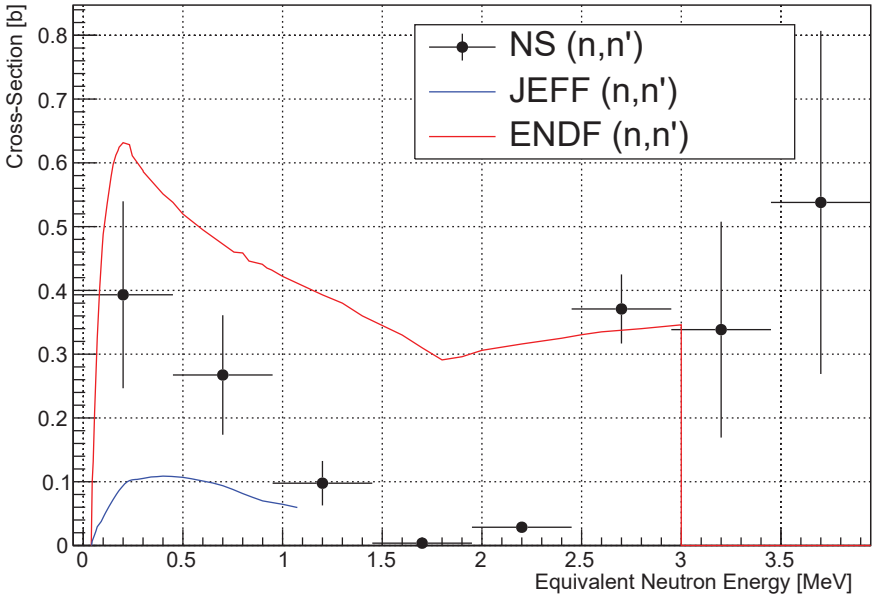

Figure 6.4: Surrogate result for ^{241}Pu(n,n') compared to the ENDF and JEFF database cross sections.

6.2 Experimental Results for ^{241}Pu(n,xn)

From this experiment three cross-sections were derived: (n,n'), (n,2n), and (n,3n). Unlike the fission measurements and (n,n') cross section, both of the (n,2n) and (n,3n) cross sections are represented in 1 MeV bins primarily due to the carbon contributions. Each result was compared to the ENDF and JEFF database cross-section. All three of the ENDF and JEFF quantities consited of cross-sections derived from theory, and in some cases (i.e. the ENDF (n,n') and (n,2n)) it is evident that there was an interpolation error when the cross-section was entered. In both the (n,n') and the (n,2n) cross-section the observed shape is not consistent with the nature of these reactions. For (n,n') reactions the cross section should decrease when approaching a neutron separation energy. As evident in Figure 6.4, the cross section looks as though it is beginning to decrease. However, above 3 MeV the cross-section rises again. It appears as through there was not adequate resolution between the (n,n') and (n,2n) cross section, highlighting concerns with the efficiency. Similarly in Figure 6.5, the same feature is found for the (n,2n) spectrum but at a lower amplitude. The (n,3n) cross section, shown in Figure 6.6, rises at the threshold as expected. Due to the limitations in energy range it is not apparent if at higher energies, where (n,4n) and other compound emissions become energetically feasible, if the cross-section resolves itself or has the same features as the (n,n') and (n,2n) measurement.

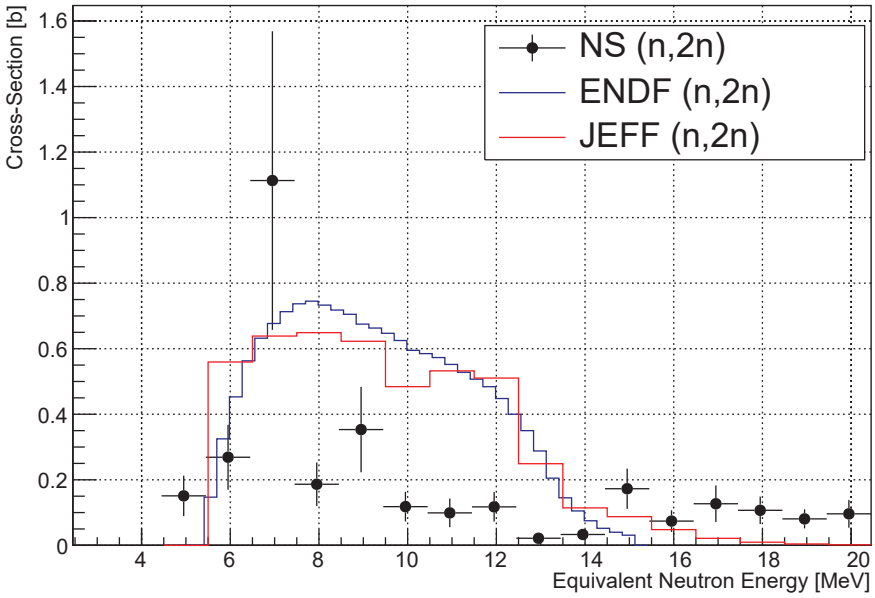

Figure 6.5: Surrogate result for ^{241}Pu(n,2n) compared to the ENDF and JEFF database cross sections.

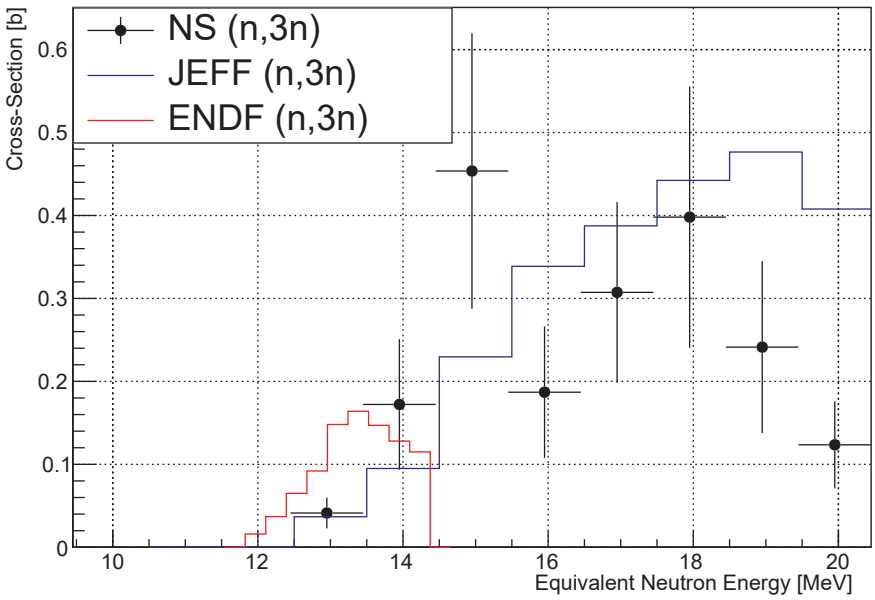

Figure 6.6: Surrogate result for ^{241}Pu(n,3n) compared to the ENDF and JEFF database cross sections.

Chapter 7

Conclusion and Future Work

Nuclear data for fission neutron branching ratios and (n,xn) reactions are important parameters for applied nuclear physics and engineering. Although the physical processes for these reactions are well understood for long-lived actinides, there has been little progress for measurements of unstable isotopes. To date there have been 21 experiments to measure the prompt fission neutron emission from ^{239}Pu, while only three measurements existed for ^{241}Pu. Given the high neutron flux in reactors, and the rate of interaction on isotopes many unstable nuclei contribute to the neutron economy through absorption, fission, and other emission pathways. The work discussed in the present text details the modeling, design, and characterization of a new experimental apparatus to perform surrogate measurements where the measured quantity pertains to the emission of neutrons. Additionally, this is the first experiment where the surrogate method was used to measure fission neutron multiplicities and (n,xn) cross-sections.

The conceptual design for the NeutronSTARS array consisted of a modified scattering chamber from the past STARS experiments with a large neutron detector previously referred to as the NIMROD-ISIS array which had been inherited from the Texas A&M Cyclotron Facility [48, 26]. The combination of the two resulted in the first experimental array capable of measuring fission neutron multiplicities without large neutron backgrounds from an incident neutron beam. Although the STARS chamber only required assembly and calibration, consistent with past experiments; the degradation of the scintillator and photomultiplier tubes required a simulation and modeling effort to determine the optimal configuration based on the available funds. After the scintillator was refurbished, the entire array's response to charged and neutral particles was characterized. To ensure the array's ability to reconstruct multiplicity distributions a ^{252}Cf source was measured and fit to a skewed Gaussian distribution.

The actual experiment consisted of 55 MeV alpha particles incident on a ^{242}Pu target as a surrogate for neutrons incident on ^{241}Pu. The target consisted of plutonium oxide electroplated onto a carbon backing. To account for target related backgrounds Mylar and Carbon targets were run under the same conditions. Due to the pulse height of carbon and oxygen breakup relative to that of fission fragments, the contributions from these elements can be

excluded with a high energy cut in the fission detector, while the these isotopes dominated the zero and one neutron multiplicity bin. Given the efficiency of the neutron detector, the multiplicity distribution from fission was determined by making a fit to the detection response and a skewed Gaussian distribution with the detected neutron spectrum. The average neutron multiplicity was measured directly based on events in the prompt and background gates. Overall, the uncertainties on all derived quantities for the fission multiplicities were limited by counting statistics. This measurement was the first demonstration of using the surrogate method to measure prompt fission neutron multiplicities. A higher efficient array and more statistics can quantify the neutron multiplicity distribution without relying on an assumed shape.

The (n,xn) cross-sections were derived from measuring the Plutonium target and subtracting contributions from fission, oxygen, and carbon. Additionally, the efficiency of the array was corrected to account for the neutron energy distribution from these reactions increasing the uncertainty in the efficiency. To "convert" the (α,α'xn) reaction rate into a cross-section a ratio between the measured fission counts and the known fission cross-section was implemented. Due to the large contribution of carbon and oxygen in the sample, the zero neutron multiplicity bin was excluded from the analysis. Given the low efficiency of the array relying on the one, two, and three neutron bins resulted in a higher uncertainty given the small parameter space to extract (α,α'xn) quantities.

Current efforts are underway for subsequent measurements and analysis of other isotopes using the NeutronSTARS array. The ^{239}Pu experiment was done in conjunction with the ^{241}Pu. Given that ^{239}Pu has more available data for the average neutron multiplicity than any other isotope, the results of the analysis can pinpoint systematic associated with the application of the surrogate method to these measurements. In the present work the (n,xn) cross-sections had large uncertainties, to further study this method's ability to measure (n,xn) reactions non-fissile radionuclides with no carbon backing are currently being evaluated. Additionally, the end-caps have recently been re-filled increasing the efficiency by an additional 30%. This upgrade gives the array the ability to measure fission neutron distributions directly. Additionally, a higher efficient array lowers the probability that one, two, and three multiplicity neutrons are detected as a zero neutron multiplicity event.

Subsequent measurements should treat the fission neutron multiplicity and (n,xn) reactions separately. To reduce the fusion-fission contribution from the (n,xn) spectrum a low beam current was selected. As a result the statistics in the prompt fission neutron multiplicity were low compared to other (n,f) measurements performed using the surrogate method [7]. Lastly, when observing neutron multiplicity measurement campaigns as a whole, most measurements occurred in the late 60's to early 70's. Although there is a renewed interest in updating these measurements, using different interaction mediums can decouple systematic uncertainties consistent with measurements using gadolinium-doped scintillators. The entire NeutronSTARS array requires a total 3.5 tons of scintillator to achieve the maximum efficiency. The large volume is used predominately to contain the gamma-ray cascade following neutron capture. Lithium doped materials with pulse-shape discrimination capabilities or $Cs_2LiLaBr_6$ crystals requires less volume, and has positional sensitivity for neutrons.

To date the surrogate method has had the capability of measuring the fission neutron cross-section, the fission fragment distributions, and gamma-ray cascades [13]. For the first time the surrogate method has been expanded to measure neutron emission from fission and (n,xn) reactions. This progress in experimental surrogate campaigns will strengthen the available nuclear data for reactor designs, nonproliferation, nuclear forensics, and stockpile stewardship.

Appendix A

Tabulated Results of the (n,xn) Cross Section and Fission Neutron Multiplicity.

E_n	$\sigma_{(n,n')}$[barns]	E_n	$\sigma_{(n,2n)}$[barns]	E_n	$\sigma_{(n,3n)}$[barns]
0.25 ± 0.25	0.393 ± 0.146	5.00 ± 0.50	0.151 ± 0.061	13.00 ± 0.50	0.041 ± 0.018
0.75 ± 0.25	0.267 ± 0.093	6.00 ± 0.50	0.268 ± 0.099	14.00 ± 0.50	0.172 ± 0.078
1.25 ± 0.25	0.097 ± 0.034	7.00 ± 0.50	1.113 ± 0.455	15.00 ± 0.50	0.453 ± 0.166
1.75 ± 0.25	0.003 ± 0.000	8.00 ± 0.50	0.186 ± 0.066	16.00 ± 0.50	0.186 ± 0.079
2.25 ± 0.25	0.028 ± 0.004	9.00 ± 0.50	0.353 ± 0.130	17.00 ± 0.50	0.307 ± 0.108
2.75 ± 0.25	0.370 ± 0.054	10.0 ± 0.50	0.118 ± 0.045	18.00 ± 0.50	0.398 ± 0.157
3.25 ± 0.25	0.338 ± 0.122	11.0 ± 0.50	0.099 ± 0.043	19.00 ± 0.50	0.241 ± 0.103
3.75 ± 0.25	0.537 ± 0.218	12.0 ± 0.50	0.117 ± 0.044	20.00 ± 0.50	0.123 ± 0.052
4.25 ± 0.25	0.638 ± 0.241	13.0 ± 0.50	0.021 ± 0.009		
		14.0 ± 0.50	0.033 ± 0.013		
		15.0 ± 0.50	0.172 ± 0.061		
		16.0 ± 0.50	0.074 ± 0.033		
		17.0 ± 0.50	0.126 ± 0.055		
		18.0 ± 0.50	0.106 ± 0.041		
		19.0 ± 0.50	0.080 ± 0.028		
		20.0 ± 0.50	0.096 ± 0.042		

Table A.1: Results of the (n,n'), (n,2n), and (n,3n) cross-sections for ^{241}Pu

Table A.2: Results for the skewed Gaussian parameters as a function of equivalent neutron energy E_n[MeV].

E_n[MeV]	μ	σ	β	χ^2/df
0.0 ±.25	2.13 ± 0.334	1.53 ± 0.139	0.894 ± 0.358	5.540
0.5 ±.25	2.00 ± 0.146	1.45 ± 0.093	1.30 ± 0.232	2.344
1.0 ±.25	2.41 ± 0.385	1.29 ± 0.148	0.663 ± 0.478	1.979
1.5 ±.25	2.77 ± 0.448	1.22 ± 0.277	1.04 ± 1.48	3.436
2.0 ±.25	1.88 ± 0.163	1.83 ± 0.083	1.62 ± 0.183	0.673
2.5 ±.25	2.88 ± 0.373	0.95 ± 0.210	1.45 ± 2.08	1.983
3.0 ±.25	3.32 ± 0.150	1.20 ± 0.022	$(1.63 \pm 1.07) \times 10^{-3}$	1.819
3.5 ±.25	3.47 ± 0.158	1.16 ± 0.026	$(2.29 \pm 1.) \times 10^{-3}$	1.593
4.0 ±.25	1.59 ± 0.167	2.50 ± 0.068	3.12 ± 0.314	4.588
4.5 ±.25	1.97 ± 0.130	2.06 ± 0.069	4.37 ± 0.697	2.172
5.0 ±.25	3.55 ± 0.157	1.13 ± 0.031	$(4.22 \pm 1.95) \times 10^{-3}$	0.999
5.5 ±.25	2.05 ± 0.122	2.14 ± 0.045	4.98 ± 0.015	0.085
6.0 ±.25	3.40 ± 0.357	1.07 ± 0.196	0.808 ± 1.11	3.491
6.5 ±.25	2.11 ± 0.147	1.99 ± 0.064	5.0 ± 1.521	0.568
7.0 ±.25	2.87 ± 0.239	1.41 ± 0.186	2.02 ± 1.13	2.582
7.5 ±.25	4.11 ± 0.178	1.09 ± 0.045	$(3.19 \pm 2.09) \times 10^{-3}$	4.654
8.0 ±.25	2.75 ± 0.123	1.67 ± 0.122	2.86 ± 1.20	2.390
8.5 ±.25	2.96 ± 0.197	1.60 ± 0.128	1.61 ± 0.369	2.365
9.0 ±.25	3.02 ± 0.171	1.43 ± 0.130	3.12 ± 1.38	0.042
9.5 ±.25	3.39 ± 0.331	1.50 ± 0.131	0.819 ± 0.291	1.151
10.0 ±.25	4.32 ± 0.193	1.28 ± 0.032	$(2.43 \pm 1.39) \times 10^{-3}$	0.686
10.5 ±.25	4.32 ± 0.191	1.08 ± 0.058	$(2.56 \pm 2.05) \times 10^{-3}$	3.491
11.0 ±.25	3.86 ± 0.344	1.26 ± 0.213	1.19 ± 1.04	2.812
11.5 ±.25	3.13 ± 0.177	1.57 ± 0.102	4.77 ± 0.548	2.547
12.0 ±.25	3.15 ± 0.211	1.60 ± 0.129	4.93 ± 0.175	1.575
12.5 ±.25	4.56 ± 0.199	1.32 ± 0.035	$2.82 \pm 1.76) \times 10^{-3}$	0.884
13.0 ±.25	3.19 ± 0.143	1.91 ± 0.107	3.26 ± 1.14	0.561
13.5 ±.25	3.33 ± 0.224	1.73 ± 0.110	4.34 ± 1.13	4.042
14.0 ±.25	3.21 ± 0.229	2.00 ± 0.086	4.98 ± 0.103	1.127
14.5 ±.25	4.90 ± 0.219	1.40 ± 0.027	$(2.54 \pm 1.64) \times 10^{-3}$	1.977
15.0 ±.25	3.65 ± 0.369	1.38 ± 0.208	4.61 ± 0.797	0.915
15.5 ±.25	5.06 ± 0.231	1.38 ± 0.033	$(2.54 \pm 1.79) \times 10^{-3}$	1.159
16.0 ±.25	3.53 ± 0.215	2.09 ± 0.088	1.96 ± 0.217	0.566
16.5 ±.25	3.29 ± 0.221	2.24 ± 0.097	4.12 ± 0.733	0.837
17.0 ±.25	3.47 ± 0.206	2.07 ± 0.101	4.05 ± 1.11	2.185
17.5 ±.25	3.11 ± 0.190	2.56 ± 0.050	4.99 ± 0.686	1.303
18.0 ±.25	3.35 ± 0.188	2.59 ± 0.082	3.24 ± 0.422	1.372
18.5 ±.25	5.02 ± 0.294	1.36 ± 0.094	0.105 ± 0.269	2.145
19.0 ±.25	5.25 ± 0.226	1.10 ± 0.080	$(2.91 \pm 3.01) \times 10^{-3}$	0.590
19.5 ±.25	5.09 ± 0.384	1.20 ± 0.191	0.505 ± 1.13	0.851
20.0 ±.25	5.48 ± 0.243	1.31 ± 0.051	$(3.48 \pm 2.52) \times 10^{-3}$	0.957

Table A.4: Results for the average neutron multiplicity and fission neutron moments.

E_n[MeV]	$\bar{\nu}$	ν_1	ν_2	ν_3
0.0 ±.25	2.90 ± 0.118	2.94± 0.288	6.88 ±1.58	13.5 ±5.10
0.5 ±.25	2.92 ± 0.094	2.94± 0.133	6.42 ±0.74	11.0 ±2.20
1.0 ±.25	2.88 ± 0.100	2.94± 0.361	6.56 ±2.01	11.3 ±6.03
1.5 ±.25	3.17 ± 0.112	3.49± 0.474	9.38 ±3.19	18.0 ±11.58
2.0 ±.25	3.09 ± 0.108	3.12± 0.132	7.96 ±0.78	17.9 ±2.83
2.5 ±.25	3.16 ± 0.111	3.55± 0.293	9.45 ±2.12	15.0 ±8.59
3.0 ±.25	3.25 ± 0.117	3.33± 0.075	8.83 ±0.48	18.4 ±1.76
3.5 ±.25	3.37 ± 0.124	3.48± 0.081	9.69 ±0.55	21.0 ±2.11
4.0 ±.25	3.43 ± 0.126	3.51± 0.118	11.030±.78	34.5 ±3.55
4.5 ±.25	3.49 ± 0.128	3.60± 0.087	10.630±.73	27.8 ±2.97
5.0 ±.25	3.54 ± 0.134	3.56± 0.080	10.130±.56	22.3 ±2.24
5.5 ±.25	3.72 ± 0.142	3.75± 0.054	11.970±.64	33.8 ±2.72
6.0 ±.25	3.70 ± 0.142	3.95± 0.401	12.452±.94	28.9 ±12.76
6.5 ±.25	3.85 ± 0.146	3.67± 0.083	11.490±.84	30.7 ±3.56
7.0 ±.25	3.85 ± 0.145	3.88± 0.232	12.081±.72	28.1 ±7.49
7.5 ±.25	4.17 ± 0.149	4.12± 0.090	13.940±.72	37.1 ±3.53
8.0 ±.25	4.05 ± 0.141	4.04± 0.136	13.391±.02	35.0 ±4.68
8.5 ±.25	4.05 ± 0.142	4.04± 0.170	13.501±.31	36.6 ±6.16
9.0 ±.25	4.16 ± 0.147	4.12± 0.103	13.771±.08	34.6 ±5.85
9.5 ±.25	4.19 ± 0.150	4.17± 0.271	14.762±.14	43.7 ±10.59
10.0 ±.25	4.30 ± 0.155	4.33± 0.097	15.910±.80	48.7 ±4.21
10.5 ±.25	4.26 ± 0.155	4.33± 0.093	15.500±.79	44.2 ±4.16
11.0 ±.25	4.54 ± 0.164	4.63± 0.340	17.792±.93	54.6 ±15.79
11.5 ±.25	4.46 ± 0.166	4.25± 0.084	15.651±.04	45.8 ±6.13
12.0 ±.25	4.46 ± 0.171	4.26± 0.132	15.831±.36	47.0 ±7.79
12.5 ±.25	4.51 ± 0.174	4.57± 0.102	18.000±.89	59.9 ±5.00
13.0 ±.25	4.64 ± 0.178	4.66± 0.126	18.541±.17	62.3 ±6.86
13.5 ±.25	4.70 ± 0.180	4.66± 0.222	18.761±.65	62.7 ±9.01
14.0 ±.25	4.83 ± 0.177	4.72± 0.138	19.741±.34	70.8 ±8.13
14.5 ±.25	4.85 ± 0.182	4.90± 0.109	21.031±.02	77.9 ±6.20
15.0 ±.25	4.82 ± 0.182	5.01± 0.284	19.482±.52	60.6 ±14.54
15.5 ±.25	5.05 ± 0.183	5.07± 0.112	22.481±.09	86.0 ±6.85
16.0 ±.25	4.95 ± 0.189	4.99± 0.156	21.991±.48	85.6 ±9.26
16.5 ±.25	5.00 ± 0.184	5.06± 0.155	22.521±.50	88.5 ±9.63
17.0 ±.25	5.19 ± 0.191	5.14± 0.205	22.961±.71	89.1 ±10.62
17.5 ±.25	5.18 ± 0.194	5.11± 0.083	23.871±.00	101.3 ±6.92
18.0 ±.25	5.27 ± 0.194	5.27± 0.120	25.211±.22	110.0 ±8.16
18.5 ±.25	5.06 ± 0.191	5.14± 0.305	23.063±.01	89.1 ±19.38
19.0 ±.25	5.22 ± 0.195	5.26± 0.115	23.601±.20	88.2 ±7.97
19.5 ±.25	5.39 ± 0.199	5.68± 0.505	27.695±.30	113.7 ±35.45
20.0 ±.25	5.46 ± 0.207	5.49± 0.123	26.331±.31	108.9 ±9.11

Bibliography

[1] Rasha Abbasi et al. "Calibration and characterization of the IceCube photomultiplier tube". In: *Nuclear Instruments and Methods in Physics Research Section A: Accelerators, Spectrometers, Detectors and Associated Equipment* 618.1 (2010), pp. 139–152.

[2] OA Akindele et al. "NeutronSTARS: A segmented neutron and charged particle detector for low-energy reaction studies". In: *Nuclear Instruments and Methods in Physics Research Section A: Accelerators, Spectrometers, Detectors and Associated Equipment* 872 (2017), pp. 112–118.

[3] JA Becker et al. "Partial y-Ray Cross Sections for the Reaction 239Pu (n, 2ny/) and the 239Pu (n, 2n) Cross Section". In: (2001).

[4] John A Becker and Ron O Nelson. "New physics opportunities with GEANIE at LANSCE/WNR". In: *Nuclear Physics News* 7.2 (1997), pp. 11–14.

[5] JW Boldeman and MG Hines. "Prompt neutron emission probabilities following spontaneous and thermal neutron fission". In: *Nuclear Science and Engineering* 91.1 (1985), pp. 114–116.

[6] CAEN. "16 Channel Programmable Spectroscopy Amplifier". In: *http://www.caen.it/csite/CaenProd.jsp?idmod=102£ \&£parent=12* (July 2017).

[7] RJ Casperson et al. "Measurement of the Am 240 (n, f) cross section using the surrogate-ratio method". In: *Physical Review C* 90.3 (2014), p. 034601.

[8] H Conde, J Hansen, and M Holmberg. "Prompt v in neutron-induced fission of 239Pu and 241Pu". In: *Journal of Nuclear Energy* 22.1 (1968), pp. 53–60.

[9] Steven Dazeley et al. "A water-based neutron detector as a well multiplicity counter". In: *Nuclear Instruments and Methods in Physics Research Section A: Accelerators, Spectrometers, Detectors and Associated Equipment* 771 (2015), pp. 32–38.

[10] James J Duderstadt and Louis J Hamilton. *Nuclear reactor analysis*. Vol. 1. Wiley New York, 1976.

[11] NP D'yachenko et al. "Energy dependence of average number of prompt neutrons in Pu 241 fission". In: *Atomic Energy* 36.4 (1974), pp. 406–407.

[12] Eljen. "EJ-335". In: *http://www.eljentechnology.com* (July 2017).

[13] Jutta E Escher et al. "Compound-nuclear reaction cross sections from surrogate measurements". In: *Reviews of Modern Physics* 84.1 (2012), p. 353.

[14] Jutta E Escher et al. "Compound-nuclear reaction cross sections from surrogate measurements". In: *Reviews of modern physics* 84.1 (2012), p. 353.

[15] J FREHAUT et al. "MEASUREMENT OF THE AVERAGE NUMBER,NU-BAR, OF THE PROMPT NEUTRONS EMITTED IN THE PU-240 AND PU-241 FISSION INDUCED BY NEUTRONS OF ENERGY BETWEEN 1.5 AND 15 MEV. (IN FRENCH)." In: *Rapport CEA-R-4626* ().

[16] J Frehaut et al. "Status of (n, 2n) cross section measurements at Bruyeres-le-Chatel". In: *Proc. of Symposium on Neutron Cross Sections from.* 1980.

[17] BL Goldblum et al. "Determination of (n, γ) cross sections in the rare-earth region using the surrogate ratio method". In: *Physical Review C* 78.6 (2008), p. 064606.

[18] Walter Hauser and Herman Feshbach. "The inelastic scattering of neutrons". In: *Physical review* 87.2 (1952), p. 366.

[19] Mark Holt, Richard J Campbell, and Mary Beth Nikitin. *Fukushima nuclear disaster.* Congressional Research Service, 2012.

[20] RO Hughes et al. "The hyperion particle-γ detector array". In: *Nuclear Instruments and Methods in Physics Research Section A: Accelerators, Spectrometers, Detectors and Associated Equipment* 856 (2017), pp. 47–52.

[21] Marc A Humphrey, Kevin D Veal, and Stephen J Tobin. "Topical Papers-The Next Generation Safeguards Initiative's Spent Fuel Nondestructive Assay Project". In: *JNMM-Journal of the Institute of Nuclear Materials Management* 40.3 (2012), p. 6.

[22] I Hutcheon, M Kristo, and K Knight. *Nonproliferation nuclear forensics.* Tech. rep. Lawrence Livermore National Laboratory (LLNL), Livermore, CA, 2015.

[23] Safeguards IAEA. *technique and equipment: 2011 edition.* Tech. rep. IAEA/NVS/1, 2011.

[24] Arjan Koning, Stephane Hilaire, and Stephane Goriely. "TALYS-1.6 A Nuclear Reaction Program". In: *User Manual (NRG, The Netherlands), First Edition: December* 23 (2013), p. 2013.

[25] Kenneth S Krane and David Halliday. *Introductory nuclear physics.* Vol. 465. Wiley New York, 1988.

[26] SR Lesher et al. "STARS/LiBerACE: Segmented silicon and high-purity germanium detector arrays for low-energy nuclear reaction and structure studies". In: *Nuclear Instruments and Methods in Physics Research Section A: Accelerators, Spectrometers, Detectors and Associated Equipment* 621.1 (2010), pp. 286–291.

[27] JP Lestone. "Energy and Isotope Dependence of Neutron Multiplicity Distributions". In: *arXiv preprint arXiv:1409.5346* (2014).

[28] RW Lougheed et al. "239Pu and 241Am (n, 2n) cross-section measurements near En= 14 MeV". In: *Radiochimica Acta* 90.12/2002 (2002), pp. 833–843.

[29] DP McNabb et al. *Evaluation of the 239Pu (n, 2n) integrated cross section*. Tech. rep. Lawrence Livermore National Laboratory (LLNL), Livermore, CA, 2001.

[30] Mesytec. "MADC-32". In: *http://www.mesytec.com* (July 2017).

[31] Micron. "http://www.micronsemiconductor.co.uk". In: (July 2017).

[32] MIDAS. In: *https://www.triumf.info/wiki/DAQwiki/index.php/MIDAS* (July 2017).

[33] MPOD. In: *http://www.wiener-d.com/sc/power-supplies/mpod--lvhv/mpod-hv-module.html* (July 2017).

[34] NADS. In: *UCRL-WEB-207296* (2016).

[35] JB Parker et al. "Monte Carlo studies of scintillator efficiencies and scatter corrections for (n, 2n) cross section measurements". In: *Nuclear Instruments and Methods* 60.1 (1968), pp. 7–23.

[36] Sara A Pozzi, Enrico Padovani, and Marzio Marseguerra. "MCNP-PoliMi: a Monte-Carlo code for correlation measurements". In: *Nuclear Instruments and Methods in Physics Research Section A: Accelerators, Spectrometers, Detectors and Associated Equipment* 513.3 (2003), pp. 550–558.

[37] Ensslin Reilly and Kreiner Smith. "Passive Nondestructive Assay Manual-PANDA". In: *Los Alamos, NM: Safeguards Science and Technology Group at LANL* (1991).

[38] Frederick Reines et al. "Detection of the free antineutrino". In: *Physical Review* 117.1 (1960), p. 159.

[39] P Santi and M Miller. "Reevaluation of prompt neutron emission multiplicity distributions for spontaneous fission". In: *Nuclear Science and Engineering* 160.2 (2008), pp. 190–199.

[40] Julius Scherzinger et al. "Tagging fast neutrons from a 252Cf fission-fragment source". In: *arXiv preprint arXiv:1611.02940* (2016).

[41] Julius Scherzinger et al. "Tagging fast neutrons from an 241 Am/9 Be source". In: *Applied Radiation and Isotopes* 98 (2015), pp. 74–79.

[42] RP Schmitt et al. "A flexible 4π neutron detector for in-beam studies: the Texas A&M neutron ball". In: *Nuclear Instruments and Methods in Physics Research Section A: Accelerators, Spectrometers, Detectors and Associated Equipment* 354.2-3 (1995), pp. 487–495.

[43] ND Scielzo et al. "Measurement of γ-emission branching ratios for Gd 154, 156, 158 compound nuclei: Tests of surrogate nuclear reaction approximations for (n, γ) cross sections". In: *Physical Review C* 81.3 (2010), p. 034608.

[44] Struck. "SIS3316-250-14 16 channel 250 MSPS 14-bit". In: *http://www.struck.de/sis3316.html* (July 2017).

[45] M Sweany et al. "Large-scale gadolinium-doped water Cherenkov detector for nonproliferation". In: *Nuclear Instruments and Methods in Physics Research Section A: Accelerators, Spectrometers, Detectors and Associated Equipment* 654.1 (2011), pp. 377–382.

[46] F Tovesson and TS Hill. "Cross Sections for 239Pu (n, f) and 241Pu (n, f) in the Range En= 0.01 eV to 200 MeV". In: *Nuclear Science and Engineering* 165.2 (2010), pp. 224–231.

[47] VF Weisskopf and DH Ewing. "On the yield of nuclear reactions with heavy elements". In: *Physical Review* 57.6 (1940), p. 472.

[48] S Wuenschel et al. "NIMROD–ISiS, a versatile tool for studying the isotopic degree of freedom in heavy ion collisions". In: *Nuclear Instruments and Methods in Physics Research Section A: Accelerators, Spectrometers, Detectors and Associated Equipment* 604.3 (2009), pp. 578–583.